

EXPERIMENTAL STUDY AND DEVELOPMENT OF SUSTAINABLE SANDWICH
PANELS

by

Raghad Kassab

Submitted in partial fulfilment of the requirements
for the degree of Master of Applied Sciences

at

Dalhousie University
Halifax, Nova Scotia
March 2020

© Copyright by Raghad Kassab, 2020

TABLE OF CONTENTS

LIST OF TABLES	VI
LIST OF FIGURES.....	VII
ABSTRACT.....	XI
LIST OF ABBREVIATIONS AND SYMBOLS USED	XII
ACKNOWLEDGMENTS.....	XVI
CHAPTER 1 INTRODUCTION.....	1
1.1 BACKGROUND	1
1.2 PROBLEM STATEMENT.....	2
1.3 RESEARCH STATEMENT	3
1.4 THESIS ORGANIZATION.....	4
CHAPTER 2 LITERATURE REVIEW.....	6
2.1 INTRODUCTION TO PLASTICS	6
2.2 MAJOR TYPES OF PLASTIC	8
2.2.1 Thermosets	8
2.2.2 Thermoplastics	10
2.2.2.1 Types of Thermoplastics	11
2.3 PLASTIC WASTE POLLUTION.....	14
2.3.1 Environmental Impact of Plastic Waste	15
2.3.1.1 Entanglement of Marine Organisms.....	16
2.3.1.2 Ingestion by Marine Organisms	17
2.3.1.3 Plastic Waste in Landfills.....	18
2.3.2 Benefits of Plastic	19
2.3.3 Solutions to Plastic Waste Pollution	21
2.4 RECYCLING OF PLASTIC WASTE	22
2.5 INTRODUCTION TO SANDWICH PANELS.....	25
2.5.1 Mechanics of Sandwich Composites	25

2.5.1.1	Normal Stresses.....	27
2.5.1.2	Deflection.....	28
2.5.1.3	Curvature.....	29
2.5.2	History and Applications of Sandwich Structures	32
2.5.3	Design Criteria of Sandwich Panels.....	34
2.5.3.1	Failure Modes of Sandwich Panels	34
2.5.3.1.1	Face Yielding or Rupture.....	35
2.5.3.1.2	Core Shear.....	36
2.5.3.1.3	Compression Face Wrinkling.....	36
2.5.3.1.4	Failure Mode Map.....	37
CHAPTER 3 EXPERIMENTAL PROGRAM.....		38
3.1	GENERAL STRATEGY	38
3.2	TEST MATRIX	38
3.3	MATERIAL PROPERTIES OF SANDWICH FACING.....	39
3.3.1	Fabrication of FRP Coupons.....	39
3.3.2	Instrumentation and Coupon Testing Procedure.....	42
3.3.3	Analysis and Results of Coupon Testing	44
3.3.4	Bilinear Stress-Strain Model of PET FRP	47
3.4	MATERIAL PROPERTIES OF CORE COMPONENT.....	49
3.5	FABRICATION OF SANDWICH PANELS	53
3.6	INSTRUMENTATION AND BENDING TEST SET-UP.....	55
3.7	DATA ANALYSIS AND TEST RESULTS	57
3.7.1	Load-Deflection	58
3.7.2	Bending Strain.....	60
3.7.2	Moment-Curvature.....	61
3.7.3	Failure Mode.....	62
CHAPTER 4 ANALYTICAL MODEL		65
4.1	SYNOPSIS.....	65
4.2	MODELLING LOAD-DEFLECTION BEHAVIOR	65
4.2.1	Linear Model.....	66
4.2.2	Non-Linear Model.....	66

4.2.2.1 Deflection Due to Bending.....	66
4.2.2.2 Deflection Due to Shear	69
4.2.3 Verification of Load-deflection models.....	74
4.3 BREAKDOWN OF SHEAR AND BENDING DEFLECTIONS REGARDING CHANGE IN DENSITY OF RECYCLED PET FOAM CORE	76
4.4 MODELING FAILURE MODES.....	78
4.4.1 Transition between Face Rupture and Core Shear	78
4.4.2 Transition between Face Rupture and Wrinkling	79
4.4.3 Transition between Core Shear and Wrinkling.....	80
4.5 PARAMETRIC STUDY.....	81
4.5.1 Effect of Core Thickness (Core Density = 80 kg/m ³ , 200 kg/m ³ , 320 kg/m ³)...84	
4.5.2 Effect of Facing Thickness (Core Density = 80 kg/m ³ , 200 kg/m ³ , 320 kg/m ³)85
4.5.3 Effect of Span Length (Core Density = 80 kg/m ³ , 200 kg/m ³ , 320 kg/m ³)	87
CHAPTER 5 CONCLUSIONS AND RECOMMENDATIONS.....	89
5.1 CONCLUSIONS.....	89
5.2 RECOMMENDATIONS FOR FUTURE RESEARCH	91
BIBLIOGRAPHY	92
APPINDIX A: DETAILS ON PP HONEYCOMB CORE MODELING	97
A1 OVERVIEW.....	97
A1 DEVELOPMENT OF SOLIDWORKS MODEL	97
A3 APPLYING STRESS ON DEVELOPED MODEL	98
A3.1 SHEAR TEST.....	99
A3.1.1 Shear Modulus Sample Calculation.....	101
A3.2 BARE COMPRESSION TEST	103
A3.2.1 Elastic Modulus in Bare Compression Sample Calculation	104
A3.3 HONEYCOMB COMPRESSION TEST	105
APPINDIX B: COMPUTING STRAIN USING VBA PROGRAMMING LANGUAGE.....	108
B1 OVERVIEW.....	108

B2	INTRODUCTION TO VBE	108
B3	EXPLANATION OF VBA CODE	109
B4	VBA CODE FOR GOALSEEK ANALYSIS	110
APPENDIX C: SHEAR TEST ON POLYPROPYLENE HONEYCOMB CORE.....		111
C1	OVERVIEW.....	111
C2	LOADING APPARATUS.....	111
C3	ULTIMATE SHEAR STRENGTH CALCULATION	112
APPENDIX D: SHEAR CONTRIBUTION TO BENDING ANALYSED WITHIN PARAMETRIC STUDY		113
D1	OVERVIEW.....	113
D1.1	Breakdown of Total Deflection with Respect to Change in Core Thickness (Core Density = 80 kg/m ³ , 200 kg/m ³ , 320 kg/m ³)	113
D1.2	Breakdown of Total Deflection with Respect to Change in Facing Thickness (Core Density = 80 kg/m ³ , 200 kg/m ³ , 320 kg/m ³)	116
D1.3	Breakdown of Total Deflection with Respect to Change in Span Length (Core Density = 80 kg/m ³ , 200 kg/m ³ , 320 kg/m ³)	119

LIST OF TABLES

Table 2-1	Types of thermosets and their corresponding applications	9
Table 2-2	World textile fibre production (Discover Natural Fibres Initiative, 2019)	11
Table 2-3	Thermoplastics' resin identification symbols, associated acronyms, full names and uses (Canadian Office of Consumer Affairs, 2019; Anon., 2015).....	13
Table 2-4	Materials discarded in United States landfills from 1960 to 2010 (in thousands of tons) (Macpherson, 2014).	19
Table 2-5	Number of times different types of carrier bags need to be reused to provide the same environmental performance of the average LDPE carrier bags (Bisinella, et al., 2018).....	21
Table 3-1	Test Matrix	39
Table 3-3	GFRP tensile test summary	46
Table 3-4	Sandwich panel specimens' mechanical properties at ultimate limit state.	57
Table 4-1	Change in shear contribution to total deflection regarding varying core densities	78
Table 4-2	Mechanical properties of sandwich panels with varying core thickness and core density ($t_f = 6\text{mm}$, $L = 3\text{m}$)	83
Table 4-3	Mechanical properties of sandwich panels with varying face thickness and core density ($t_c = 150\text{mm}$, $L = 3\text{m}$).....	83
Table 4-4	Mechanical properties of sandwich panels with varying span length and core density ($t_f = 6\text{mm}$, $t_c = 150\text{mm}$)	83

LIST OF FIGURES

Figure 1-1	Breakdown of main research stages.	4
Figure 1-2	Crude oil distillation unit and products (EIA, 2012).....	7
Figure 2-2	Chemical structure of thermosets.	8
Figure 2-3	Plastic production rate over the years. (a) The three phases of plastic production rates. (b) Identification of the percentage in which each sector consumes plastic in 2015. (Worm, et al., 2017)	14
Figure 2-4	The effect of entanglement on marine organisms (a) (Flip, 2013) (b) (Sinclair, 2014) (c) (Shelton, 2019) (d) (Leavy, 2018) (e) (Kelly, 2016) (f) (Groves, 2019).....	16
Figure 2-5	Examples of marine organisms and seabirds that were victims of plastic ingestion (a) (Lofgren, 2014) (b) (Thompson, 2018) (c) (Wilson, 2017) (Shelton, 2019) (d) (Anon., 2019).....	18
Figure 2-6	Mechanical recycling process of thermoplastic waste(Ragaert, et al., 2017).....	23
Figure 2-7	Meteghan River house under construction made using foam recycled from plastic (Comeau, 2019).....	25
Figure 2-8	Sandwich beam loaded in three-point bending.	26
Figure 2-9	Stress distribution along the beam’s cross-section (Zenkert, 1997).....	28
Figure 2-10	Breakdown of total deflection into (a) bending deflection and (b) shear deflection (Betts, et al., 2018)	29
Figure 2-11	Cross-section of deformed beam under pure bending	30
Figure 2-12	Sandwich structure in human anatomy. (a) Cross-sectional view of human skull (source: fineartamerica.com) (b) Bones of the sandwich structure within a human skull (Wang, et al., 2014).	32
Figure 2-13	Side view sketch of the built-up beam used in Duleau’s experiments (Timoshenko, 1953).	33
Figure 2-14	Sandwich panels in civil engineering (a) Exterior Walls - Ikea Doha in Qatar, Ikea Bratislava in Slovakia and Ikea Bayonne in France (Source: bondor.com) (b) Roof Panels - Geusselt football stadium in the Dutch town of Maastricht (Source: viavac.com)	34

Figure 2-15	Failure modes sandwich panels (Zenkert, 1997).....	35
Figure 2-16	Failure modes map of a sandwich panel set(Zenkert, 1997).....	37
Figure 3-1	Fabrication of PET FRP Coupons: (a) epoxy spread on parchment paper; (b) layer of fabric placed on epoxy layer; (c) second layer of epoxy spread evenly on stitched fibres; (d) parchment paper placed on composite and scraper removed excess air bubbles; (e) after curing, composite was marked and prepared to be cut; (f) composite was cut into coupons.	41
Figure 3-2	Coupon testing setup (a) FRP coupon set on Instron8501 for tension test; (b) coupon testing apparatus; (c) FRP coupons prepared for DIC	43
Figure 3-3	Stress-strain diagrams of (a) GFRP with respect to PET FRP and (b) PET FRP	45
Figure 3-4	FRP coupons after reaching their ultimate tensile stress capacity; (a) PET FRP coupons; (b) GFRP coupons.	46
Figure 3-5	Bilinear stress-strain model based on Richard-Abbott equation.	47
Figure 3-6	Stress-strain curves of PET FRP and parameters used in Richard-Abbott bilinear stress-strain function	48
Figure 3-7	Change in mechanical properties with respect to core density: (a) elastic modulus vs foam density; (b) shear modulus vs foam density.....	50
Figure 3-8	Loading configuration applied on developed analytical model to derive the (a) shear modulus and; (b) elastic modulus.	51
Figure 3-9	Change in mechanical properties with respect to core density (a) shear modulus vs PP honeycomb density; (b) elastic modulus vs PP honeycomb density.	52
Figure 3-10	Change in shear strength of R-PET foam core with respect to core density.	53
Figure 3-11	Fabrication process of sandwich panels: (a) fabric layer cut to the required length; (b) parchment paper traced based on fabric layer; (c) unidirectional fabric was placed on layer of resin; (d) another layer of resin spread on fabric layer; (e) core component placed on top of epoxy layer; (f) weights placed on composite prior to curing stage.....	54
Figure 3-12	Sketch for three-point bending test set-up.....	56
Figure 3-13	Three-point bending test set-up.....	56

Figure 3-14	Load vs deflection curve of sandwich panels under three-point bending	58
Figure 3-15	Side view of sandwich panels made from (a) PP honeycomb core and (b) R-PET foam core after failure.	59
Figure 3-16	Compression and tension strains with respect to the applied load of the tested sandwich panels.	61
Figure 3-17	Moment vs curvature diagram associated to all the different sets of sandwich panels.....	62
Figure 3-18	Side-view images of tested beams.....	63
Figure 3-19	Side-view of the beam showing the sequence at which it failed. (a) Wrinkling of the top face appears and (b) starts propagating. (c) Core fails in shear.	64
Figure 4-1	Stress vs strain diagrams of facing component with secant lines plotted on the curve to obtain the “varying” secant modulus.....	67
Figure 4-2	Flowchart of bending deflection model.....	68
Figure 4-3	Non-linear shear stress vs shear strain projected relationship.....	69
Figure 4-4	Shear stress vs shear strain curve of core component.	71
Figure 4-5	Shear deflection of beam under three-point bending.	71
Figure 4-6	Flowchart of shear deflection model.	73
Figure 4-7	Flowchart for determining the failure load of sandwich panels made from PET FRP facings.	75
Figure 4-8	Load vs deflection curves of sandwich panel sets made from PET FRP facing and (a) PP honeycomb core, (b) R-PET 70 foam core, (c) R-PET 80 foam core and (d) R-PET 100 foam core, under three-point bending.	76
Figure 4-9	Breakdown of total deflection into shear and bending deflections of specimens made from PET FRP facings and R-PET foam core of varying densities.	77
Figure 4-10	Failure mode maps of PET FRP-RPET sandwich panel sets.....	81
Figure 4-11	Load-deflection curve displaying initial and ultimate-secant stiffnesses.....	82

Figure 4-12	Stress-strain and load-deflection curves for sandwich panels with varying core thickness and core density; (a-b) density = 80 kg/m^3 , (c-d) density = 200 kg/m^3 , (e-f) density = 320 kg/m^3	85
Figure 4-13	Stress-strain and load-deflection curves for sandwich panels with varying facing thickness and core density; (a-b) density = 80 kg/m^3 , (c-d) density = 200 kg/m^3 , (e-f) density = 320 kg/m^3	86
Figure 4-14	Stress-strain and load-deflection curves for sandwich panels with varying span length and core density; (a-b) density = 80 kg/m^3 , (c-d) density = 200 kg/m^3 , (e-f) density = 320 kg/m^3	88

ABSTRACT

The use of disposable plastic items has been increasing enormously throughout the past ten years. Despite comprising of recyclable polymers, thermoplastic waste has made international headlines as a major source of environmental pollution. For this thesis, multiple thermoplastic constituents were used to create different sets of sandwich panels that were later tested and studied rigorously to determine whether a relevant structural application can arise from the current thermoplastic waste. Polyethylene Terephthalate (PET), currently occupying the waste systems in the form of water bottles, single-use food utensils and polyester fibers, was used in fibre form to create a new fiber reinforced polymer (FRP) composite used as the facing material for the sandwich panels. Polypropylene (PP)—extensively employed when creating single-use plastic items such as plastic straws, water bottle caps and medicine vials—was used in the form of honeycomb as a core material to one set of sandwich panels. Another set of sandwich panels was made from recycled PET foam core, which was obtained from 100% post-consumer PET bottles. Failure mode maps for the different sets of the plastic sandwich panels were developed in order to distinguish the optimum structural design prior to the manufacturing process. Six different sets of sandwich beams were created and tested in three-point bending. Three identical panels were tested from each set to produce substantiated results. The major difference between each set of panels was the types of materials used in making up their core and skin components. Mechanical properties of the sandwich structures and their different components were obtained experimentally. Utilizing plastic waste by incorporating it in sandwich panel components improves the sustainability of the panels and reduces the current environmental pollution.

LIST OF ABBREVIATIONS AND SYMBOLS USED

Abbreviations

ASTM	American Society for Testing Materials
CCME	Canadian council of ministers of the environment
DAQ	Data Acquisition
DIC	Digital image correlation
EIA	Energy information administration
ETICS	External thermal insulation composite system
FAO	Food and agriculture organization
FEA	Finite element analysis
FMM	Failure mode map
FRP	Fibre reinforced polymer/plastic
GFRP	Glass fibre reinforced polymer
HDPE	High-density polyethylene
HSS	Hollow structural sections
LDPE	Low-density polyethylene
MIT	Massachusetts Institute of Technology
PET	Polyethylene terephthalate
PP	Polypropylene
PS	Polystyrene
PU	Polyurethane
PVC	Polyvinyl chloride
R	Recycled

SIP	Structural insulated panels
US	United States
UN	United Nations
VBA	Visual basic for application
VBE	Visual basic editor

Symbols

$(AG)_{eq}$	Equivalent shear rigidity
$(EI)_{eq}$	Equivalent flexural rigidity
E_c	Elastic modulus of sandwich core component
E_f	Elastic modulus of sandwich facing components
E_{sec}	Secant elastic modulus
E_{su}	Ultimate secant modulus
E_1	Primary modulus of elasticity
E_p	Plastic/secondary modulus of elasticity
G_c	Shear modulus of the core component
G_{secant}	Secant shear modulus
G_e	Shear modulus of the core component within elastic limit
I	Moment of inertia
K_i	Initial stiffness
K_u	Ultimate stiffness
L	Unsupported span length
O	Curve's origin

P	Applied load
P_{CS}	Failure load initiating core shear
P_f	Final applied load
P_{FR}	Failure load initiating face rupture
P_{FW}	Failure load initiating face wrinkling
P_i	Initial applied load
P_u	Peak load
V	Shear force
V_f	Fibre volume fraction
b	Cross-sectional width of sandwich panel
c	Core height
d	Distance between facings' centroids
f	Stress
f_o	Plastic stress
f_y	Yield stress
f_u	Ultimate strength
h	Depth of sandwich panel/cross-sectional height
n	Shape parameter
s	Spacings between supporting bars
t_f	Facing thickness
y	Vertical distance away from neutral axis
Ψ	Curvature
ΔP	Loading increments

δ_b	Bending deflection
δ_s	Shear deflection
δ_t	Total deflection
δ_u	Total deflection at peak load
ϵ	Strain
ϵ_{bottom}	Bottom strain
ϵ_{top}	Top strain
ϵ_u	Ultimate strain
ϵ_y	Yield strain
γ_u	Ultimate shear strain
γ_e	Maximum shear strain within elastic limit
θ	Central angle (in radians)
ρ	Radius of curvature
σ_c	Stress in the core component
σ_f	Stress in the facing component
τ_c	Shear stress in core component
τ_u	Ultimate shear strength

ACKNOWLEDGMENTS

First and foremost, I would like to thank my supervisor, Dr. Pedram Sadeghian, for providing the opportunity to be part of his research team and allowing me to complete my graduate studies in such an engaging environment. His constant encouragement, significant remarks and input had the greatest impact on this thesis and made the overall research period an enjoyable learning experience.

I would like to gratefully acknowledge Armcell[®] for supplying the recycled PET foam used in this research. I would also like to thank Mr. Kavish Bujun from Armacell[®] for his kindest assistance. I wish to acknowledge Dalhousie's technicians; Brian Kennedy, Jesse Keane, and Jordan Maerz, for their lab guidance, which allowed the experimentation period to run smoothly and safely. A special acknowledgement also goes to my colleagues; Dillon Betts, Ahmed Moussa, Lucas Marques, and Koosha Khorramian, for their constant lab support and inspiration.

Finally, I would like to express my sincerest gratitude to my parents, whom are an endless source of happiness and motivation. Your presence brings out the best in me and I cannot imagine life without you.

CHAPTER 1 INTRODUCTION

1.1 BACKGROUND

The shift towards building with sustainable materials stems from a global goal of preserving the environment for future generations. Sustainability focuses on providing resources capable of supplying essential needs that in turn do not affect future availability (Pearce et al., 2018). This project explores the use of plastic waste as a viable infrastructural material. Recycling waste is considered an honourable task, but there exists an unjustification: the use of waste products in applications requiring more strength than what the material can provide. Additionally, it is illogical to excessively refine waste products to increase strength properties. Energy spent on refining or enhancing waste material can often exceed the energy required for creating new materials. Therefore, energy consumption and strength properties were major aspects considered while developing new infrastructural applications from waste materials.

Using plastic waste as the sustainable element in this research was decided due to its negative environmental impact. Over time, plastic waste has made a markedly detrimental influence on the environment, aquatic habitation, and human health. This theory was proven through various studies conducted by numerous global sources. Although impossible to precisely gauge the amount of plastic waste polluting the ocean, a recent study estimates the number of plastic debris to be 5.25 trillion pieces, which totals an approximate mass of 26,900 ton (Francois et al., 2017). Despite these facts, the rate of plastic production and its environmental disposal rate has both significantly and steadily increased (Santos et al., 2015). This is primarily because of the wide range of superior properties associated with plastic, including its structural strength, or low weight;

durability; and flexibility (Christopher, 2018). Given these superior qualities, plastic has attracted many commercial sectors allowing a constant, large-scale production.

Today, most plastic products are either disposed in landfills or left to pollute the environment. In both cases, this material is unused after initial use; only 9% of produced plastic undergoes recycling due to the lack of applications available for consuming recycled plastic (Rhodes, 2019). Therefore, discovering a novel use for post-consumer plastic waste would generate a motive for recycling. Structural elements generally require a significant volume of building materials; thus, employing recycled plastic in infrastructure will reprocess vast quantities of current waste products.

Due to its relatively low mechanical performance (e.g. tensile and compressive strength) with respect to current construction materials, plastic could not be used in bulk form to create structural members, including beams and columns. Instead, plastic has been efficiently used in multiple forms to create sandwich composites. Those structure facings were comprised from plastic fibre reinforced polymer (FRP), in which plastic fibres were mixed with epoxy resin in a wet layup process to produce stiff sheets of plastic composite. Conversely, the core component of the sandwich structures was created from two major forms and types of plastic: polypropylene (PP), used in the honeycomb structure; and polyethylene terephthalate (PET), used in the foam form.

1.2 PROBLEM STATEMENT

The majority of sandwich panels used in engineering applications consume vast amounts of virgin constituents. When those panels are being used as Structural Insulated Panels (SIPs) —including prefabricated housing panels—the core component is most commonly made from a thermosetting plastic foam, which can not be derived from post-consumed

plastic waste. This conveys that sandwich panels in present days are not fully sustainable despite their large potential in consuming recycled materials and becoming an environmentally sustainable element due to their structural efficiency. In this research, the mechanical performance of sandwich panels made from recycled and recyclable thermoplastic constituents will be derived through experimental tests and analytical models.

1.3 RESEARCH STATEMENT

This research aims to create an application to efficiently consume plastic waste in infrastructure. The main research objectives are:

- (i) To identify the mechanical properties of FRP made of PET fibres.
- (ii) To establish the failure criteria of sandwich beams made of PET FRP skins and recycled PET foam cores.
- (iii) To establish load-deflection behavior of sandwich beams made of PET FRP skins and recycled PET foam cores.

The central motive of this research is to help solve the current plastic waste pollution problem without affecting the production rate of conveniently-used plastic products. Figure 1-1 summarizes each important research stage.

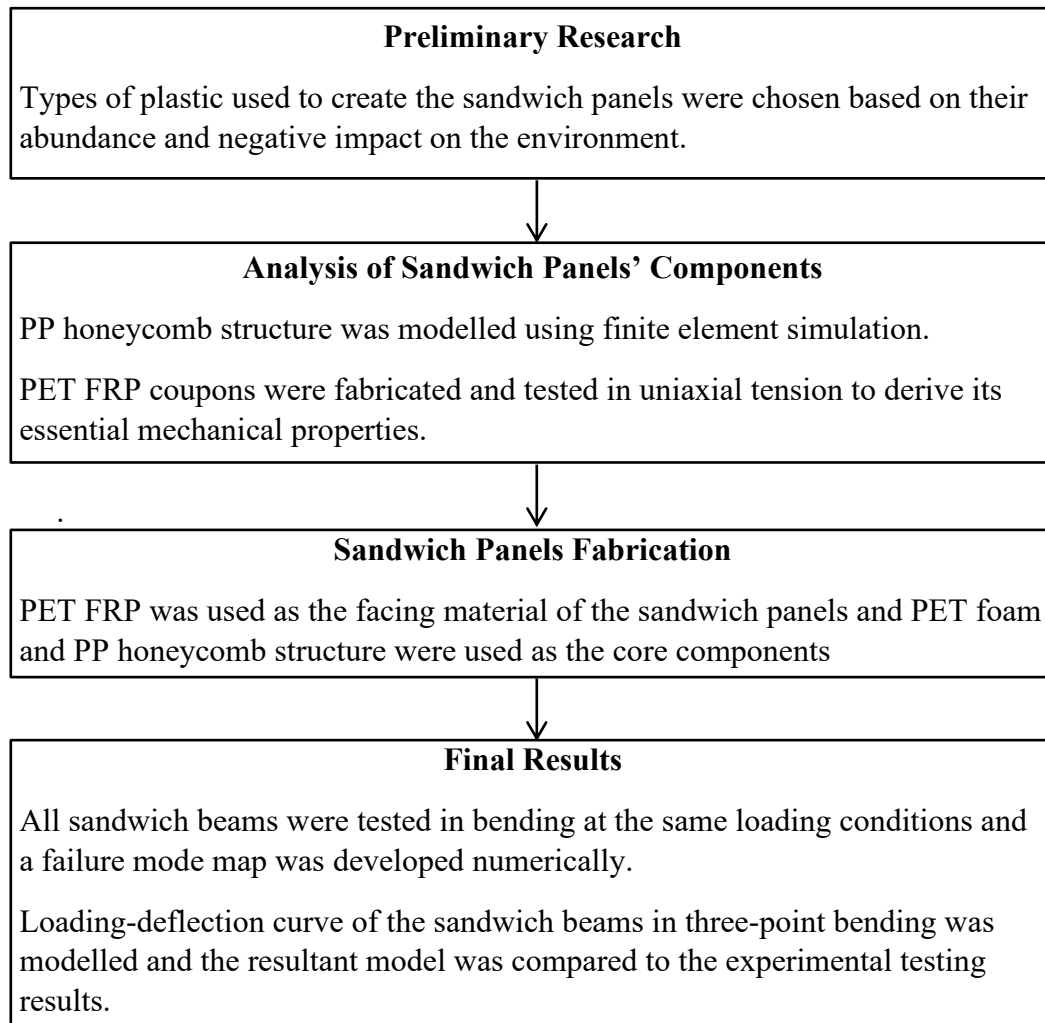


Figure 1-1 Breakdown of main research stages.

1.4 THESIS ORGANIZATION

The type of plastic used in this research was important and depended on various factors. Therefore, a full overview on plastics will be provided in Chapter 2's literature review. This overview will explain the major differences between plastic types and the cause of the current plastic waste pollution crisis impacting the planet. Additionally, Chapter 2 will include an introduction to the sandwich panels explaining their significance in ancient and modern structures.

Following the introduction and overview, Chapter 3 will contain a detailed explanation of

the manufacturing procedure of various specimens created for this research. Moreover, this chapter will present a summary of the testing setups used to obtain the mechanical properties of all fabricated elements.

The results of the laboratory study will be presented and analyzed in Chapter 4; the acquired testing data will generate results of the load-strain, moment-curvature, and load-deflection curves of the sandwich panels under three-point bending. Furthermore, Chapter 4 will present analytical models for the load-deflection relation of different sets of sandwich panels. Ultimately, analytical models will be compared to the load-deflection curves acquired through direct lab testing.

Finally, Chapter 5 will present the conclusion of this research work, summarizing major findings of all previous chapters. The conclusion will also include brief recommendations and suggestions for future studies derived from the experience obtained during this research period.

CHAPTER 2 LITERATURE REVIEW

2.1 INTRODUCTION TO PLASTICS

In 1907, an American scientist invented the first plastic polymer chain comprised entirely of synthetic molecules. His invention was intended as a substitute for natural insulators and aimed to attract the US electrical market. Shortly after its invention, plastic deduced to hold numerous superior properties intriguing many industries and became known as “the material of a thousand uses.” The term “plastic” was originally an adjective describing malleable objects, and stems from the Greek words *plastikos* and *plastos*, which translate to “form” and the “ability to be formed,” respectively. Since plastic’s foremost property was its moldability into various shapes, “plastic” then became a noun to name the material (Harrison, 2019). Around the globe, scientists witnessed the prevailing material, which accelerated motivation to invent additional forms of plastics using different chemical constituents. Thousands of unique plastic grades were introduced, each targeting a specific application depending on its mechanical and physical performance properties.

All plastic constituents possess a strong carbon-carbon bond commonly extracted from petroleum oil (Anshuman, 2018). The initial stage in plastic production is the distillation of crude oil (Palm and Svensson, 2018). During distillation, oil becomes separated into fractions with varying densities. The lightest oil products signify the lowest boiling point. Consequently, the heaviest oil products require the highest boiling point. Figure 2-1 depicts all oil products obtained through distillation along with the temperature range required for each product (EIA, 2012). The fraction of oil used as the primary building block for all plastics is called naphtha, which is achieved at a temperature range between 185-350°F.

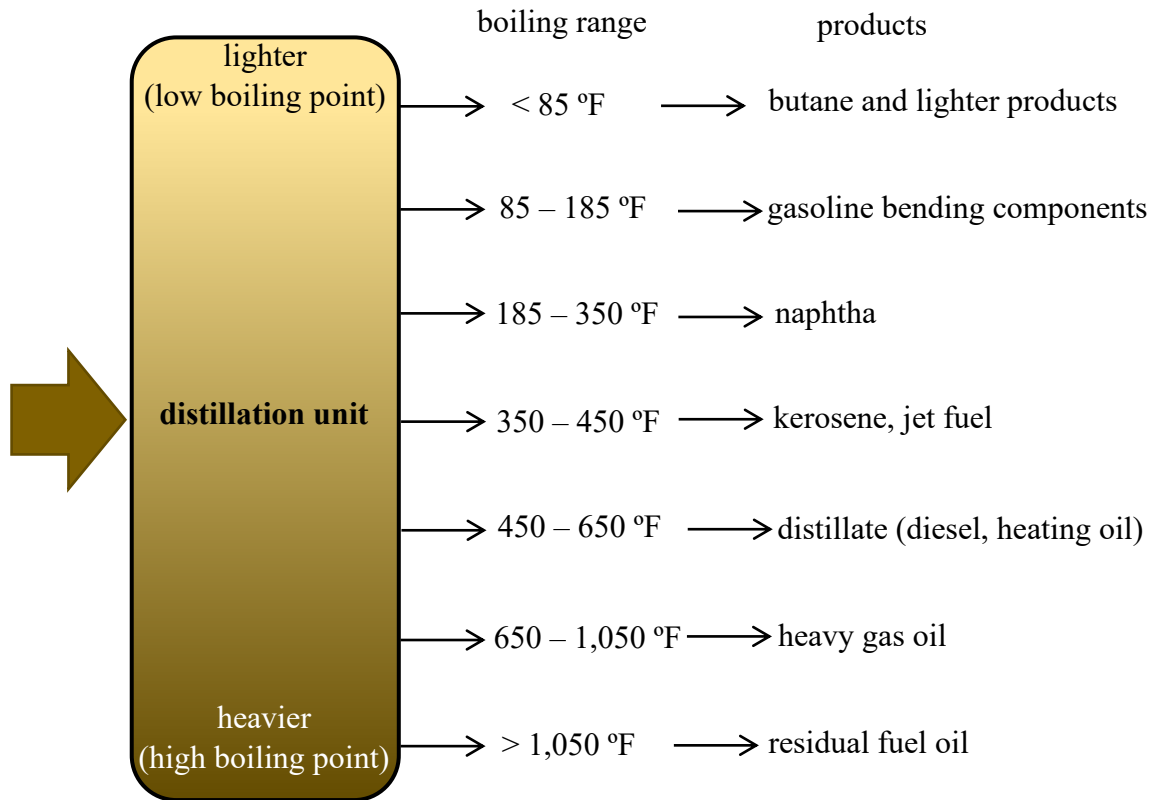


Figure 1-2 Crude oil distillation unit and products (EIA, 2012)

After distillation, a cracking process occurs to break down the long hydrocarbon chains formulating naphtha into smaller units of monomers including ethylene, propylene, and styrene (Anshuman, 2018). Ultimately, separate units are joined in the polymerization process to produce alternate types of plastic polymer chains. Despite its continuous mass production, plastic accounts for only 4-8% of global oil consumption (Palm and Svensson, 2018).

2.2 MAJOR TYPES OF PLASTIC

The chemical constituent comprising a certain type of plastic has a direct influence on its physical properties. Currently, a thousand forms of plastic—each distinguished by its monomer—hold certain properties targeting specific applications. The leading difference among varieties is the reaction towards heat exposure, which divides plastic into two main categories: thermoplastics and thermosets.

2.2.1 Thermosets

Thermosets are plastics that cannot be remolded through heat or pressure after forming (Palm and Svensson, 2018), due to strong cross-links between the polymer chains as shown in Figure 2-2.

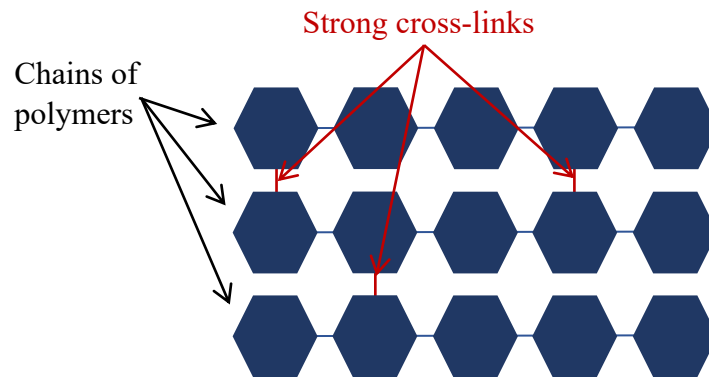


Figure 2-2 Chemical structure of thermosets.

Thermosets are divided into three categories: general use thermosets, engineering thermosets, and specialty thermosets. The qualities associated with each category depends on the intended application. Table 2-1 lists the chief products of each thermoset category. Currently, general purpose thermosets are the most produced. Despite low resistance to high temperatures—and a high coefficient of expansion—general purpose thermosets are consumed on a vast scale. This is mainly due to their average mechanical properties

existing at a comparatively low cost allowing a perfect fit for multiple applications (Dodiuk and Goodman, 2014).

Engineering thermosets are distinguished by high mechanical properties and temperature resistance. As the name suggests, these thermosets are intended for engineering applications. Epoxy and polyurethane are the most common products of engineering thermosets, which are used in producing structural and mechanical engineering elements. In modern construction, epoxy is widely used as the polymer matrix for FRPs while polyurethane (PU) creates the foam core of structural sandwich panels. Both applications consume a significant amount of this material during manufacturing. Engineering thermosets can function at temperatures higher than 400°F and maintain adhesive, thermal, and electrical resistance properties. Applications requiring a specific quality in terms of strength capacity or other forms of mechanical properties typically consume specialty thermosets, which are incredibly expensive and have the lowest production rate among thermosets.

Table 2-1 Types of thermosets and their corresponding applications

Types of Thermosets	Intended Application
Phenolics, aminos, polyesters	General Purpose Thermosets
Epoxy, polyurethane, vinyl ester	Engineering Thermosets (FRP pipes and rebars)
Silicones, polyimides, polybenzimidazoles allyls, cross-linked thermoplastics	Speciality Thermosets – applications requiring high temperatures

2.2.2 Thermoplastics

Thermoplastics are plastic types able to become remolded infinitely after forming (Palm and Svensson, 2018). At high temperatures (e.g. 300-330°C), thermoplastics soften and transform into a viscous fluid (Olagoke and Kolapo Peluola, 2016). The fluid can then be shaped into different structures. Therefore, thermoplastic properties are dependent on ambient temperatures. At a molecular level, the phase change encountered at high temperatures is due to a lack of crosslinks between plastic polymers. Despite exhibiting lower mechanical properties than thermosetting plastics, thermoplastics are produced on a much broader scale. Veritably, thermoplastics account for more than 10 percent of all chemicals produced worldwide and have a direct influence on the global economy (Olagoka and Kolapo Peluola, 2016). Furthermore, two-thirds of global plastic include thermoplastic resin (Hopewell et al., 2009).

Thermoplastics generate a vast range of products used in modern society, many of which are part of the food packaging industry (Raheem, 2013); (Palm and Svensson, 2018). The demand for thermoplastics, however, extends to the textile, aerospace, and healthcare sectors (Timm, 2018); (Stewart, 2005). In the food packaging industry, thermoplastics help extend the life of many food products through preservation and isolation from external environmental conditions (Andrady and Neal, 2009). As a result, less food is wasted annually. The three foremost aspects contributing to the use of certain thermoplastics in food packaging are: relatively cheap cost, a high strength-to-weight ratio, and non-reactivity with packaged food. Furthermore, the textile industry consumes considerable amounts of thermoplastic resins. Although fabrics made from natural fibres—like cotton—are preferred by consumers instead of synthetic fabric, the yearly

production rate of synthetic fibres made from thermoplastic materials is extraordinarily higher than natural fibres. Table 2-2 depicts the production breakdown in percentages of the world textile fibres (Discover Natural Fibres Initiative, 2019). Thermoplastics can also exist within critical and sophisticated applications, such as artificial limbs, prosthetics, and hip or joint replacements. Material use has gradually increased due to its superior properties, low cost, and simple manufacturing process.

Table 2-2 World textile fibre production (Discover Natural Fibres Initiative, 2019)

World Fibre Production				
in Metric Ton	2008	%	2018	%
Natural Fibres				
Coconut Fibres	1.056	1.4	970	0.9
Raw Cotton	23.584	31.4	26.120	23.5
Linen	533	0.7	310	0.3
Hemp	61	0.1	70	0.1
Jute	2.588	3.4	2.500	2.2
Sisal	295	0.4	210	0.2
Floss	164	0.2	164	0.1
Wool	1.198	1.6	1.080	1.0
Other Fibres	1.076	1.4	780	0.7
Total Natural Fibres	20.479	40.7	32.200	28.9
Synthetic Fibres				
Cellulose Fibres	3.464	4.6	6.900	6.2
Synthetic Fillament	25.750	34.3	49.800	44.7
Staple Fibres	15.331	20.4	22.400	20.1
Total Sythetic Fibres	44.545	59.3	79.100	71.1
Total Fibres	74.024	100.0	111.300	100.0

2.2.2.1 Types of Thermoplastics

Thermoplastics exist in various forms depending on the fundamental polymer used during manufacturing. Because differing thermoplastics are not visually distinguished, a code is

imprinted on the plastic product with a number identifying the resin used in formation.

Table 2-3 depicts the most common resin identification codes, as well as the major applications associated with each (Canadian Office of Consumer Affairs, 2019); (Hester and Harrison, 2019). Those types, along with their distinct properties, are listed and described as follows (Juran, 1989):

- Polyethylene Terephthalate (PET): This material, also known as polyester, is recognized for its toughness, impact resistance, dimensional stability, clarity, and transparency.
- High Density Polyethylene (HDPE): HDPE is a material that maintains its mechanical properties at low temperatures, which allows for use in numerous applications. Its main properties include high clarity, transparency and stiffness.
- Polyvinyl Chloride (PVC): Its main property is weatherability. This material can endure external weather conditions and variations in climate, permitting external use in structural elements. Additional mechanical benefits of PVC include low combustibility, high toughness, and low melt viscosity.
- Low Density Polyethylene (LDPE): LDPE has similar properties to HDPE. Its major property is low stiffness due to low density, which allows its use in applications requiring compressibility.
- Polypropylene (PP): This thermoplastic has various properties, including low density and high stiffness. Shortly after its discovery in 1953, polypropylene's inventors, Karl Ziegler and Giulio Natta, received The Nobel Prize in Chemistry.

- Polystyrene (PS): The major advantages of PS include its low cost and simple production process. Fortunately, these advantages outweigh certain weak properties, including low impact strength and durability.

The common advantage among all thermoplastics listed is recyclability, which distinguishes thermoplastics from thermosets. Section 2.3 will further discuss the recyclability and recycling process associated with different types of thermoplastics.

Table 2-3 Thermoplastics’ resin identification symbols, associated acronyms, full names and uses (Canadian Office of Consumer Affairs, 2019; Anon., 2015)

Symbol	Acronym	Full name and uses
 PETE	PETE	Polyethylene terephthalate - Fizzy drink bottles and frozen ready meal packages.
 HDPE	HDPE	High-density polyethylene - Milk and washing-up liquid bottles
 PVC	PVC	Polyvinyl chloride - Food trays, cling film, bottles for squash, mineral water and shampoo.
 LDPE	LDPE	Low density polyethylene - Carrier bags and bin liners.
 PP	PP	Polypropylene - Margarine tubs, microwavable meal trays.
 PS	PS	Polystyrene - Yoghurt pots, foam meat or fish trays, hamburger boxes and egg cartons, vending cups, plastic cutlery, protective packaging for electronic goods and toys.
 OTHER	OTHER	Any other plastics that do not fall into any of the above categories. For example melamine, often used in plastic plates and cups.

2.3 PLASTIC WASTE POLLUTION

Plastic pollution is currently extending from land areas to oceans and different waterbodies (Thompson & Pahl, 2019). It is difficult to distinguish the specific sources and environmental areas from where plastic waste derives (François, et al., 2017). The increasing rate of environmental plastic pollution is due to two major factors. Firstly, the over-reliance on single-use plastic products, which yields an increase in plastic's production rate. Figure 2-3 depicts the rate at which global plastic production increases, as well as the percent of applications consuming plastic since 2015 (Worm, et al., 2017). Plastic production rates have significantly changed over time. As illustrated in Figure 2-3, global plastic production rates could be divided into three major phases, and each phase features a constant increase rate. Phase 1 depicts a relatively low plastic production rate in metric tons, which occurs from the initial period of plastic discovery until 1950. For Phase 2, plastic production rates followed a sudden increased trend. For Phase 3, plastic production rates continued to progressively increase.

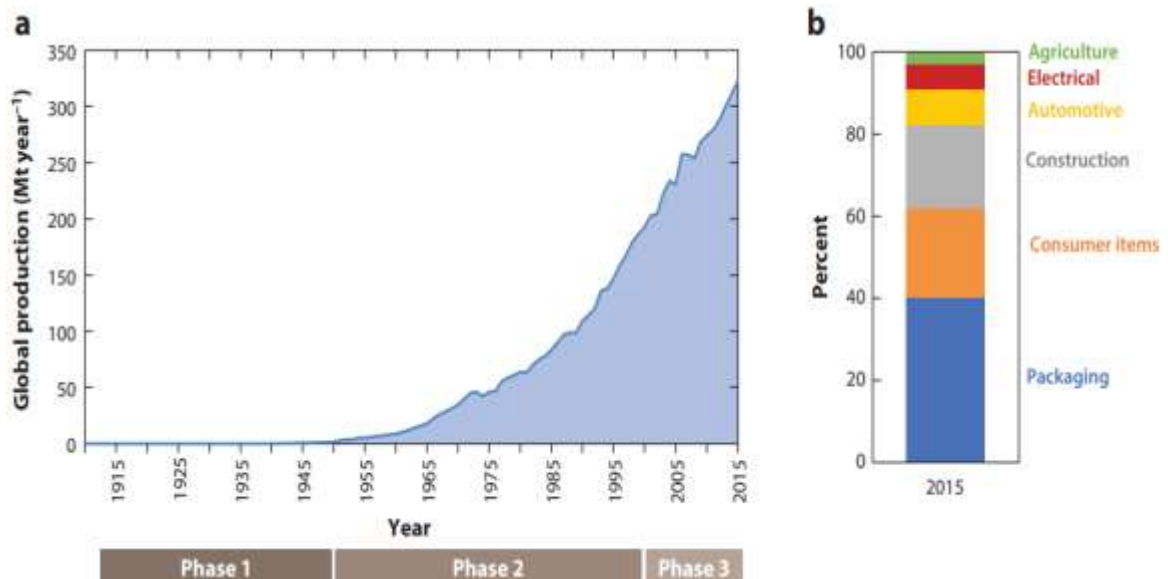


Figure 2-3 Plastic production rate over the years. (a) The three phases of plastic production rates. (b) Identification of the percentage in which each sector consumes plastic in 2015. (Worm, et al., 2017)

The second factor affecting the increase of plastic waste in the environment is related to the chemical composition of plastic molecules. These molecules are comprised from incredibly strong carbon-carbon bonds that are not biodegradable and have extremely low degradation rates (Zheng, et al., 2008). Therefore, even if the production rate was assumed constant, the amount of environmental waste will continue to increase (Thompson & Pahl, 2019). As a result, a 2015 study estimates the amount of plastic waste occupying the ocean to triple by 2025 when considering a constant rate of plastic waste generation (Jambeck, et al., 2015).

2.3.1 Environmental Impact of Plastic Waste

Post consumer plastic waste currently causes a significant negative impact on various environmental areas. It threatens marine wildlife, affects human health, and occupies large spaces in waste landfills. Plastic in the ocean is either discarded from sailboats or carried from land to the ocean and different waterbodies through river channels, wind, tides, rainwater, storm drains, direct sewage disposal, and flooding (Ryan, et al., 2009). Plastic pollution in the ocean has affected 267 different kinds of marine species (Moore, 2008) through entanglement or direct ingestion (Ryan, et al., 2009), which has caused many national leaders to focus on developing a plan mitigating plastic marine pollution. Under the theme of “working together on climate change, oceans and clean energy,” Canadian Prime Minister, Justin Trudeau, has organised ministerial meetings regarding plastic waste reduction. The series of arranged meetings focus on the impact of plastic pollution, and marks the first step in addressing Canada's contribution, which could possibly influence neighboring countries (Government of Canada, 2017). On World Environment Day, the United Nation’s Secretary, General Antonio Guterres, spoke solely about plastic pollution.

His only request was to “beat plastic pollution” (United Nations, 2018). This highlights the extent of plastic pollution problematically and rapidly growing into an environmental crisis.

2.3.1.1 Entanglement of Marine Organisms

Entanglement occurs when a marine organism attempts to pass through a closed loop plastic waste smaller than its body (Laist, 1997). As a marine organism swims farther or dives deeper, water currents push the loop and cause the organism great struggle.

Additionally, as the marine organism grows, the plastic entanglement begins to affect its mobility and natural shape structure. Figure 2-4 depicts commonly used news and media photos to emphasize the effects of entanglement. As shown in the Figure 2-4, plastic waste can entangle different types of species of varying sizes, and each incident has its own impact on the affected organism.

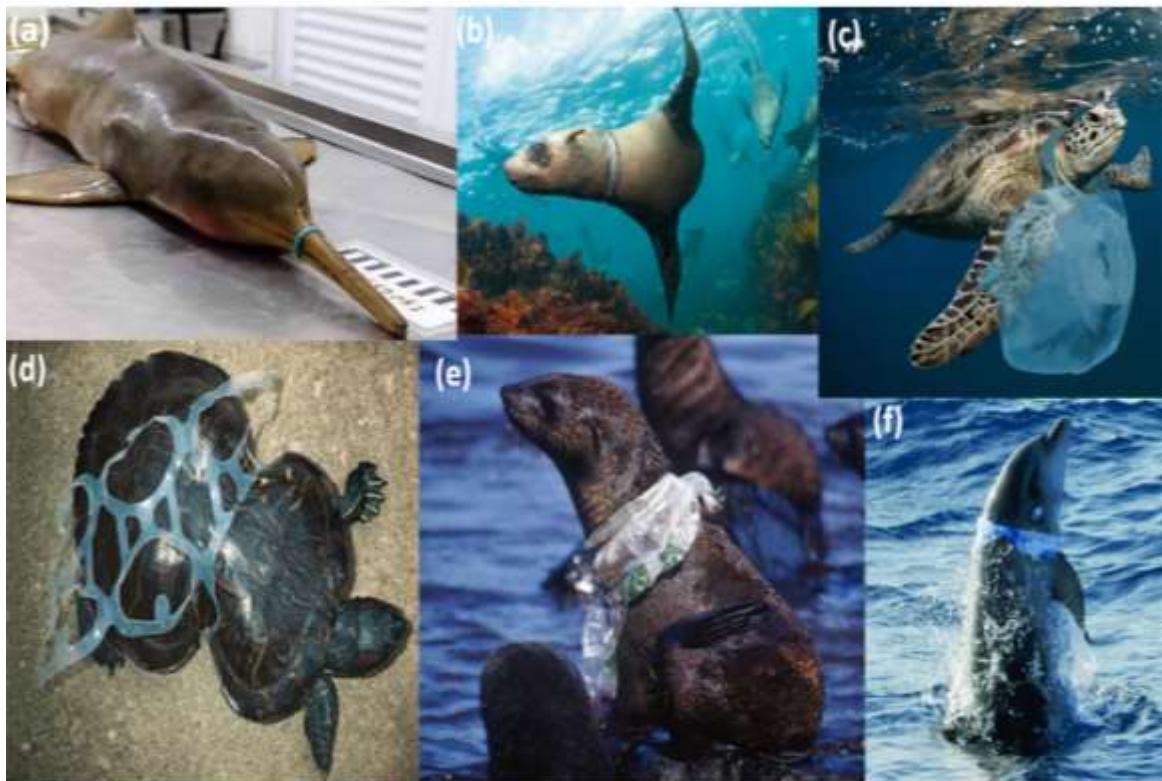


Figure 2-4 The effect of entanglement on marine organisms (a) (Larson, 2018) (b) (Sinclair, 2014) (c) (Shelton, 2019)(d) (Leavy, 2018) (e) (Kelly, 2016) (f) (Groves, 2019)

Harmful entanglement effects on marine species include: starvation due to the disability of biting or chewing food, as shown in Figure 2-4 (a); disability of growing correctly, as has happened to the turtle shown in Figure 2-4 (d); immobility from an accumulation of plastic waste on an organism's body, leastly causing discomfort to the species as shown in parts (b, c, e, f) of Figure 2-4.

2.3.1.2 Ingestion by Marine Organisms

Plastic debris ingestion by marine organisms occur on a larger scale compared to entanglement. Marine organisms and seabirds often mistake plastic with food (Hammer, et al., 2016), which causes digestive problems and, ultimately, starvation from the false feeling of fullness or satiation (Wright, et al., 2013). Plastic floating in different waterbodies tends to attract seabirds searching for food. This phenomenon has caused over 90% of the seabird population to have plastic pieces in their stomach (Smith, 2018). Figure 2-5 depicts multiple forms of organisms who fell victim to plastic ingestion. As shown in parts (a) and (b), plastic particles ingested did not decompose even after death and the decomposition of the organism. As the amount of plastic ingested by fish increases, humans become more susceptible to consume plastic. Although eating wild fish might be a primary route for plastic to reach humans, it is not the only source. Researchers have discovered plastic in sea salt, honey, and beer (Smith, et al., 2018), which highlights the impact of exposing plastic to the environment and its capacity to reach and affect human health.

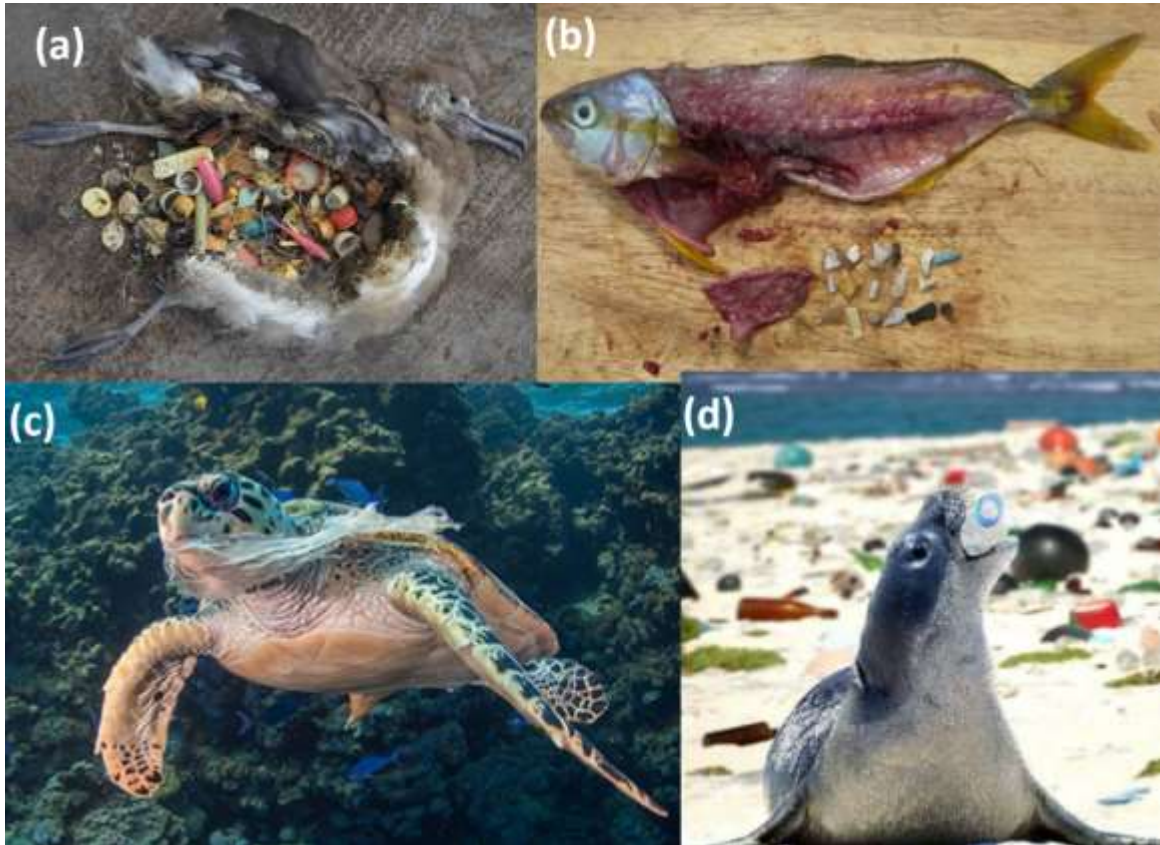


Figure 2-5 Examples of marine organisms and seabirds that were victims of plastic ingestion (a) (Lofgren, 2014) (b) (Thompson, 2018) (c) (Wilson, 2017) (Shelton, 2019) (d) (Anon., 2019)

2.3.1.3 Plastic Waste in Landfills

Presently, 86% of plastic waste generated in Canada is kept in landfills (Wuennenberg & Tan, 2019). This large percentage accounts for a loss in valuable landfill space, which will be preoccupied for a significant amount of time due to plastic's low decomposition rate. Plastic waste in landfills could also lead to the release of hazardous chemicals and bio-aerosols in the environment (Mudgal, et al., 2011). Table 2-4 depicts the increased trend of plastic waste disposal into US landfills within the past 50 fifty years, and also compares plastic disposal rates to other waste occupying landfills (Macpherson, 2014).

Table 2-4 Materials discarded in United States landfills from 1960 to 2010 (in thousands of tons) (Macpherson, 2014).

Wastes	1960	1970	1980	1990	2000	2005	2010
Paper and Paperboard	24,916	37,540	43,420	52,500	50,180	42,880	26,740
Glass	6,620	12,580	14,380	10,470	9,890	9,950	8,400
Metals	10,770	13,350	14,290	12,580	12,340	13,400	14,540
Plastics	390	2,900	6,810	16,760	24,050	27,470	28,490
Rubber and Leather	1,510	2,720	4,070	5,420	5,850	6,200	6,610
Textiles	1,710	1,980	2,370	5,150	8,160	9,670	11,150
Wood	3,030	3,720	7,010	12,080	12,200	12,960	13,580
Other Materials ^b	70	470	2,020	2,510	3,020	3,080	3,380
Food Scraps	12,200	12,800	13,000	23,860	29,130	31,300	33,790
Yard Trimmings	20,000	23,200	27,500	30,800	14,760	12,210	14,200
Miscellaneous Inorganic Wastes	1,300	1,780	2,250	2,900	3,500	3,690	3,840
Total MSW Discarded	82,516	113,040	137,120	175,030	173,080	172,810	164,720

2.3.2 Benefits of Plastic

Plastic contributes several important benefits to the society and the environment that many individuals, including environmental activists, are not aware of. Since its inception, plastic has become a part of applications that enhanced humankind's quality of life (Hidayah & Syafudin, 2018). After being publicly presented as a major source of environmental pollution, several studies were conducted on plastic aiming to estimate and review its pros and cons with respect to other materials such as glass, metals, and paper. According to a report published by the European Association of Plastic Manufacturers, approximately 19% of all plastic products cannot be replaced by non-plastic materials without a significant aspect changes in the product's design. Additionally, the report's assessment concludes that substituting plastic with non-plastic materials will consume 26% more energy and generate

56% more greenhouse gases to the environment during product lifecycles (Pilz, et al., 2005).

Plastic is used very commonly in packaging food and beverage containers. Despite criticism regarding its waste abundance in the environment, this application prolongs the life of the packaged food, which ultimately reduces the amount of food waste. According to the Food and Agriculture Organization (FAO) of the United Nations (UN), approximately one-third of all globally produced food is lost or wasted (FAO, 2011). This illustrates societal need to extend expiration dates of produced food to avoid the waste issues. When discarded in landfills, food releases greenhouse gases, imposing a catastrophic impact on climate (Hidayah & Syafudin, 2018).

Plastic bags—primarily used in the grocery market—are another commonly used plastic product reputed to negatively impact the environment. Intended as an effort of distinguishing the optimum option of bags to replace plastic ones, the Danish government conducted an extensive study on various types of carrier bags. The study concluded that the amount of carbon emissions associated with plastic bags are significantly lower than all other options. The report suggests that a consumer needs to reuse a cotton bag at least 7,100 times and a paper bag at least 870 times for each to impose a lower impact on the climate change and other indicators. In Table 2-5, “all indicators” refer to environmental consequences, besides climate change, including ozone depletion, human toxicity cancer and non-cancer effects, photochemical ozone formation, ionizing radiation, particulate matter, terrestrial acidification, terrestrial eutrophication, marine eutrophication, freshwater eutrophication, ecosystem toxicity, resource depletion, fossil and abiotic, and depletion of

water resource (Bisinella, et al., 2018). In summary, plastic produces durable and high-performance materials at a significantly low price and weight, and due to those properties—according to a report by the Canadian Council of Ministers of the Environment (CCME)—plastic currently and significantly benefits the Canadian economy (CCME, 2018).

Table 2-5 Number of times different types of carrier bags need to be reused to provide the same environmental performance of the average LDPE carrier bags (Bisinella, et al., 2018).

	LDPE average, reused as waste bin bag	
	Climate Change	All indicators
LDPE simple, reused as waste bag	0	1
LDPE rigid handle, reused as waste bag	0	0
Recycled LDPE, reused as waste bag	1	2
PP, non-woven, recycled	6	52
PP, woven, recycled	5	45
Recycled PET, recycled	8	84
Polyester PET, recycled	2	35
Biopolymer, reused as waste bag or incinerated	0	42
Unbleached paper, reused as waste bag or incinerated	0	43
Bleached paper, reused as waste bag or incinerated	1	43 ⁴
Organic cotton, reused as waste bag or incinerated	149	20000
Conventional cotton, reused as waste bag or incinerated	52	7100
Composite, reused as waste bag or incinerated	23	870

⁴ The highest value for bleached paper is set to as minimum be equal to the value for unbleached paper.

2.3.3 Solutions to Plastic Waste Pollution

As problems caused by plastic pollution are increasing and expanding globally, vast efforts are made to distinguish solutions to help resolve issues. One suggested approach is the use of natural plastic or bioplastics. Unlike conventionally used petroleum-based plastic, these

forms are composed of polymers obtained from agricultural by-products such as corn, soy bean, and sugarcane (Pathak, et al., 2014). According to plastic consumers, bioplastics are ecofriendly with respect to conventionally used plastic because of their degradability and composability properties. Individuals witnessing the effect of non-degradable plastic waste on marine life have strongly encouraged and defended the use of bioplastics. However, if considering the chemical reaction occurring during degradation, bioplastics appear as a “misguided solution” (Washam, 2010). The decomposition reaction of bioplastic is shown in Equation (2-1); the product of bioplastic decomposition releases methane and carbon dioxide. Both compounds, when released to the atmosphere, will have a heating effect that contributes to climate change (Reay, et al., 2012).

Additionally, despite a composition from renewable resources, the bioplastic production process consumes fossil fuels to power machines generating its products. Harvesting crops used for bioplastics also has hidden environmental costs, including the use of toxic pesticides in processes and carbon emitted from agricultural machinery. Furthermore, bioplastics are more expensive than petroleum-based plastic.



2.4 RECYCLING OF PLASTIC WASTE

Recycling plastic waste is considered a practical solution to address current plastic pollution. There are two methods for plastic waste recycling. Firstly, chemical recycling yields plastic resin identical to the mechanical qualities to disposed plastic. Despite producing high-quality products, chemical recycling is not favoured due to its long process involving energy consumption at high cost. Moreover, the final product cost generated from

chemical recycling plants often exceeds the price of brand-new plastics (Hopewell, et al., 2009).

Secondly, the mechanical recycling process involves a series of mechanical steps including: shredding, washing, drying, and separating, as illustrated by Figure 2-6. This method aims to refine plastic waste, preparing it for remolding. Mechanical recycling costs less than chemical recycling, therefore it happens on a much larger scale.

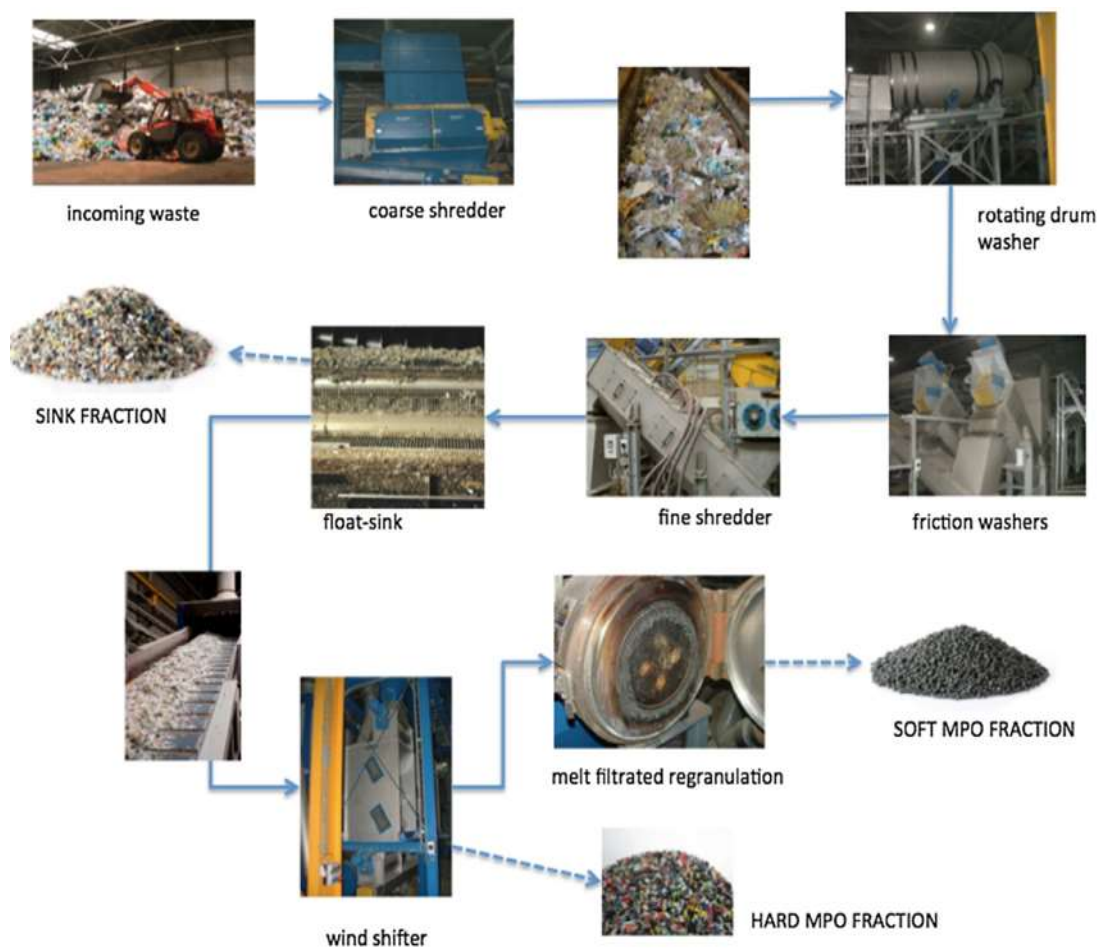


Figure 2-6 Mechanical recycling process of thermoplastic waste (Ragaert, et al., 2017).

Since plastic production rates have increased within the past few years, many attempts have aimed to create a valid product to consume post-mechanical recycled plastic resin. At Massachusetts Institute of Technology (MIT), a specific grade of postconsumer plastic was used in the form of powder as an additive to concrete mix. The resultant concrete mix revealed to have superior properties compared to conventionally used concrete (Chu, 2017). At many other institutes, research has focused on using plastic waste for infrastructural applications, and its main objective is the reduction of plastic pollution through consumption of large plastic waste quantities.

Plastic foam is among the most innovative products of recycled plastic currently used for numerous structural applications. Recycled plastic foam can consume large quantities of plastic waste and is currently a part of various industries including wind energy, construction, and transportation. Regarding the construction industry, plastic foam is incorporated in air ducts, façade cladding, external thermal insulation composite system (ETICS), roof structures, and structural flooring (Armacell, 2018). In 2019, a house in Meteghan River, Nova Scotia, was built utilizing over 600,000 post-consumer plastic bottles as recycled foam (Comeau, 2019). Figure 2-7 depicts the house during its construction stage, where recycled foam was used as part of façade cladding and roof structure.



Figure 2-7 Meteghan River house under construction made using foam recycled from plastic (Comeau, 2019).

2.5 INTRODUCTION TO SANDWICH PANELS

A sandwich panel is a composite structure consisting of two face-skin sheets and a core section. The core's main structural purpose is to increase the panel's bending stiffness by increasing the distance separating the face-skins. The top and bottom facings of the sandwich structure are designed to resist bending forces (i.e. forces in tension and compression that result during bending). Therefore, the core component of a sandwich structure is made from a lightweight/low-dense material. Meanwhile the facings are made from an element with high stiffness and strength properties.

2.5.1 Mechanics of Sandwich Composites

The mechanical behavior of a sandwich structure can be analysed by modelling a simply supported sandwich beam in three-point bending, similar to the image in Figure 2-8.

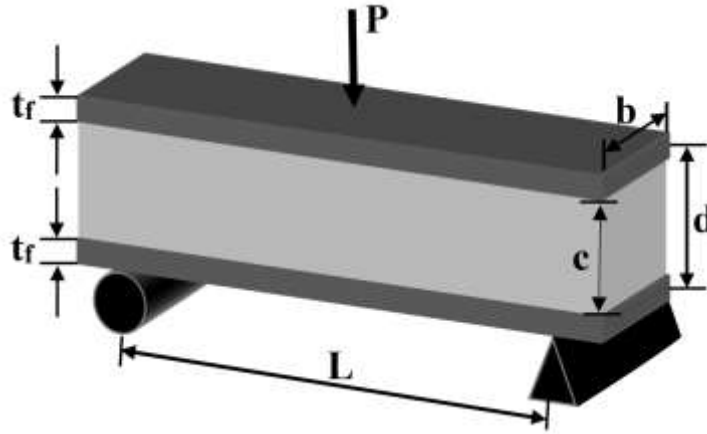


Figure 2-8 Sandwich beam loaded in three-point bending.

The equivalent flexural rigidity, $(EI)_{eq}$, can be derived from the elastic modulus of the facing material, E_f , and the elastic modulus of the core material, E_c using the parallel axis theorem. Sandwich panel's facing component is typically very thin—with respect to the panel's cross section—and the core's modulus term is much smaller than the facings' moduli; thus, equivalent flexural rigidity can be simplified as follows:

$$(EI)_{eq} = \frac{E_f b t_f^3}{6} + \frac{E_c b c}{12} + \frac{E_f b t_f (c + t_f)^2}{2} \longrightarrow \frac{E_f b t_f c^2}{2} \quad (2-2)$$

In which, “ t_f ” is the thickness of the facing component, “ c ” is the thickness of the core component, “ E_f ” is the modulus of elasticity of the facing component, “ L ” is the distance between the supports, “ d ” is the distance between facing centroid and “ b ” is the width of the sandwich panel as shown in Figure 2-8.

The equivalent shear rigidity term, $(AG)_{eq}$, can be derived from the shear modulus of the core component, G_c , using the following equation (Allen, 1969):

$$(AG)_{eq} = \frac{G_c b d^2}{d} = G_c b d \quad (2-3)$$

2.5.1.1 Normal Stresses

As the beam bends under the applied load, P , normal stresses in the facing (σ_f) and core (σ_c) will be developed, as described in the following equations (Allen, 1969):

- Stress in facing component: $\sigma_f = \frac{\left(\frac{PL}{4}\right)y E_f}{(EI)_{eq}} = \frac{M}{b t_f c} \quad (2-4)$

- Stress in core component: $\sigma_c = \frac{\left(\frac{PL}{4}\right)y E_c}{(EI)_{eq}} = \frac{M}{b t_f c} \frac{E_c}{E_f} \quad (2-5)$

Moreover, following the same assumptions used in estimating the equivalent flexural rigidity term, shear stress is estimated as constant throughout the core's cross-section, and linear through the facings. Therefore, the shear stress along the core is obtained through the following formula:

$$\tau_c = \frac{V}{b d} \quad (2-6)$$

In which, $V = \frac{P}{2}$ for three-point bending configuration.

Figure 2-9 shows the normal and shear stress distribution along the sandwich panel's cross-section respectively and justifies the approximations considered in the above formulas (Zenkert, 1997).

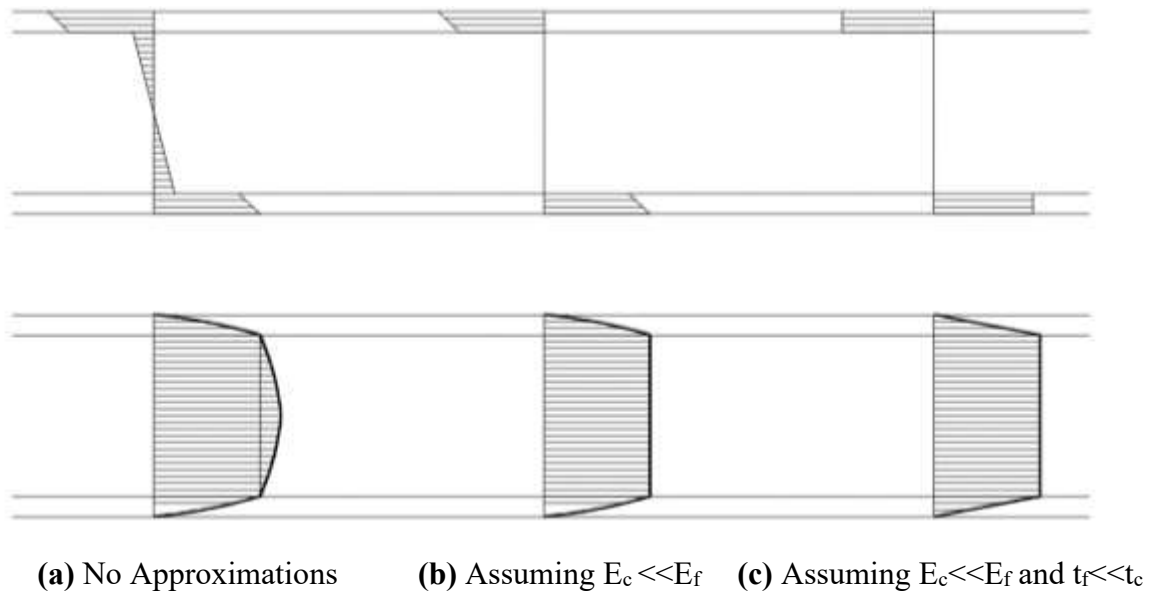


Figure 2-9 Stress distribution along the beam's cross-section (Zenkert, 1997).

2.5.1.2 Deflection

When the load is applied on the mid-span length of the sandwich beam, it will start deflecting. The total deflection at midspan, δ_i , sustained by the beam is a sum of the deflection due to shear at midspan, δ_s , and the deflection due to bending at midspan, δ_b . Shear deflection corresponding to the facings is insignificant and therefore is not considered in the shear deflection calculation. Figure 2-10, demonstrates the breakdown of the total deflection into bending and shear deflections of a sandwich panel under three-point bending (Betts, et al., 2018).

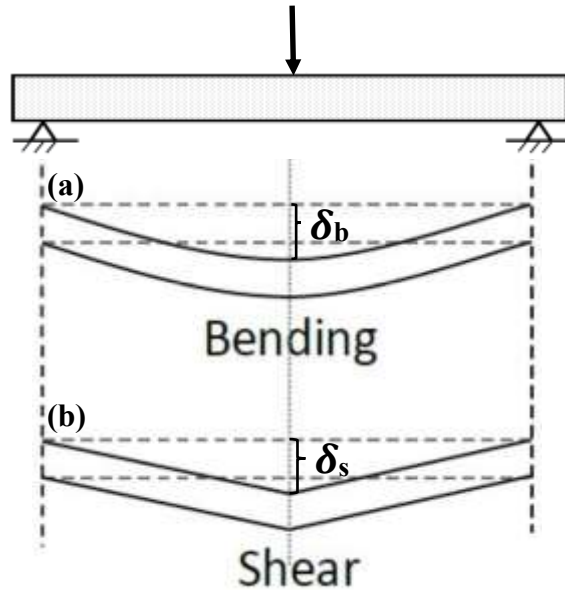


Figure 2-10 Breakdown of total deflection into (a) bending deflection and (b) shear deflection (Betts, et al., 2018)

The midspan total deflection of the beam under applied load is obtained using the following equation:

$$\delta_t = \delta_b + \delta_s = \frac{PL^3}{48(EI)_{eq}} + \frac{PL}{4(AG)_{eq}} \quad (2-7)$$

2.5.1.3 Curvature

The total deflection (i.e. sum of shear and bending deflections) of a simply supported beam varies along its span length. Beams deform into a curve along their longitudinal axis under loading; hence, maximum deflection exists in beam sections farthest away from support(s). This section will include a comprehensive derivation of the curvature equation used in Chapter 3's analysis section.

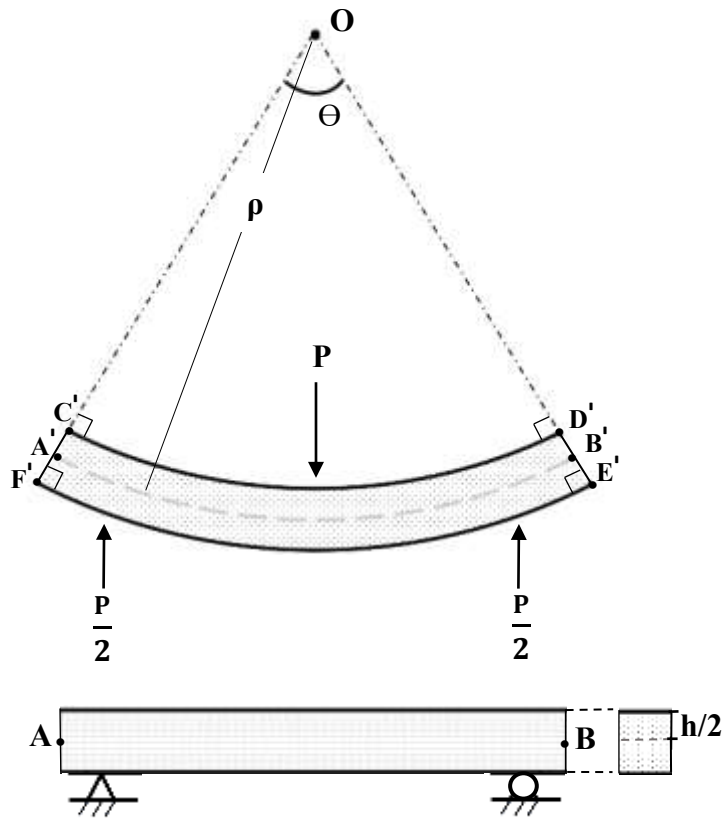


Figure 2-11 Cross-section of deformed beam under pure bending.

Curvature is defined as the reciprocal of the curve's radius. The fundamental assumption used in deriving curvature is that the shear deformation is negligible; therefore, the cross section remains perpendicular to the bending line as shown in Figure 2-11. As the beam bends further under an applied load the curve's radius, ρ , will decrease and curvature, ψ , will increase. Considering a sandwich structure similar to the one represented in Figure 2-10, for a given radius and central angle, Θ —to which the sandwich beam is bending—the beam length measured at its neutral axis (i.e. the distance of arc length $A'B'$) can be calculated using the following mathematical equation:

$$A'B' = \rho \Theta \quad (2-8)$$

In which Θ must be measured in radians.

Similarly, the arc length of the top and bottom faces of the sandwich panels after bending is equivalent to:

- Arc length of top face after deflection: $C'D' = (\rho - h/2) \Theta$ (2-9)

- Arc length of bottom face after deflection: $E'F' = (\rho + h/2) \Theta$ (2-10)

Substituting ρ with $1/\psi$, equation of curvature can be written as shown below:

$$\psi = \Theta / A'B' \quad (2-11)$$

Beams used for structural engineering applications are designed with a slight deflection capacity. Therefore, $A'B'$ is approximately equivalent to AB .

Strain, ϵ , is defined as the ratio between the deformed length to the original length.

Subsequently, the top and bottom strains of the sandwich panel are denoted as follows:

$$\epsilon_{\text{top}} = \frac{\text{Deformation of top face length}}{\text{Original face length}} = \frac{AB - C'D'}{AB} = \frac{\rho \Theta - (\rho - \frac{h}{2}) \Theta}{\rho \Theta} = \frac{h}{2\rho} = \psi \frac{h}{2} \quad (2-12)$$

$$\epsilon_{\text{bottom}} = \frac{\text{Deformation of bottom face length}}{\text{Original face length}} = \frac{F'E' - AB}{AB} = \frac{(\rho + \frac{h}{2}) \Theta - \rho \Theta}{\rho \Theta} = \frac{h}{2\rho} = \psi \frac{h}{2} \quad (2-13)$$

The sum of the top and bottom strains simplifies to:

$$\epsilon_{\text{top}} + \epsilon_{\text{bottom}} = \psi \frac{h}{2} + \psi \frac{h}{2} = \psi h \quad (2-14)$$

Finally, curvature is derived from the sum of top and bottom strains equations:

$$\psi = \frac{\epsilon_{\text{top}} + \epsilon_{\text{bottom}}}{h} \quad (2-15)$$

2.5.2 History and Applications of Sandwich Structures

Sandwich structures exist throughout history and are very common in nature and living organisms (Gibson & Ashby, 1999). The human skull, as shown in Figure 2-12, is essentially a sandwich structure composed of a porous bone layer sandwiched between two rigid bone layers. Bones in legs and arms are another example of sandwich structure in human anatomy. The significance of those structures within a living organism is related to their ability to endure various complex loading conditions of repetitive tension, compression, and bending while being light in weight (Thomsen, et al., 2005).

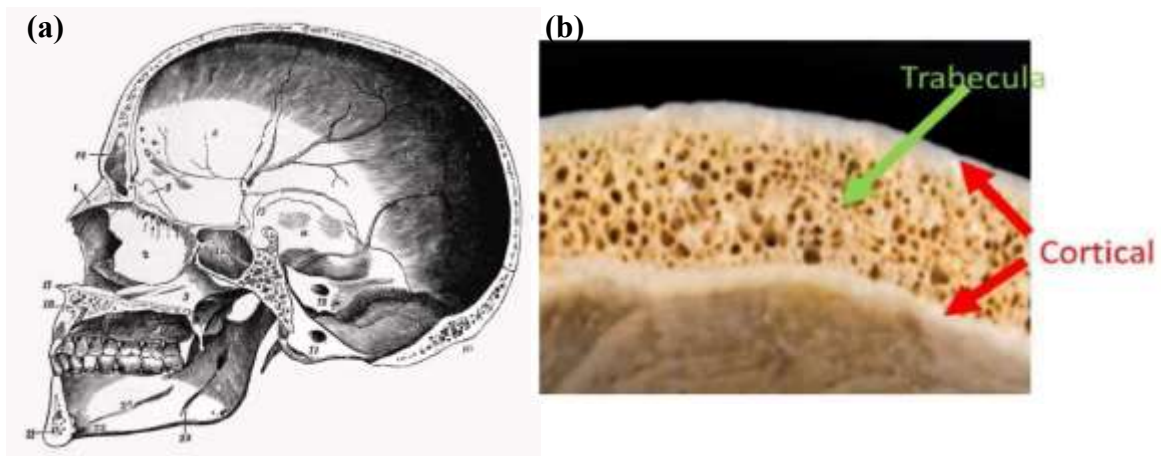


Figure 2-12 Sandwich structure in human anatomy. (a) Cross-sectional view of human skull (source: fineartamerica.com) (b) Bones of the sandwich structure within a human skull (Wang, et al., 2014).

The mechanical concept of sandwich structures was first understood in the early 1800s. A Frenchman, Duleau, discovered that strength and stiffness of a built-up beam (as shown in Figure 2-13) made from spaced bolted bars increased as the spacings, s , of bolts supporting the bar increased (Timoshenko, 1953). This concept analysis led to the first construction of steel I-beams and later to the commercially-used sandwich panels (Timoshenko, 1953; Kuen, 1959).

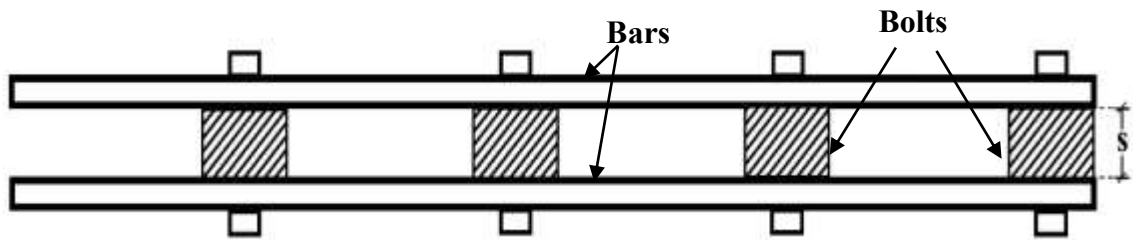


Figure 2-13 Side view sketch of the built-up beam used in Duleau's experiments (Timoshenko, 1953).

In recent years, sandwich panels have been extensively used to create complex structures with a high strength-to-weight ratio. When designing a sandwich panel, the mechanical and physical properties of the components making up the sandwich structure should be considered and the material choice becomes governed by properties required through the intended application. In civil engineering, sandwich panels are primarily used as exterior walls/facades or roof panels, as shown in Figure 2-14. Therefore, the core component is chosen based on its insulation properties to satisfy that requirement. When sandwich panels are used in a mechanical engineering application, like being part of helicopter rotter blades, skin-facings require resistance to weather condition changes. Hence, various application-specific design aspects always govern the choice of materials completing the final composite product.

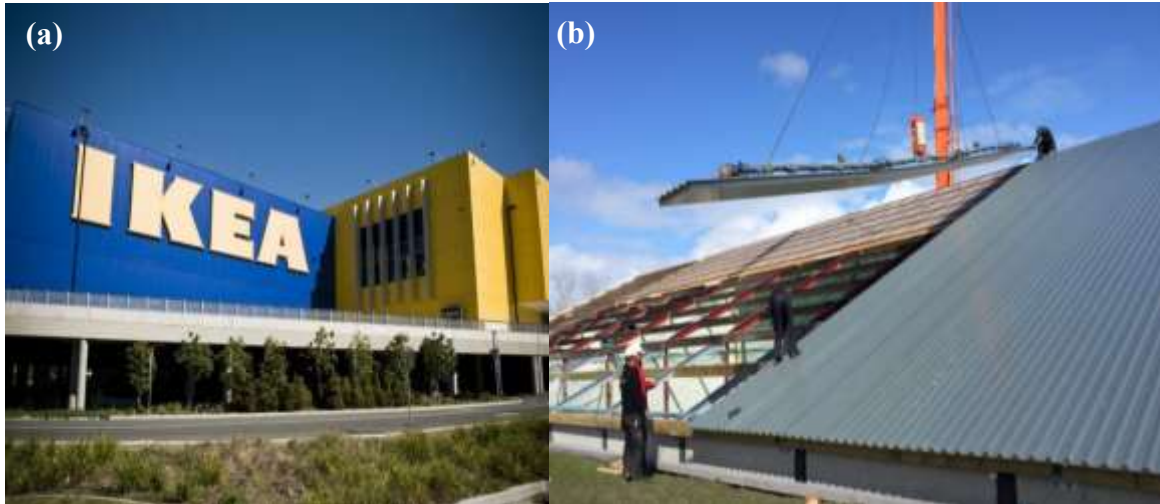


Figure 2-14 Sandwich panels in civil engineering (a) Exterior Walls - Ikea Doha in Qatar, Ikea Bratislava in Slovakia and Ikea Bayonne in France (Source: bondor.com) (b) Roof Panels - Geusselt football stadium in the Dutch town of Maastricht (Source: viavac.com)

2.5.3 Design Criteria of Sandwich Panels

The two primary aspects considered during the sandwich panel design stage are the choice of material used for the core and facings components, and the dimensions of those components. When a sandwich panel's intended application is defined and, accordingly, the choice of material is selected (Zenkert, 1997) the final design stage is specifying its cross-sectional dimensions. Here, the panel's failure mode should be considered to produce optimum design regarding material consumption.

2.5.3.1 Failure Modes of Sandwich Panels

During the design stage of new construction projects, the designing engineer anticipates and accounts for the failure mode of each structural element. When conventionally used materials are then designated, the engineer must then typically account for only one failure mode. In doing so, designers can avoid brittle collapses and also allows control of the mechanism in which the structure fails at its ultimate strength capacity. There are

numerous mechanisms for which sandwich panels can fail. This is primarily because panels are made by bonding components (i.e., facings and core) with material properties that vary significantly in strength and mechanical performance capacities. The most common modes of failure for sandwich panels (illustrated in Figure 2-15) are face yield/fracture, core shear, and face wrinkling.

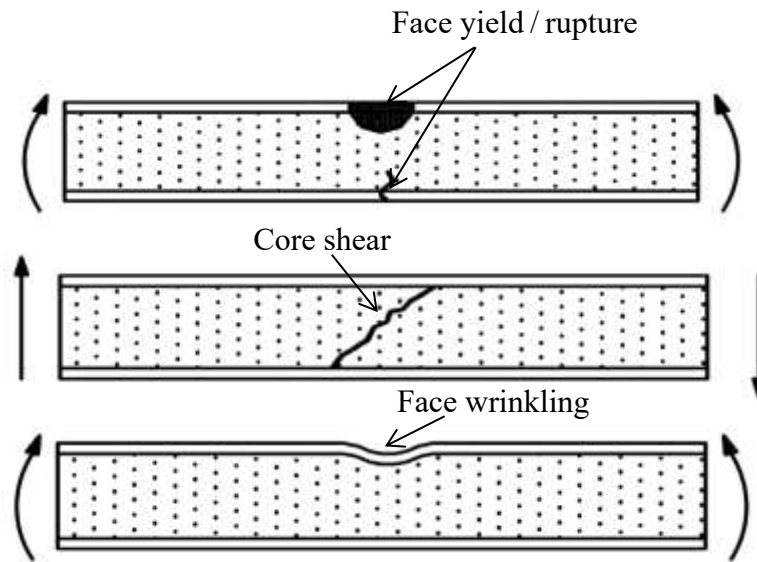


Figure 2-15 Failure modes sandwich panels (Zenkert, 1997).

2.5.3.1.1 Face Yielding or Rupture

Generally, when the facing component is significantly weaker than the core, the expected mode of failure of the sandwich panel will be “face yielding” or “face fracture,” depending on its material. Metals, such as steel and aluminum, would yield but fibre composites would fracture and rupture more suddenly.

Assuming that the flexural stresses are uniform and carried out by the facing component, the ultimate failure load initiating face rupture for a sandwich panel under three-point bending is equivalent to:

$$P_{FR} = \frac{4 \sigma_f t_f db}{L} \quad (2-16)$$

2.5.3.1.2 Core Shear

Core shear will most commonly occur in sandwich structures with large core thickness, and/or low core density. This mode of failure is incredibly common in engineered applications since most applications use stiff metals or fiber composites—which is significantly stiffer than the core—as the facing component material. The following formula is used to calculate the ultimate failure load initiating core shear of a sandwich panel under three-point bending configuration:

$$P_{CS} = 2 E_c db \quad (2-17)$$

2.5.3.1.3 Compression Face Wrinkling

Face wrinkling occurs when the compressive face of a sandwich panel reaches a local instability stress (Allen, 1969). Therefore, ultimate failure load initiating wrinkling is dependant on both the core and face components of the sandwich structure as shown in following equation:

$$P_{FW} = \frac{4t_f db}{2L} \sqrt[3]{E_f E_c G_c} \quad (2-18)$$

2.5.3.1.4 Failure Mode Map

Using the three equations listed above that are associated with the failure strength of sandwich panels, a graphical representation of the failure modes and the transition between each mode can be produced as a map. The equations were slightly altered by adding the core density term to the strength relationship in order to produce a map that is beneficial for designers. Hence, a designer can use the failure mode map (FMM), similar to the one shown in Figure 2-16, in the preliminary design stage to estimate the thickness of the facings and the density of the core required to achieve a specific failure mode (Zenkert, 1997).

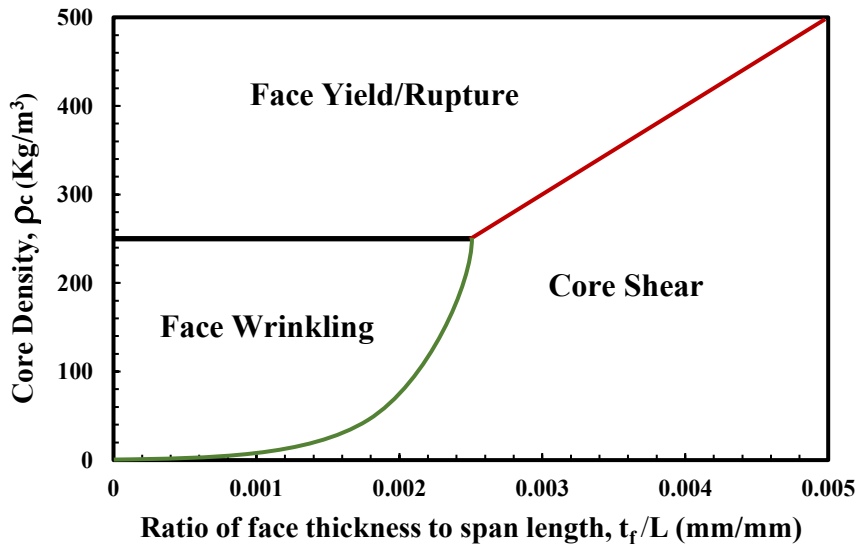


Figure 2-16 Failure modes map of a sandwich panel set

CHAPTER 3 EXPERIMENTAL PROGRAM

3.1 GENERAL STRATEGY

This chapter will cover the manufacturing procedure of the sandwich specimens and FRP coupons, and the testing set-up used to evaluate related strength properties and mechanical behavior. The test matrix, describing the changing parameters among the fabricated sandwich panels, will be included. Additionally, post-testing results—such as the mode of failure for each set of sandwich panels at peak load—will be reported and analysed. Ultimately, data acquired from different sets of tested specimens will be compared.

3.2 TEST MATRIX

The difference between the sets of sandwich specimens were the materials used for facings and core components, as well as the foam core density, which range from 70 kg/m³ to 100 kg/m³. The facing components were made from GFRP or PET FRP sheets with a 3 mm thickness. The core was made from either PP in the honeycomb structure form and a density of 80 kg/m³, or PET in the foam form with varying densities. The dimensions of all sandwich panel sets were kept constant. Furthermore, the cross-sectional width (w) and height (h) of the panels were 78 mm and 82 mm, respectively. The honeycomb structure is composed of PP circular tubes (3 mm thick) that are adhesively bonded. Adversely, the foam core is extruded from recycled PET pellets obtained from post-consumed plastic bottles. Table 3-1 lists all sets of sandwich panels tested for this research and describes the major difference among the sets. As indicated in the table, three identical specimens were tested from each set to confirm testing results. In total, 18 sandwich panel specimens were fabricated and tested in three-point bending.

Table 3-1 Test Matrix

Set Number	Facing Material	Core Material	Core Structure	Core Density (kg/m³)	Number of Identical Specimens
1	PET FRP	PP	Honeycomb	80	3
2	GFRP	PP	Honeycomb	80	3
3	PET FRP	R-PET	Foam	70	3
4	PET FRP	R-PET	Foam	80	3
5	PET FRP	R-PET	Foam	100	3
6	GFRP	R-PET	Foam	100	3
Total number of specimens					18

3.3 MATERIAL PROPERTIES OF SANDWICH FACING

Prior to testing the sandwich panels in bending, the facings' material properties were obtained by testing PET FRP and GFRP coupons in uniaxial tension. Analysing the mechanical properties of a sandwich panel's components—through identifying their load-bearing behavior—is critical to anticipate the sandwich panel's peak strength. Ultimately, this affects the panel's design aspects and machine selected while testing beams in bending.

3.3.1 Fabrication of FRP Coupons

Fibre reinforced polymer (FRP) consists of a polymer matrix reinforced with fibres. Epoxy resin (West System 105) and hardener (West System 206) were the polymer matrix of FRP coupons. The two types of fibres used were glass and PET; both fibres were woven into unidirectional fabric by the manufacturer. Unidirectional glass fabric was obtained from Anjie Glass Fibre Fabrics (China) and unidirectional PET fabric was

purchased from Maeda Kosen Ltd. (Japan). As shown in Figure 3-1, PET FRP composite coupons were made by combining a unidirectional PET fabric with an epoxy and hardener in a wet lay-up process.

After curing the composite for four days at room temperature, it was cut into coupons (250 mm x 25 mm). The curing conditions noted above were established by the manufacturer of the epoxy used. Using the same procedure, GFRP coupons were produced; the only differences included the number of fabric layers and the type of fabric used. PET fabric layers—provided by the manufacturer—were five times thicker than glass fabric. Importantly, composite coupons should include the same dimensions, and all coupons had a cross-sectional thickness of approximately 3 mm. FRP strength is highly influenced by fibre volume fraction, primarily because the fibres provide the composite with strength whereas the matrix binds fibres together and distributes (translates) the load among bonded fibres. Therefore, the fibre volume fraction, V_f , should always be accounted for and reported during the FRP design stage. Fibre volume fraction becomes difficult to accurately obtain when a wet lay-up process is used to create the composite. The epoxy–polymeric matrix will escape from the composite throughout curing, which corresponds to a change in the initially recorded matrix weight. Therefore, the calculated fibre volume fraction will not be exact.

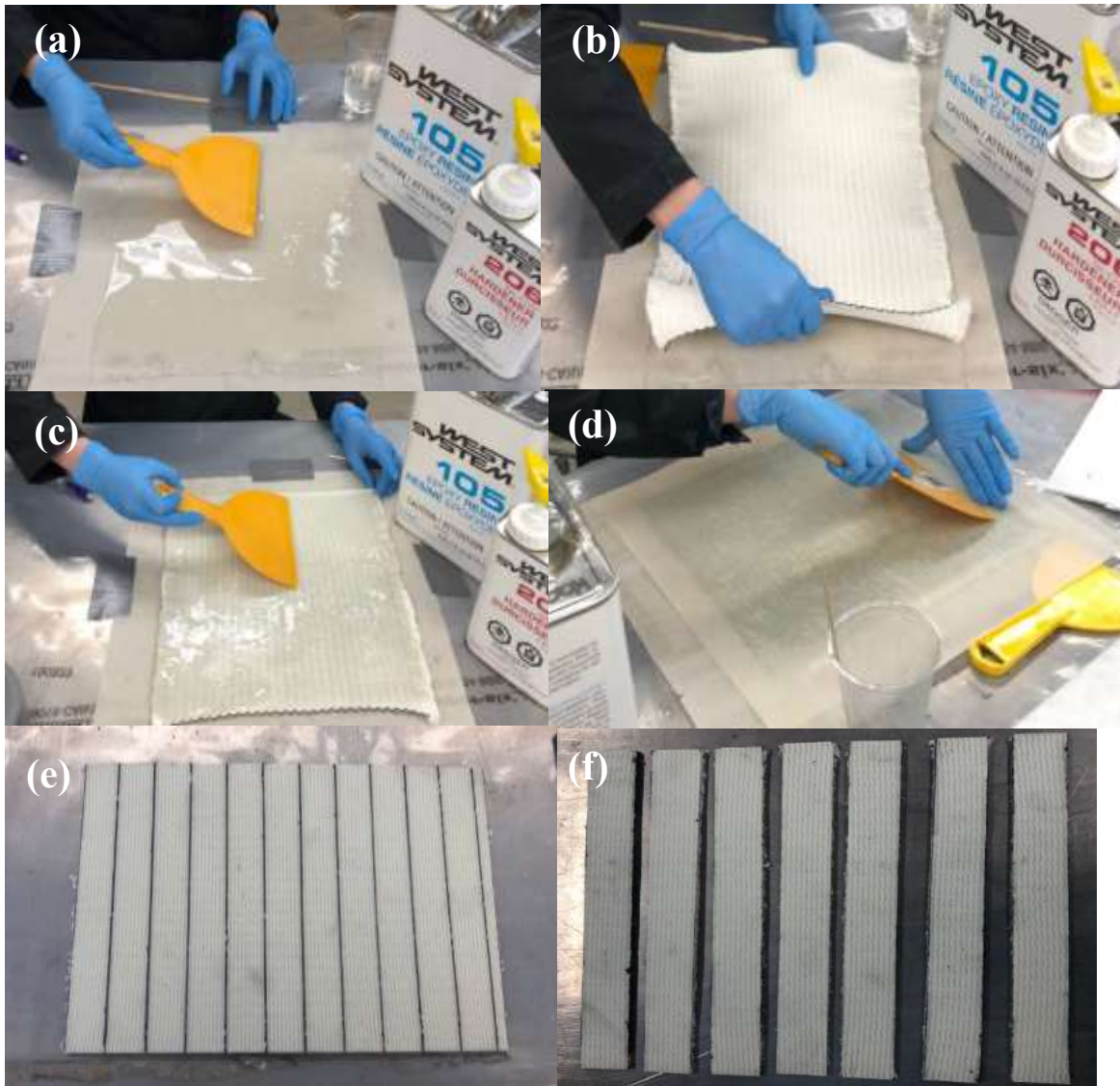


Figure 3-1 Fabrication of PET FRP Coupons: (a) epoxy spread on parchment paper; (b) layer of fabric placed on epoxy layer; (c) second layer of epoxy spread evenly on stitched fibres; (d) parchment paper placed on composite and scraper removed excess air bubbles; (e) after curing, composite was marked and prepared to be cut; (f) composite was cut into coupons.

The fibre volume fraction of the PET FRP and GFRP coupons was calculated based on densities and recorded weights of the epoxy and fabric layer(s) prior to the wet lay-up process. The polymeric matrix used in the fabrication of both types of FRPs was a West

System Epoxy, which has a density of 1.011 mg/mm^3 (Anil, et al., 2018). The density of the PET fibres—obtained from the manufacturer—was equivalent to 1.38 mg/mm^3 ; the density of the glass fabric was 2.5 mg/m^3 (Larco, et al., 2015). Using the densities and weight of fabric and epoxy, the fibre volume fractions of the PET FRP and GFRP composites were found to be 33% and 21%, respectively.

3.3.2 Instrumentation and Coupon Testing Procedure

Each coupon was tested in uni-axial tension using Inston 8501 Material Testing Machine. The ends of the FRP coupons were tightly gripped by the Instron's jaws and carefully aligned to avoid twisting of the coupon during testing which could generate poor data procurement. In accordance with the American Society for Testing and Materials (ASTM) D882, 50 mm of the coupon's length was placed within the grips from each end, leaving 150 mm of the coupon's length laterally unsupported. The loading rate was displacement-controlled which was set to a rate of 2 mm per minute. The change in strain of the GFRP and PET FRP coupons was recorded throughout the test using a video camera and a data acquisition (DAQ) unit which was connected to the strain gauges and extensometer. Figure 3-2(a), reveals a PET composite coupon fixed on the Instron machine before load was applied. The load resisted by the coupon was recorded by the Instron at an interval of 0.1 seconds. The test was finally terminated when the FRP coupon was torn apart along its cross-section. After test completion, stress change and ultimate tensile strength were calculated by dividing the load applied by the average cross-sectional area of individual coupons. The average cross-sectional area was obtained through the average of areas found in three locations within the length of the coupon: two at the end and one midpoint.

To use digital image correlation (DIC) for measuring the strain, FRP coupons were video recorded throughout the test. The camera needed to remain stable and properly aligned; the quality of strain data extracted from the video could be highly affected by external conditions. Therefore, before testing the coupons, several key steps helped produce progressive quality data, including: placing the camera on a properly calibrated tripod; orienting the camera at a 90° angle facing the Instron machine; and manually adjusting the camera's focus and brightness in advance. The camera should commence recording simultaneously with the tension test when the load is applied. The camera should also not be interrupted or touched, as any slight intervention could generate incorrect results often misleading during the research phase. Figure 3-2(b) shows the uniaxial tension testing setup of the prepared FRP coupons.

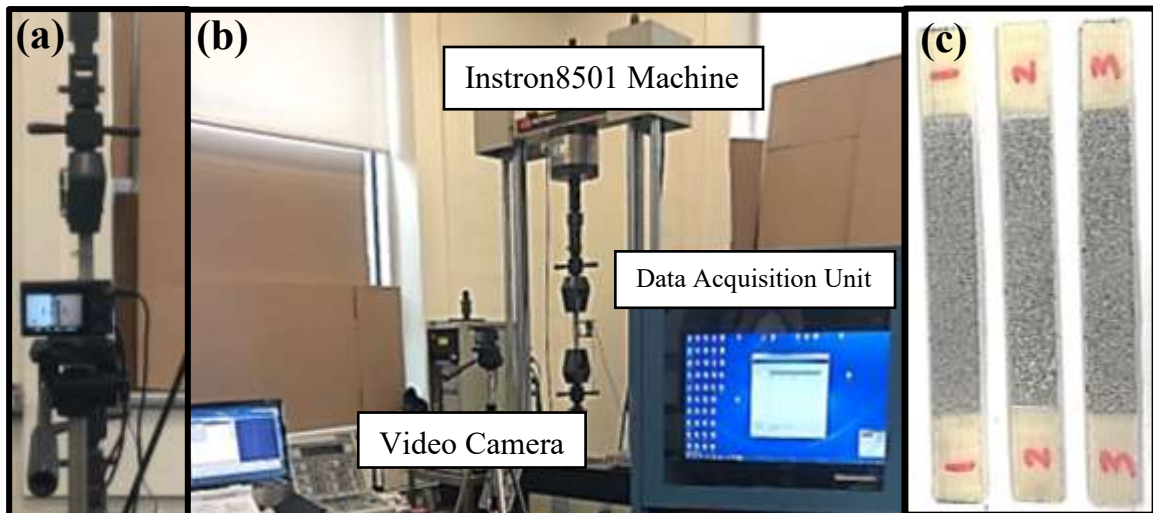


Figure 3-2 Coupon testing setup (a) FRP coupon set on Instron8501 for tension test; (b) coupon testing apparatus; (c) FRP coupons prepared for DIC

Following test completion, the video was converted into a collection of images set at the same time interval as the applied tensile force data. Furthermore, GOM correlate software

was used to extract strain data from captured images. The software identified coupon patterns and monitored individual paint splatters (illustrated in Figure 3-2(c)) as they separated during stretching. Finally, the strain values obtained from the DAQ system and by GOM correlate were carefully aligned with associated stress values to formulate appropriate data for analysis.

3.3.3 Analysis and Results of Coupon Testing

Three FRP coupons were tested from each set of fibre reinforced composite (e.g. GFRP and PET FRP). They concluded relatively similar testing results in terms of strain deformation capacity and strength. Therefore, based on ASTM D882 standards, there was no requirement to test and create more coupons. As shown in Figure 3-3, the ultimate tensile strength for the GFRP and PET FRP coupons were found to be approximately 400MPa and 300 MPa, respectively. As of note, during the tension test, PET FRP coupons deformed greatly; hence, the mounted strain gauges became detached. Furthermore, the strain recording stopped as the strain change reached by the coupons exceeded the highest value measured by the strain gauges. Consequently, the change in strain for those coupons was obtained from the extensometer and DIC. The ultimate strain capacity for the PET FRP and GFRP coupons were found to be approximately 2% and 8%, respectively.

As demonstrated in Figure 3-3, the stress-strain behavior of PET FRP was deemed bilinear, and the juncture between two linear curves is assumed as a yielding point. Thus, the yielding stress and strain were extracted from the plot using the 0.2% offset method.

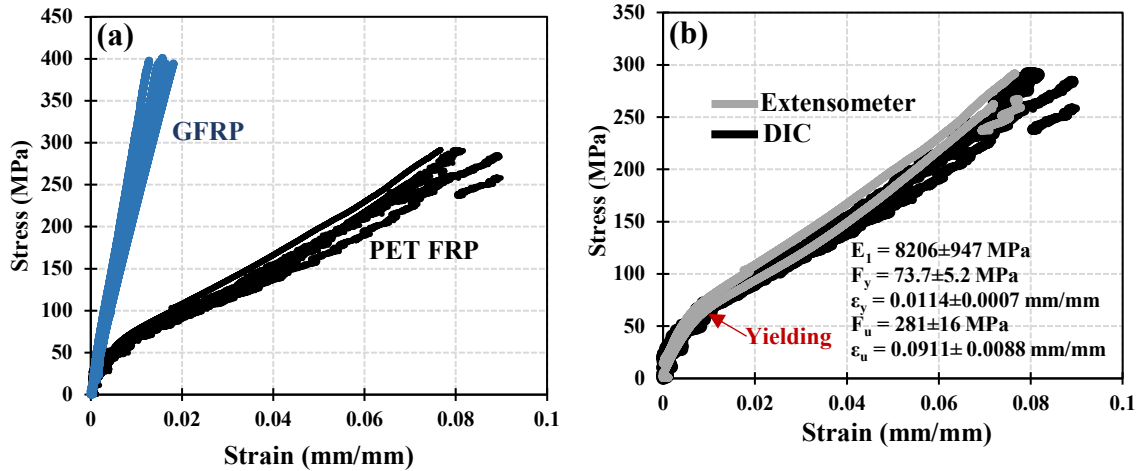


Figure 3-3 Stress-strain diagrams of (a) GFRP with respect to PET FRP and (b) PET FRP

Ultimately, material properties (listed in Table 3-2 and Table 3-3), including the primary and plastic/secondary moduli, illustrated in Figure 3-5 (E_1 and E_p), were obtained. As presented in the Table 3-2, the values of initial modulus, E_1 , measured by DIC, strain gauges, and extensometer are widely spread. This is because DIC cannot accurately measure small strains. As such, the value of initial modulus measured using DIC is not reflective of the actual initial modulus of PET FRP. Thus, the initial modulus is more accurately represented by the values obtained through strain gauges and extensometer. However, past the yielding point, secondary modulus becomes more accurately measured using DIC and extensometer. Figure 3-4 depicts the GFRP and PET FRP coupons after reaching their ultimate tensile stress capacity.

Table 3-2 PET FRP tensile test summary

	DIC	Stain Gauge	Extensometer	Average	Standard Deviation
E_1 (MPa)*	5387	9249	8206	7410	1884
E_1 (MPa)**	5387	8743	8028	7216	1650
E_P (MPa)	2821	Inconclusive	3338	3111	358
E_{sec} (MPa)	3232	Inconclusive	3931	3581	521
f_y (MPa)*	76	66	74	73	5
f_y (MPa)**	76	77	80	78	4
ϵ_y (mm/mm)*	0.0141	0.0089	0.0114	0.0118	0.0023
ϵ_y (mm/mm)**	0.0141	0.0088	0.0133	0.0125	0.0024
f_u (MPa)	281	Inconclusive	Inconclusive	178	13
ϵ_u (mm/mm)	0.0911	Inconclusive	Inconclusive	0.0912	0.0100

* Strain range of 0.001 to 0.003 was used
 ** Strain range of 0.002 to 0.004 was used

Table 3-3 GFRP tensile test summary

	DIC	Stain Gauge	Extensometer	Average	Standard Deviation
E (MPa)	25682	23913	27482	25692	2433
ϵ_u (mm/mm)	0.0152	0.0158	0.0146	0.0152	0.0011
f_u (MPa)	390	390	394	391	5



Figure 3-4 FRP coupons after reaching their ultimate tensile stress capacity; (a) GFRP coupons; (b) PET FRP coupons.

3.3.4 Bilinear Stress-Strain Model of PET FRP

The PET FRP stress-strain relationship was modelled using the equation proposed by Richard and Abbott for bilinear functions. As shown in Figure 3-5, the model splits up the stress strain relationship into three parts. The first and third parts are represented by two linear functions, while the second part is represented by a curve linking the two linear functions together. Hence, the equation includes four parameters: initial modulus, E_1 ; final/plastic modulus, E_p ; shape parameter, n ; and reference plastic stress, f_0 .

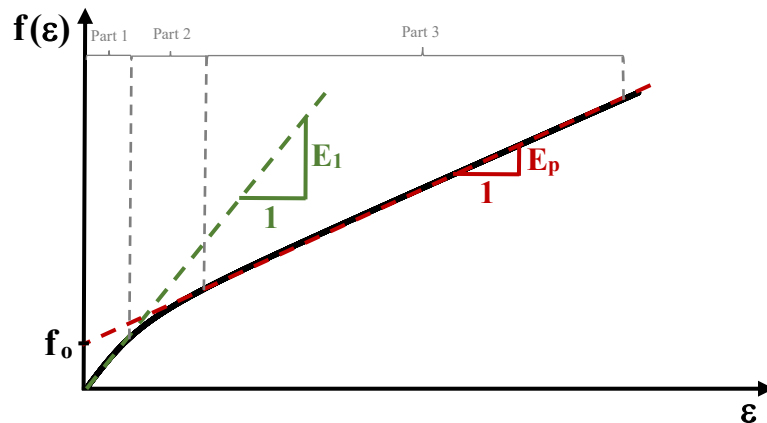


Figure 3-5 Bilinear stress-strain model based on Richard-Abbott equation.

The shape parameter is a constant term controlling the degree of curvature at the transition zone represented in “part 2” of the model. The reference plastic strain term sets out the location of the transition zone. As demonstrated in equation (3-1), the Richard-Abbott stress-strain relationship gives the stress, f , explicitly in terms of strain, ϵ (Richard & Abbott, 1975).

$$f = \frac{(E_1 - E_p) \cdot \epsilon}{\left(1 + \left|\frac{(E_1 - E_p) \cdot \epsilon}{f_0}\right|^n\right)^{1/n}} + E_p \cdot \epsilon \quad (3-1)$$

PET FRP stress-strain curves acquired from the series of uni-axial tension tests—completed on PET FRP coupons—were used to derive terms encompassed in the Richard-Abbott equation. After obtaining the required terms, the function was plotted along the results via experimental testing to verify the finalized model as shown in Figure 3-6. Stress-strain behaviour of PET FRP past the yielding point becomes difficult to monitor. This is because PET FRP has a large strain capacity that surpasses the strain limit that can be measured by the strain gauges and extensometer. Hence, mathematical relations, reported in Figure 3-6, were drawn from the model to relate final modulus to initial modulus and a reference plastic stress to yield stress, f_y . Those relations are destined as a guide when creating the stress-strain model for PET FRP components for structural elements.

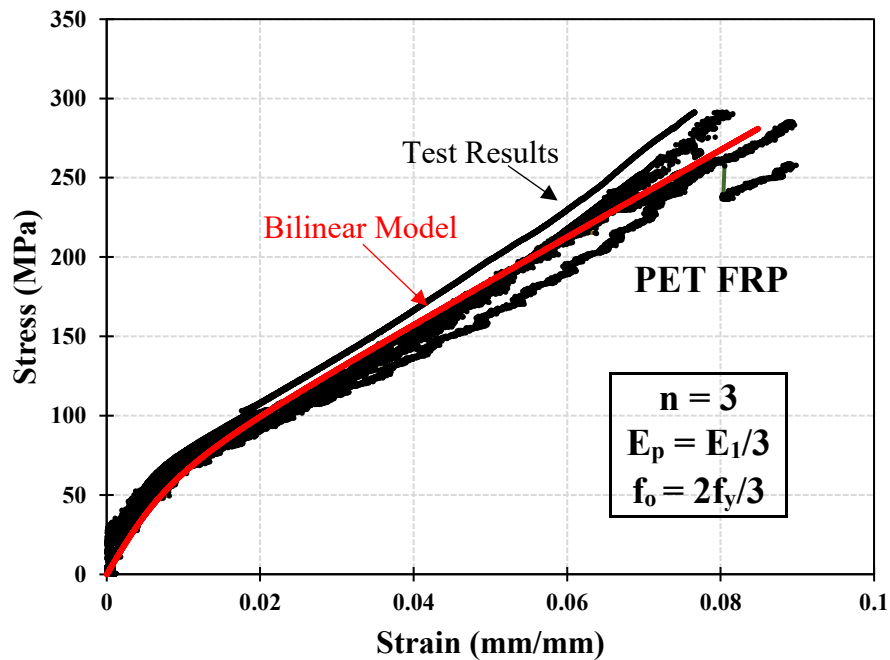


Figure 3-6 Stress-strain curves of PET FRP and parameters used in Richard-Abbott bilinear stress-strain function

3.4 MATERIAL PROPERTIES OF CORE COMPONENT

The PET foam core was manufactured at Armacell[®] where PET pellets—derived from post-consumed plastic bottles—were extruded into sheets and bonded into 4x4 foot boards with a 3-inch thickness. The foam's density is dependant on the air content detailed in the production stage. The foam's mechanical properties were directly obtained from the data sheet provided by the manufacturer. The technical data sheet was used to develop a relationship between foam density and various strength parameters (illustrated in Figure 3-7). The plot, shown in Figure 3-7, was used to derive the constants that formed the analytical model. The mechanical properties of the PP honeycomb core—at a density of 80kg/m³—was acquired from the technical data sheet. Based on the data, an analytical model was created to anticipate the change in strength parameters of the honeycomb structure as core density changes. It should be noted that the nominal properties of materials can be significantly different from properties obtained through experimental testing. Since the density of the PP core was the only changing variable and due to limited availability of PP core with varying densities, the use of FEA modeling is justified. Appendix A describes the procedure by which the analytical model was created in a finite element analysis (FEA) software.

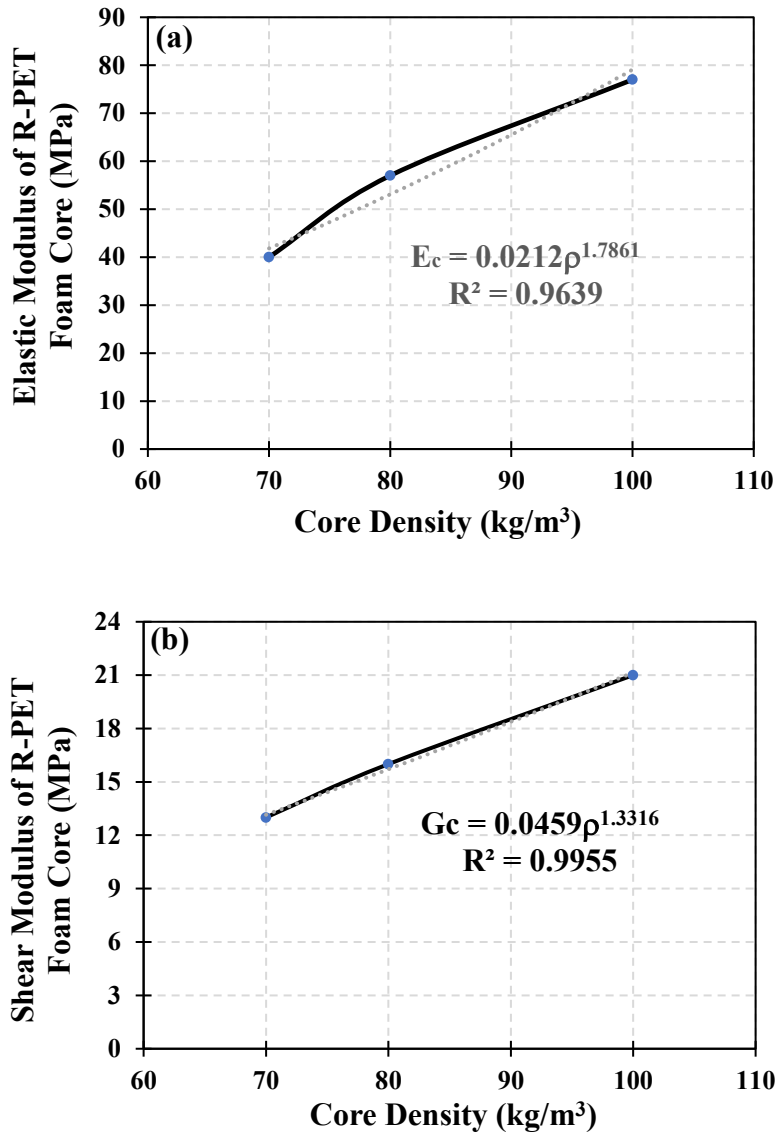


Figure 3-7 Change in mechanical properties with respect to core density: (a) elastic modulus vs foam density; (b) shear modulus vs foam density.

Figure 3-8 (a) illustrates the loading configuration and boundary conditions applied to the model to calculate the shear modulus, G_c . Consequently, the model was loaded as shown in Figure 3-8 (b) to obtain the elastic modulus, E_c . Shear and elastic moduli—with respect to density—were plotted to derive constants shown in Figure 3-9 (a) and (b).

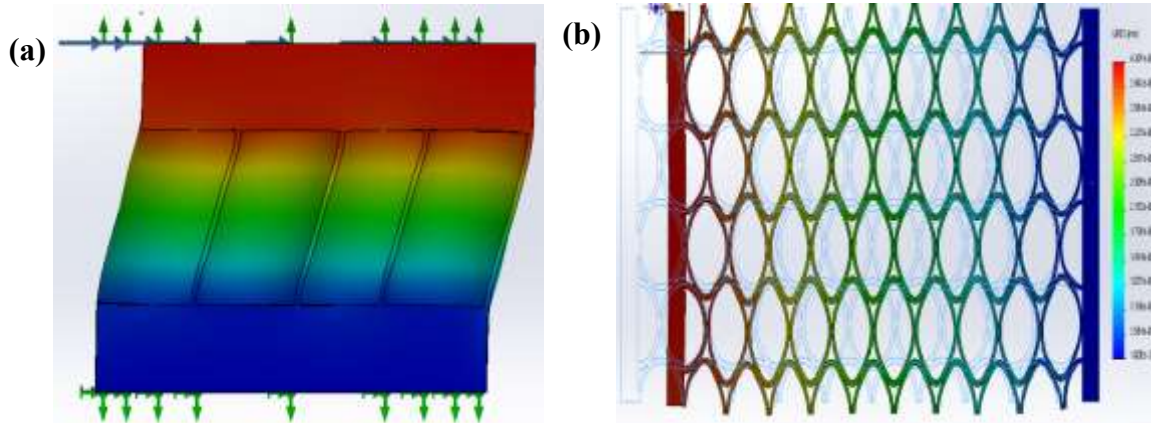


Figure 3-8 Loading configuration applied on developed analytical model to derive the (a) shear modulus and; (b) elastic modulus.

Change in shear strength with respect to R-PET foam density was derived from the values listed in the technical data sheet that was provided by the manufacturer. This correlation is presented in Figure 3-10. Shear strength of the PP honeycomb core did not depend on the core density. Instead, it was a constant value obtained from the technical data sheet provided by the manufacturer. Appendix C illustrates a shear test done on the PP honeycomb core to obtain the shear strength value experimentally. The testing set-up involved in the shear test was proven to be invalid. Hence, the obtained shear strength value was inaccurate and was not used in the analytical model.

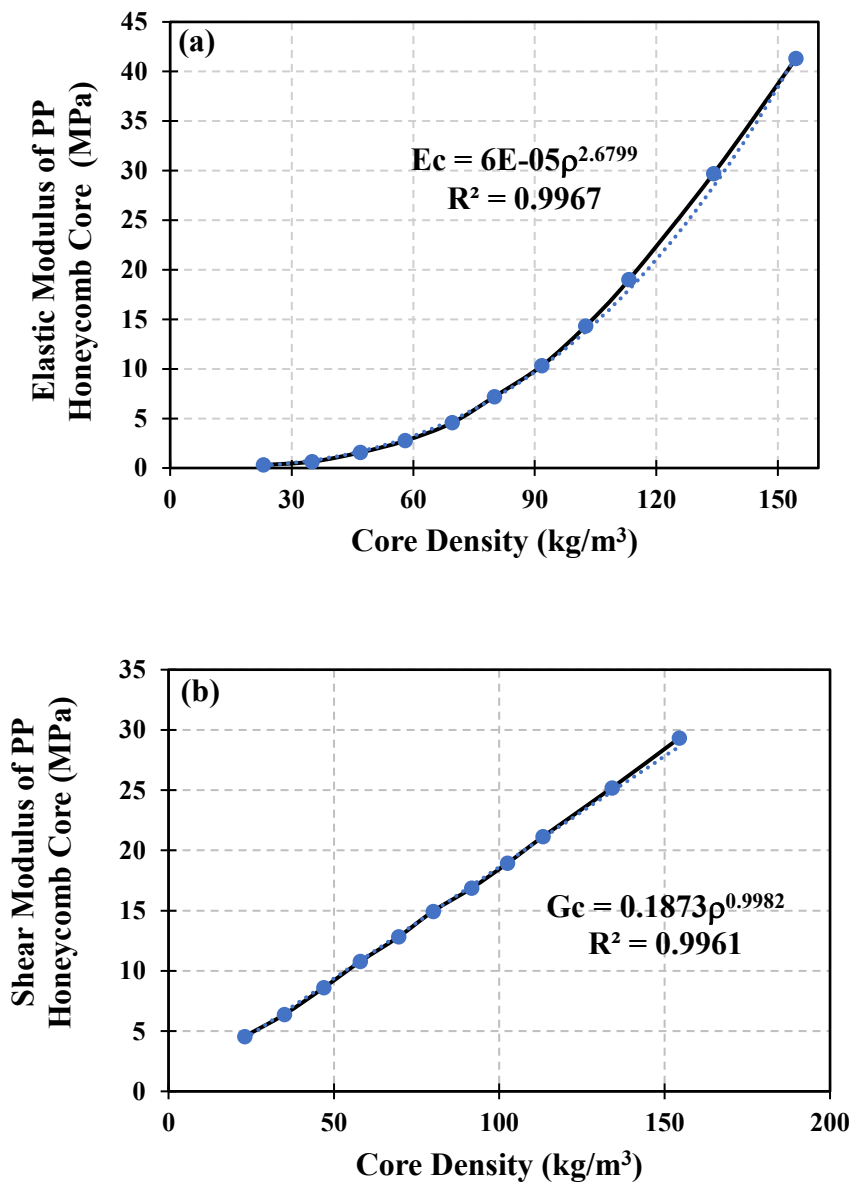


Figure 3-9 Change in mechanical properties with respect to core density (a) shear modulus vs PP honeycomb density; (b) elastic modulus vs PP honeycomb density.

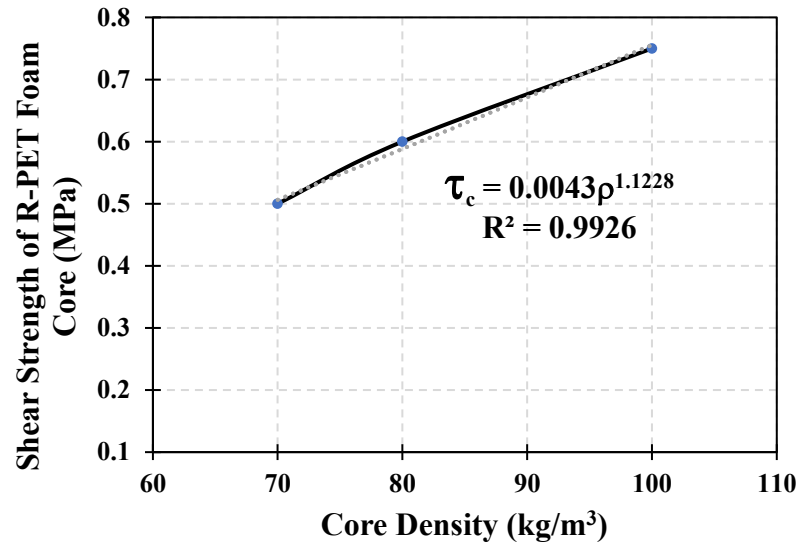


Figure 3-10 Change in shear strength of R-PET foam core with respect to core density.

3.5 FABRICATION OF SANDWICH PANELS

The fabrication procedure, shown in Figure 3-11, was followed to produce all different sets of sandwich panels. Plastic sheet and parchment paper were taped on a clean tabletop; it is vital to use wrinkle-free plastic to ensure a smooth tabletop and a final product with flat facings and no impressions. A unidirectional fabric layer was then cut to required length and its borders traced on parchment paper. Epoxy and hardener were combined at a ratio of 5:1 and carefully mixed for two minutes. Within the traced borderlines, the above mixture was evenly spread on the parchment. The unidirectional fabric was placed atop, and an additional layer was added onto the fabric. The repeating layers of fabric and epoxy depend on the thickness of the dry fabric, as well as the required face thickness outlined by the design.

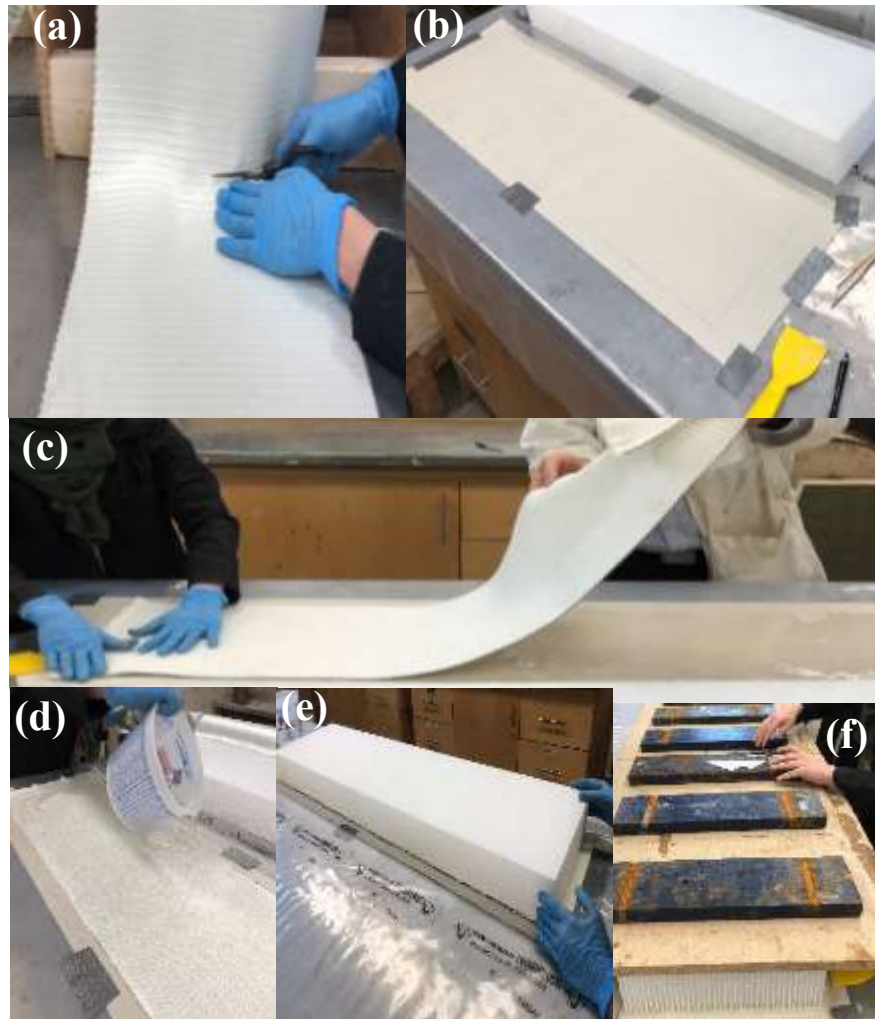


Figure 3-11 Fabrication process of sandwich panels: (a) fabric layer cut to the required length; (b) parchment paper traced based on fabric layer; (c) unidirectional fabric was placed on layer of resin; (d) another layer of resin spread on fabric layer; (e) core component placed on top of epoxy layer; (f) weights placed on composite prior to curing stage.

Furthermore, epoxy and hardener must be used in adequate amounts to ensure a load transfer matrix exists between the fabric's fibres and the facing and core components. The core component was placed on top of the second layer of epoxy and hardener then weights were placed atop the core to allow excess resin to outflow from the sides. The

composite was then left to cure at room temperature for four days. After curing, the same procedure was done to create the other facing component of the sandwich panel. Each facing component was fabricated and cured separately; it is not recommended to fabricate the two facings within the same day and set them to cure simultaneously. This is because the wet resin can be absorbed by the core. Finally, the sandwich panel was cut into four equal sections at a width, b , of 76 mm.

3.6 INSTRUMENTATION AND BENDING TEST SET-UP

The sandwich panels were tested in three-point bending using the test setup illustrated in Figures 3-12 and 3-13. For each sandwich panel, two strain gauges were mounted on the centre point of compression and tension faces to capture the strain change during bending. The panels were supported on steel rollers from each end.

A string potentiometer was attached at the mid-span of the unsupported length to capture the panel's displacement during bending. Concentric load was applied through a hollow structural section (HSS) at a constant displacement-controlled rate of 6 mm per minute. The HSS was 350 mm wide and weighs 0.8 kg, which was accounted for during data analysis. The data acquisition unit (DAQ) recorded the force applied, bending deformation, and change in panel strain during bending at midspan length. The test was terminated once the sandwich specimens reached their ultimate strength capacity. At the peak load, sandwich panels deform abruptly, causing difficulty to identify the failure mechanism. Therefore, a video camera was part of the test setup and focused on the failure point to track the sequence by which the sandwich failed.

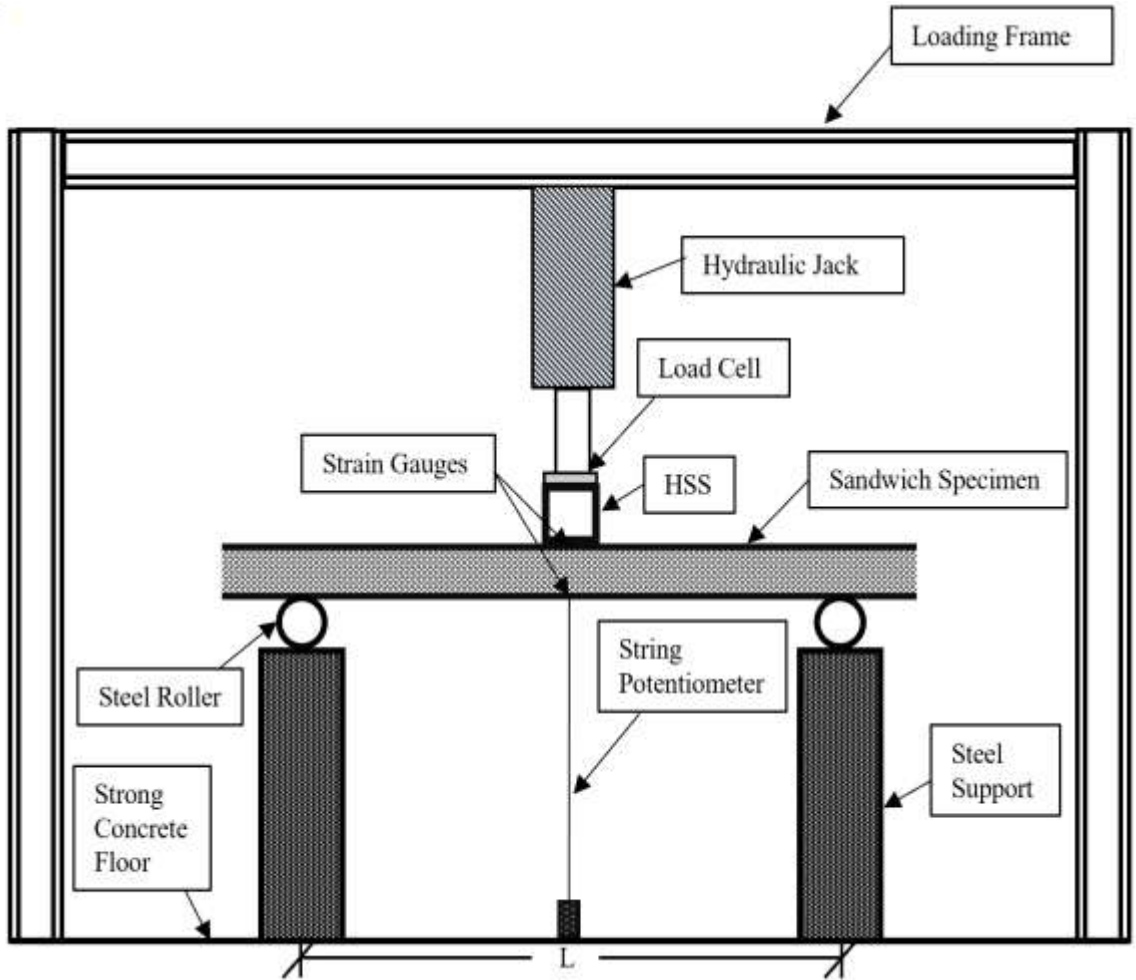


Figure 3-12 Sketch for three-point bending test set-up

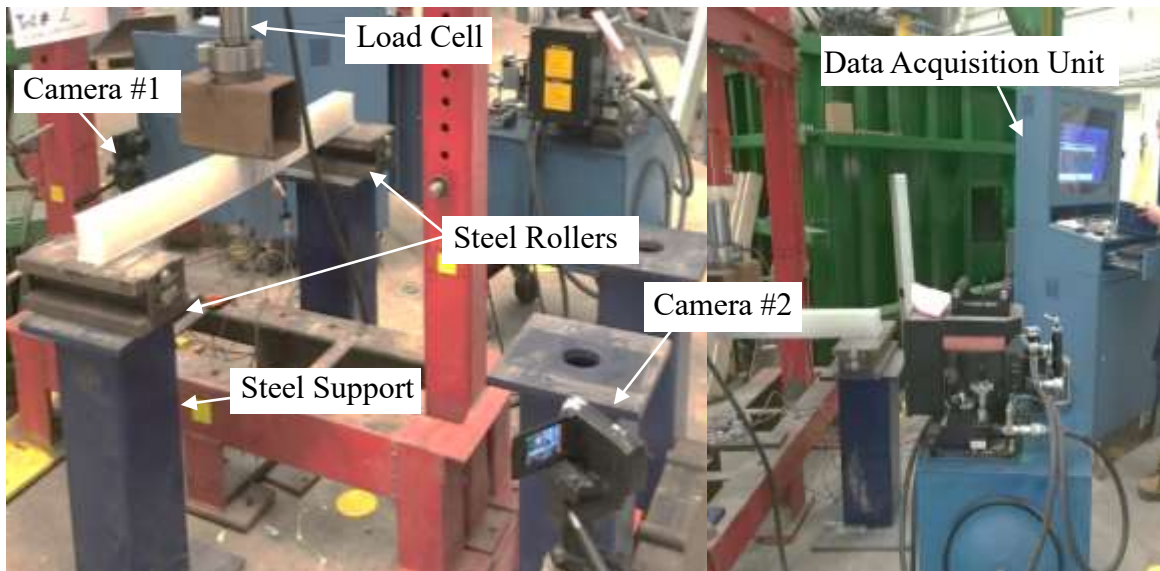


Figure 3-13 Three-point bending test set-up

3.7 DATA ANALYSIS AND TEST RESULTS

As shown in Figure 3-13, the three-point bending test set-up includes many variables. All variables must function well throughout the entire testing period for the experiment to be considered successful. Hence, if one of the machines, devices, or tools ceases to function or was improperly set, the entire test is considered unsuccessful and its yielded data are rejected. Based on this established criterion, three of each set of sandwich panels were considered successful. Hence, data analysed in this section are derived from 18 tests. After completion of the three-point bending test, the facing components of all tested sandwich panels returned to the original shape. The bending load did not exceed the tensile/compression strength of the facing material, which allowed it to undergo full elastic recovery. Table 3-4 presents a summary of the panels' mechanical properties tested in bending at ultimate limit state.

Table 3-4 Sandwich panel specimens' mechanical properties at ultimate limit state.

Specimen	Load (kN)	Deflection (mm)	Tensile Strain ($\mu\epsilon$)	Compression Strain ($\mu\epsilon$)	Moment (kNm)	Curvature (1/m)
1.PET FRP-PP80	4.2	38	9561	-12398	1.2	0.28
2.PET FRP-PP80	4.3	36	8223	-9196	1.2	0.20
3.PET FRP-PP80	4.5	32	9557	-14657	1.2	0.33
1.GFRP-PP80	5.5	33	3878	-4127	1.5	0.09
2.GFRP-PP80	6.1	41	3458	-5529	1.4	0.10
3.GFRP-PP80	5.2	27	3532	-4184	1.4	0.09
1.PET FRP-RPET70	3.7	41	9574	-9042	1.0	0.22
2.PET FRP-RPET70	3.5	37	8253	-12809	1.0	0.28
3.PET FRP-RPET70	3.4	36	8144	-13303	1.0	0.28
1.PET FRP-RPET80	4.0	37	8845	-13345	1.1	0.27
2.PET FRP-RPET80	4.7	42	9997	-14495	1.3	0.31
3.PET FRP-RPET80	4.2	42	10419	-14373	1.2	0.30
1.PETFRP-RPET100	4.3	41	1083	-16606	1.2	0.33
2.PET FRP-RPET100	4.2	42	13345	-21967	1.2	0.42
3.PET FRP-RPET100	4.3	41	9776.5	-12156	1.2	0.27
1.GFRP-RPET100	7.3	43	5758	<i>Inconclusive</i>	2.0	<i>Inconclusive</i>
2.GFRP-RPET100	7.5	45	5803	-6881	2.1	0.15
3.GFRP-RPET100	7.2	39	3966	-7459	2.0	0.14

3.7.1 Load-Deflection

Deflection of a beam under an applied load is a vital factor to consider, particularly for a beam used in structural engineering applications. For structural elements, deflection capacity has the potential as the governing aspect of the design. Thus, a strong beam with low stiffness will meet the ultimate limit state requirement but not the serviceability limit state criterion. Change in deflection, with respect to the applied load, was captured at the sandwich beam's mid-span length throughout the three-point bending test. Figure 3-14

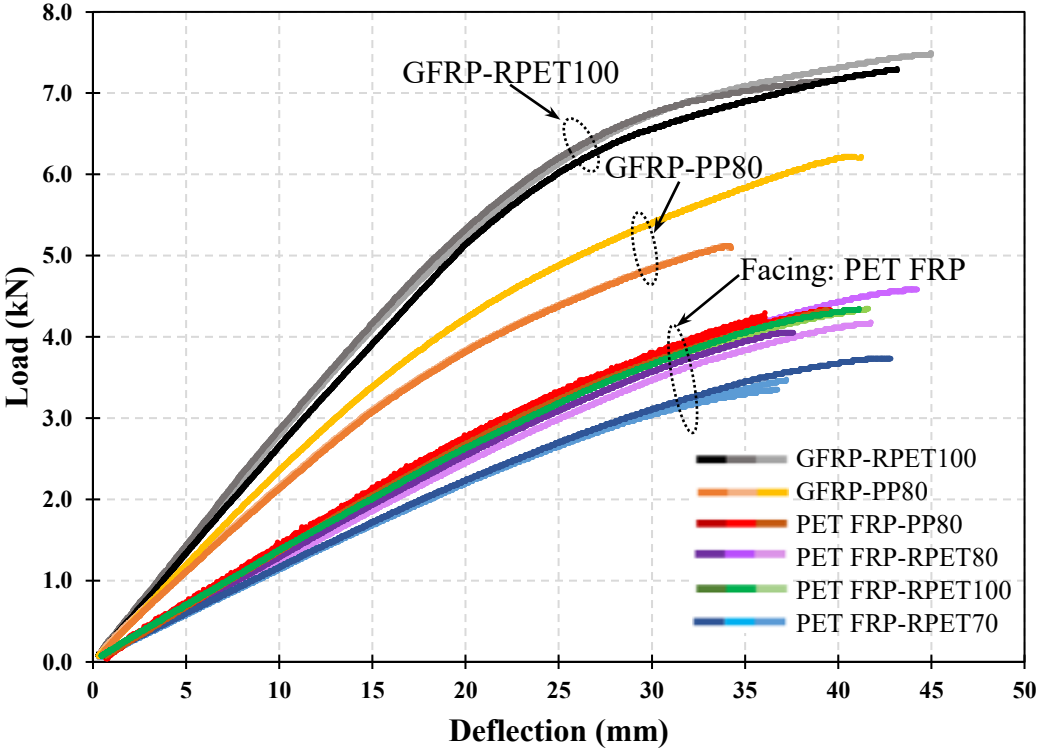


Figure 3-14 Load vs deflection curve of sandwich panels under three-point bending

As shown, the overall stiffness of the sandwich panel depends on the stiffness of the facing component. Hence, sandwich panels comprised from GFRP facings deflected less than sandwich panels made from PET FRP faces at a certain load.

Load-deflection curves of sandwich panels made from GFRP facing and PP core had lower stiffness in comparison to panels made from GFRP facing and R-PET core. This illustrates that the core component of a sandwich panel contributes to the overall stiffness of the beam. Additionally, the ultimate load capacities of sandwich panel specimens made from GFRP facing and PP honeycomb cores varied considerably. This suggests that the sandwich panels made from PP core and GFRP facings prematurely failed. Premature failure can be triggered by multiple factors typically related to the fabrication process. This particular failure was caused by the weak bonds connecting cylinders that create the honeycomb structure. As shown in Figure 3-14 (a), due to this weak bond, shear failure occurred along the walls of the cylinders/tubes. In contrast, the sandwich panel set made from GFRP facing and R-PET foam sheared following the diagonal crack shown in Figure 3-13 (b).

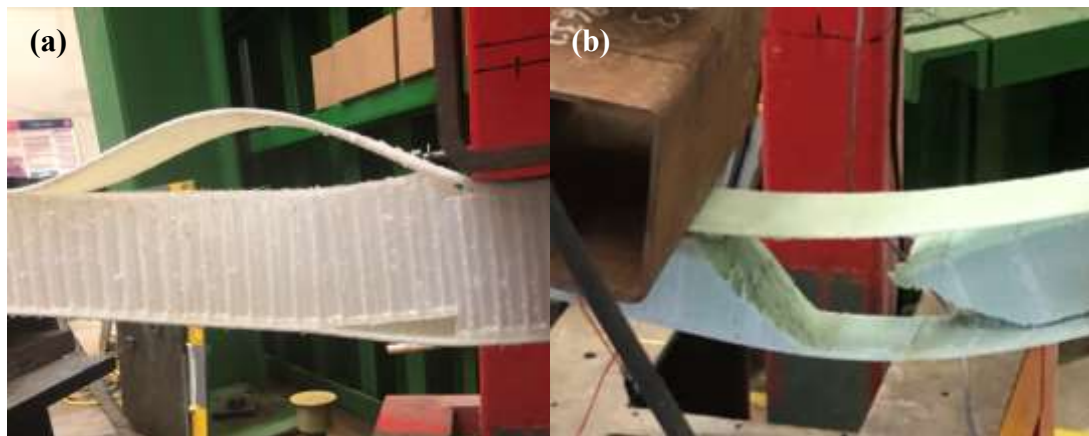


Figure 3-15 Side view of sandwich panels made from (a) PP honeycomb core and (b) R-PET foam core after failure.

The load-deflection curve presented in Figure 3-14 suggests that no sandwich panel sets made from PET FRP facings prematurely failed. Thus, changing the core type from PP honeycomb to R-PET foam does not change the ultimate strength capacity of the sandwich panels. Changing the density of the foam core results in a change in stiffness. As the density of the foam core increases, the corresponding stiffness increases. This correlation plateaued at a core density of 80 kg/m³, where increasing the density of the foam core from 80 kg/m³ to 100 kg/m³ did not generate an increase in stiffness. In addition to the change in stiffness, as the foam core density increased, the overall weight of the sandwich panel will increase. Sandwich panels used in construction are required to have high strength-to-weight ratio. Considering this aspect, the ideal foam core density for the sandwich beams should be 80 kg/m³—according to the load-deflection curves of the tested beams.

3.7.2 Bending Strain

Deflection of a beam under three-point bending is only achieved with a strain capacity on the top and bottom facings of the sandwich panel. Hence, large bending deflection corresponds to a sandwich panel made from facings with large strain capacities. When a load is applied downwards on a sandwich panel under a three-point bending condition, the top face undergoes compression while the bottom undergoes tension. As the load increases, the strain increases subsequently. This correlation can be anticipated using the load-strain diagram shown in Figure 3-16. As shown in the Figure, panels made from stiff GFRP facings had significantly less strain capacity compared to panels with PET FRP facings; the core component did not impact the overall deformation and bending strain for both facings. Hence, the strain vs load curves did not change significantly among the

sandwich panel sets made with varying core materials. Additionally, Figure 3-16 illustrates that PET FRP's strain capacity varies depending on the direction of the force applied (i.e., tension and compression). The ultimate strain capacity reached by the top facing—the facing under compression—was approximately $15,000\mu\epsilon$. Meanwhile the ultimate strain capacity reached by the bottom facing—the facing under tension—was approximately $10,000\mu\epsilon$.

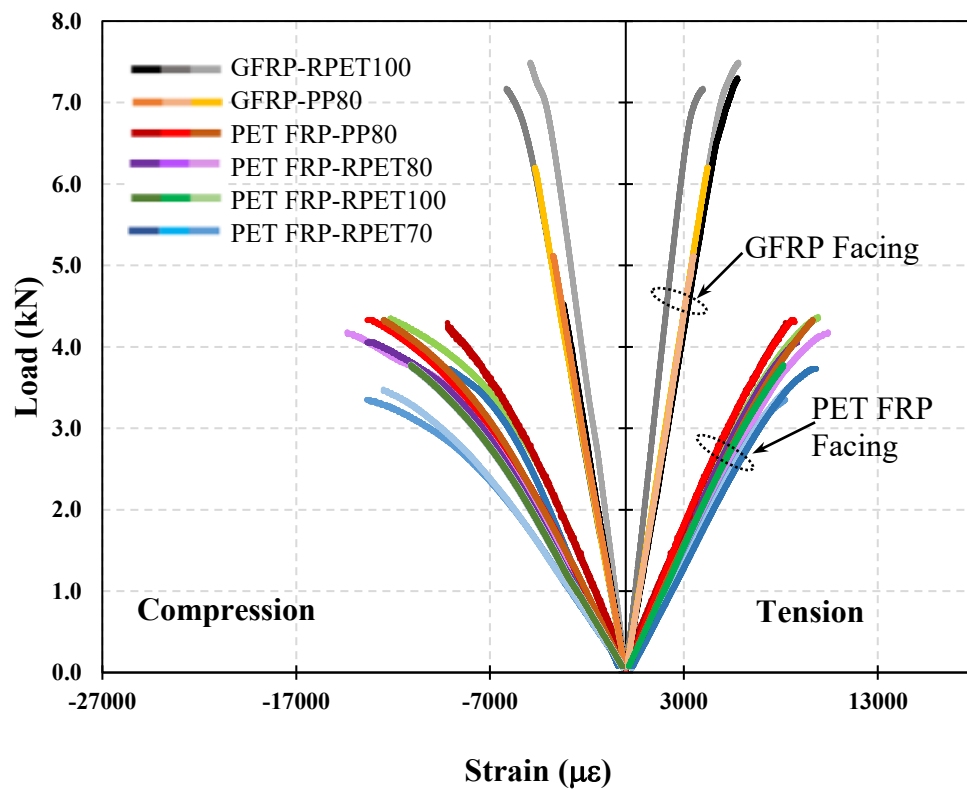


Figure 3-16 Compression and tension strains with respect to the applied load of the tested sandwich panels.

3.7.2 Moment-Curvature

As the bending moment varies with respect to amount of applied load, curvature or the degree to which the beam is bending, will change. Moment-curvature relationship is often used to obtain or verify the flexural rigidity constant associated with the bending beam

experimentally. Flexural rigidity is the moment required to bend the beam one unit of curvature. Figure 3-17 presents the moment-curvature relationship of all the simply supported sandwich beams tested in three-point bending. As shown in the Figure, flexural rigidity depends on the facing components. Hence the sandwich panel sets with matching facing material develop a similar moment-curvature relationship.

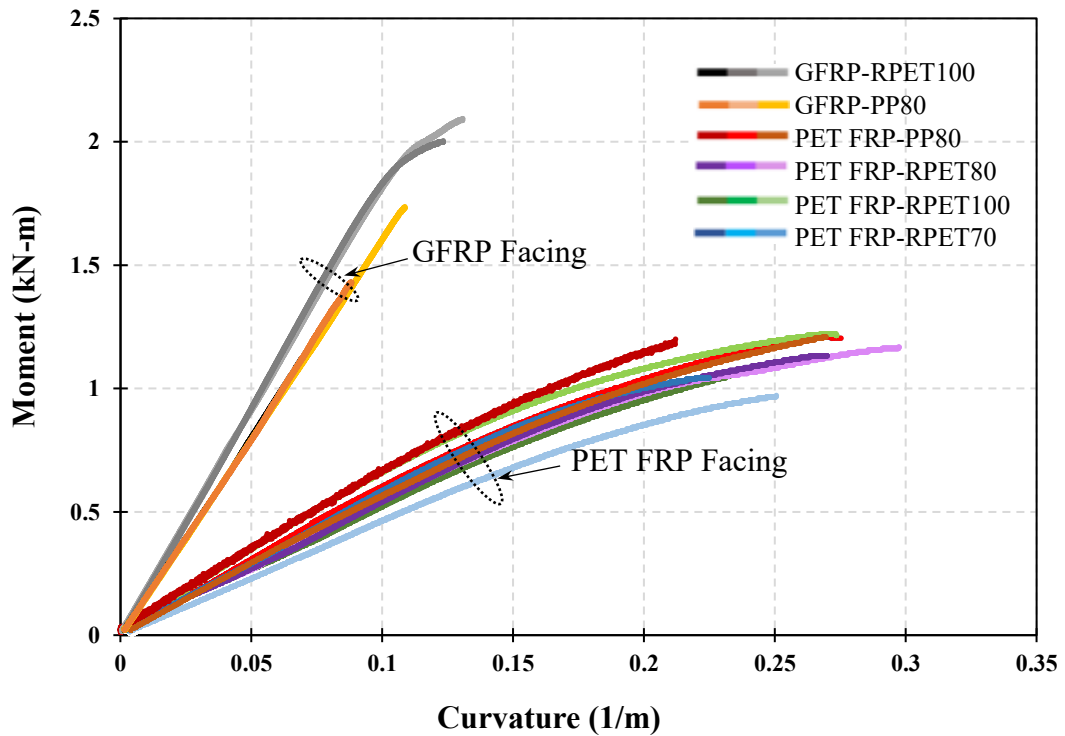


Figure 3-17 Moment vs curvature diagram associated to all the different sets of sandwich panels.

3.7.3 Failure Mode

The mechanism of failure of sandwich panels is generally difficult to assess experimentally. Unlike numerical models conducted on finite element analysis software, experimental modelling does not instantly stop once a mode of failure is detected, instead the experiment is terminated shortly after this critical stage. This leaves room for error in

identifying the correct mode of failure of the tested beam. The potential human caused error can only be avoided when there is a significant gap in the mechanical strengths of the various components making up sandwich panel. Since the calculated failure loads triggering core shear failure, wrinkling and face rupturing of all the tested sandwich panels were close, it became difficult to report the mode of failure accurately. As all of these modes can happen at a very short time interval– just when the test is being terminated. Figure 3-18 shows the side-view of the sandwich beams after failing.

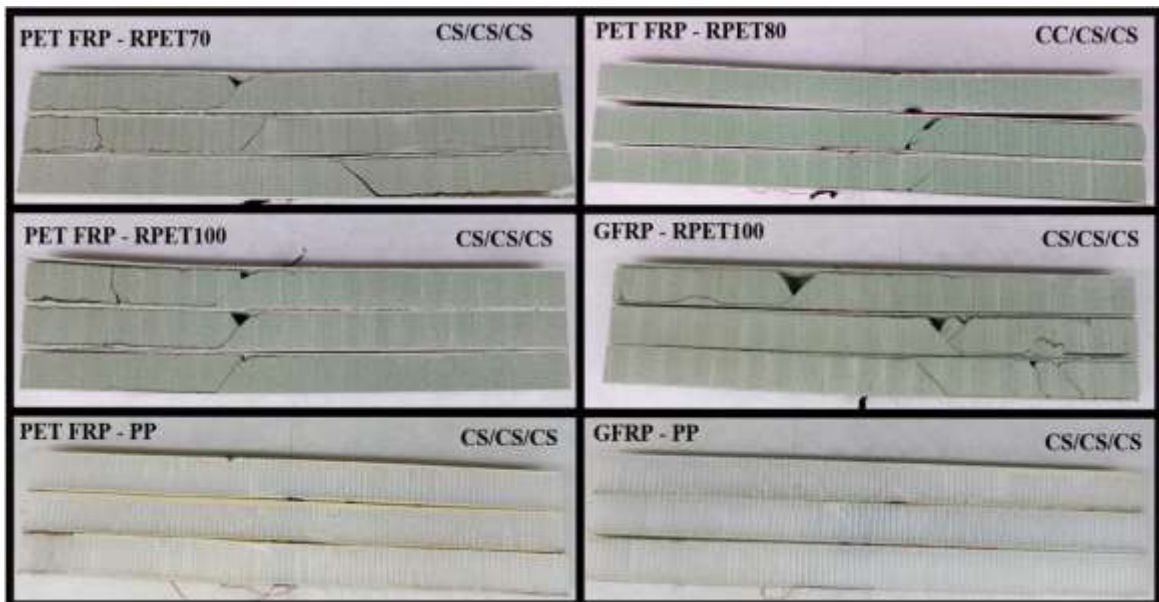


Figure 3-18 Side-view images of tested beams.

The beams' pictures in the figure suggest that all of them failed in core shear except one made from PET FRP facing and RPET70 foam core which seemed like it failed by the crushing of compression face. This conclusion is not necessarily true. Figure 3-19 shows a series of pictures that were extracted from a slow-motion video of one of the tested beams. Figure 3-19 (a) suggests that wrinkling was the primary mode of failure, instantly after wrinkling, the core component failed as shown in Figure 3-19(c).

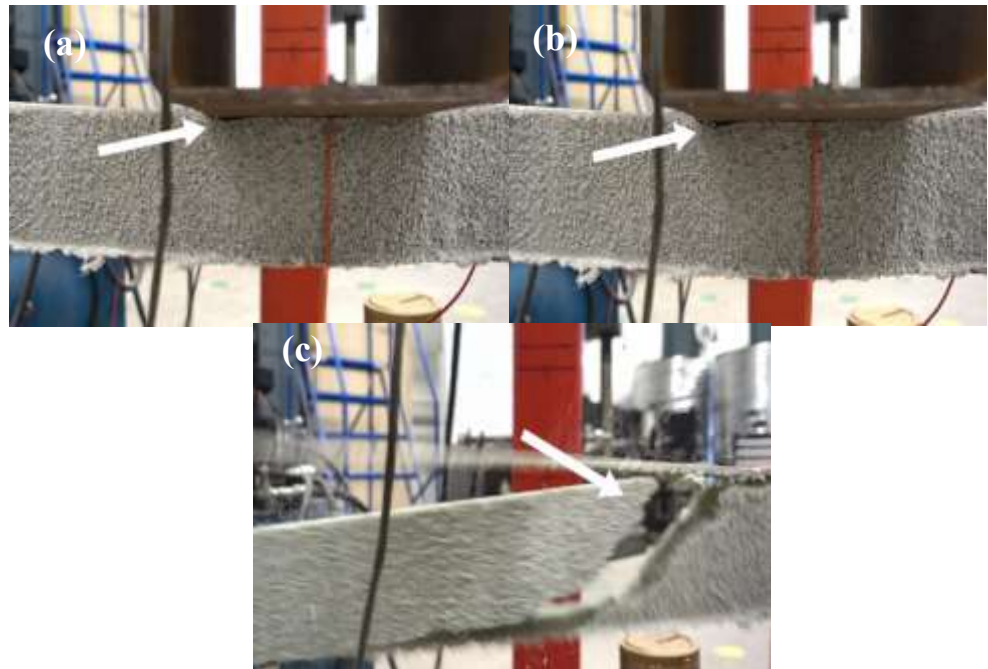


Figure 3-19 Side-view of the beam showing the sequence at which it failed. (a) Wrinkling of the top face appears and (b) starts propagating. (c) Core fails in shear.

CHAPTER 4 ANALYTICAL MODEL

4.1 SYNOPSIS

Numerical models were developed using the mechanical properties associated with each type of material—those which were involved in creating components for various sets of sandwich panels. Numerically modeling sandwich panels provides a stronger understanding of load-bearing behaviour and justifies the testing results obtained experimentally. Two types of models were developed. Firstly, one that predicts the load vs deflection relationship of the different sets of sandwich panels. Secondly, the model anticipates failure mode of any sandwich panel made from PET FRP/GFRP facings and PP/R-PET core, which is based on the design panel dimension and core density. This section will analyse the established models, and explain the method and assumptions used in development.

4.2 MODELLING LOAD-DEFLECTION BEHAVIOR

As mentioned, the total deflection of a beam under three-point bending is a sum of shear and bending deflections; Chapter 2 provides a detailed analysis used to generate the total deflection equation. Shear and secant moduli of the facing and core components of the sandwich panels—acquired by direct lab testing and analytical modeling, as shown in section 3.4—were inputted into equations as constant values to obtain a linear load-deflection model. Conversely, a non-linear model was developed using the secant elastic and shear moduli that varied according to the amount of applied load.

4.2.1 Linear Model

The linear model assumes that the PET FRP facing's elastic modulus is a constant term. This assumption was invalidated through a tension test conducted on the PET FRP coupons—depicted in the previous chapter. As illustrated in Figure 3.3, the stress-strain curve of the tested PET FRP coupons was bilinear, and the elastic modulus varied depending on the force applied in tension. Additionally, the shear modulus term, used in the shear deflection term of the model, was also assumed to be non-changing throughout the bending test. This assumption was invalidated after testing sandwich panel sets made from GFRP facings in three-point bending. The load-deflection curve of those sets (presented in Figure 3-12) was found to be non-linear.

4.2.2 Non-Linear Model

The non-linear model was developed using different assumptions from those made while formulating the linear model. Hence, the shear modulus of the core component and the elastic modulus of the facing components were not inputted as constant values in the total deflection equation. Instead, secant elastic modulus was used to formulate the non-linear load vs deflection model due to bending and the secant shear modulus of the core component was used in developing the non-linear load-deflection behavior due to shear.

4.2.2.1 Deflection Due to Bending

The non-linear load vs bending deflection model was obtained by converting the concentric applied load into stress resisted by the facings of the panels, and plugging the stress value into the Richard-Abbott equation (Equation 3-1) to obtain strain values for each stress. Since the Richard-Abbott equation yields stress in terms of strain, a VBA program was developed in Excel to calculate the strain values corresponding to the

stresses. Appendix B includes a detailed explanation of the necessary code. After generating the stress vs strain behavior of the facing component using the Richard-Abbott equation—which is detailed in section 3.3.4—the secant elastic modulus, E_{Sec} , was obtained. This is depicted in Figure 4-1, and consequently plugged into the bending deflection equation. The flowchart illustrated in Figure 4-2 demonstrates the method for modeling the bending deflection of sandwich panels in simple steps.

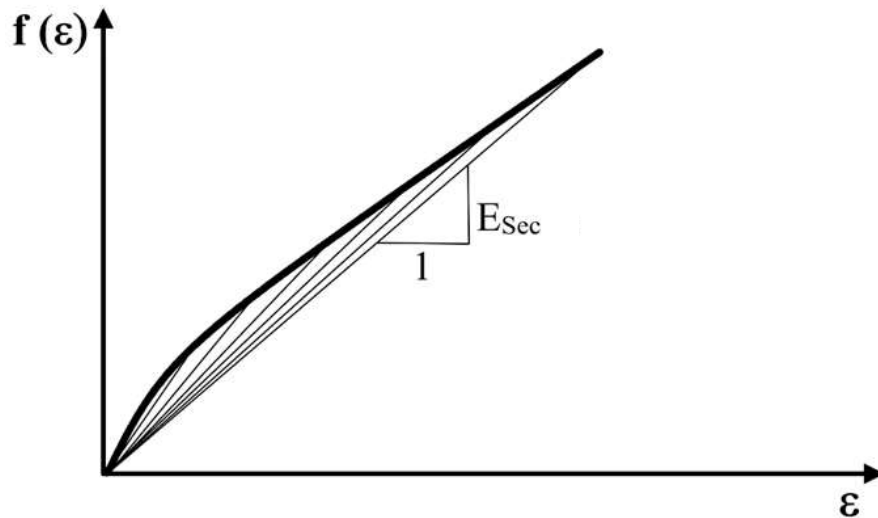


Figure 4-1 Stress vs strain diagrams of facing component with secant lines plotted on the curve to obtain the “varying” secant modulus.

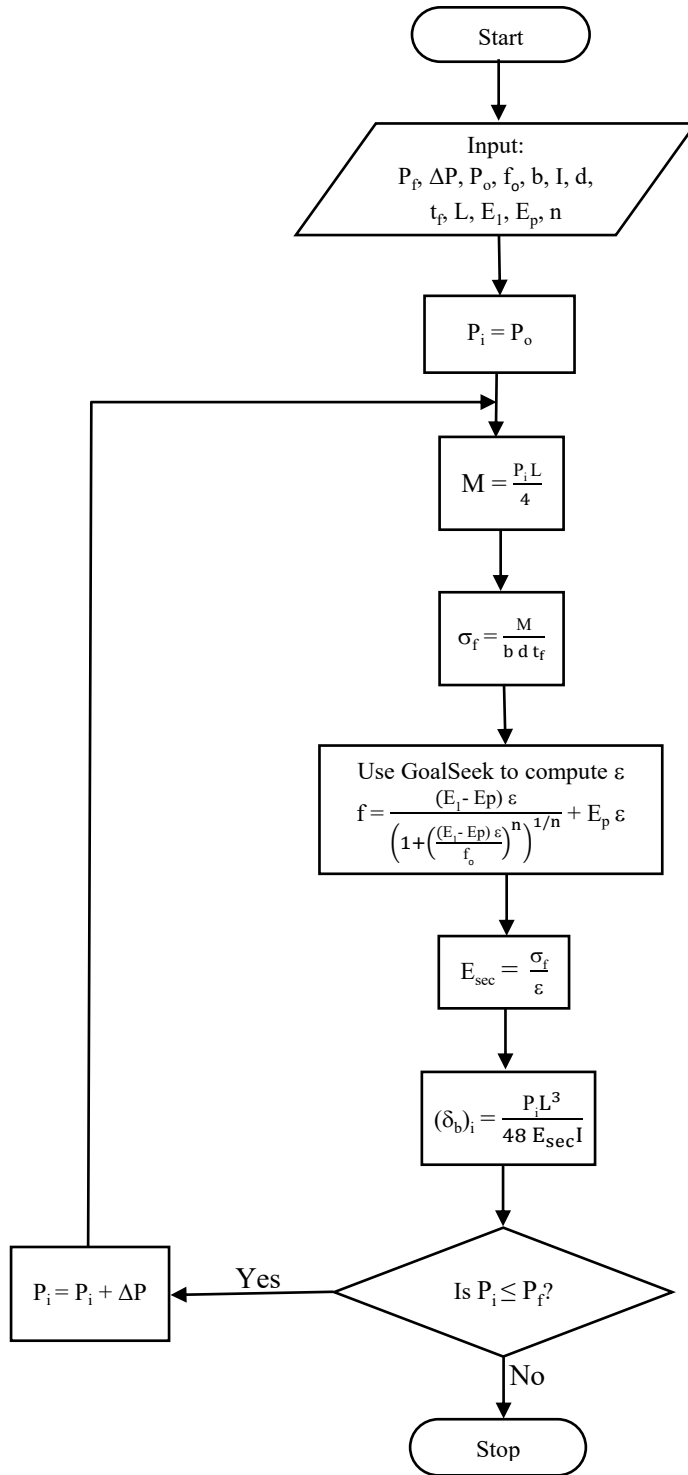


Figure 4-2 Flowchart of bending deflection model.

4.2.2.2 Deflection Due to Shear

Multiple assumptions helped generate the non-linear load vs shear deflection model. As shown in Equation 4-7, the model assumes that the ultimate shear strain, γ_u , of the core component is twice the maximum shear strain achieved by the core within its elastic limit, γ_e . This fundamental assumption is demonstrated in Figure 4-3. The maximum shear strength, and shear modulus within the elastic range, G_e , were obtained from the material data sheet provided by the manufacturer.

$$\gamma_u = 2 \cdot \gamma_e = 2 \cdot \frac{\tau_u}{G_e} \quad (4-7)$$

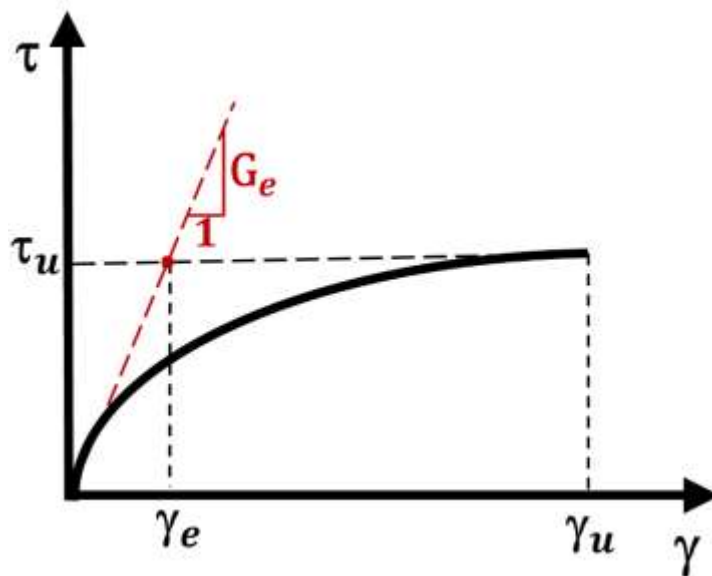


Figure 4-3 Non-linear shear stress vs shear strain projected relationship.

The non-linear shear stress vs shear strain behavior of the core component was modeled using the equation of a parabola shown below:

$$y = ax^2 + bx + c \quad (4-8)$$

Thus, “y” is the shear stress at a given shear strain “x.” Because the shear stress and shear strain relationship begin at zero, the “c” term is omitted from the equation, which is then simplified to:

$$\tau = ay^2 + by \quad (4-9)$$

Using the property of first derivative—which demonstrates that the tangent line slope is equivalent to the derivative at the point of tangency—“a” and “b” constants are obtained as follows:

$$\tau' = \frac{\partial \tau}{\partial \gamma} = 2a\gamma + b \quad (4-10)$$

Applying the initial value of shear strain ($\gamma = 0$) into the above equation, “b” simplifies to:

$$b = \frac{\partial \tau}{\partial \gamma} = G_e \quad (4-11)$$

Applying the final values of strain within the elastic limit ($\gamma = \gamma_e$) and stress ($\tau = \tau_u$) into the parabola equation, “a” term becomes equivalent to:

$$a = \frac{\tau_u - G_e \gamma_e}{\gamma_e^2} \quad (4-12)$$

Inputting the equivalent values of “a” and “b” terms into the parabola equation, the shear stress equation becomes equivalent to:

$$\tau = \frac{\tau_u - G_e \gamma_e}{\gamma_e^2} \gamma^2 + G_e \gamma \quad (4-13)$$

Subsequently, the secant shear modulus, G_{secant} , is obtained by dividing shear stress by shear strain at specific increments as shown in Figure 4-4.

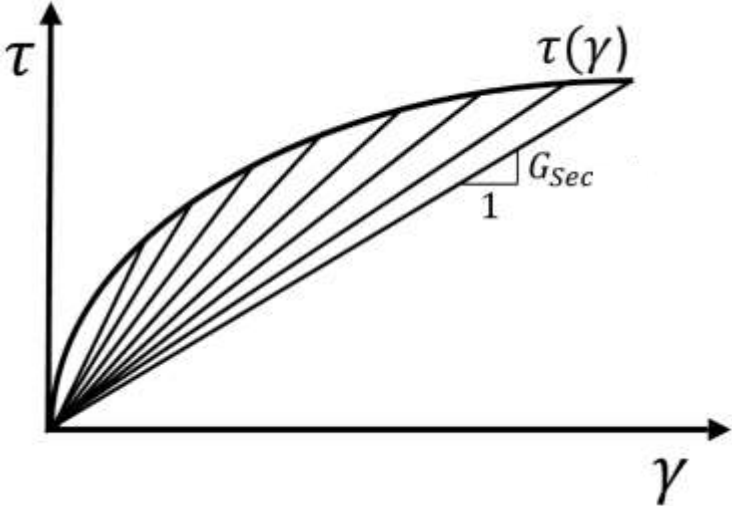


Figure 4-4 Shear stress vs shear strain curve of core component.

$$G_{sec} = \frac{\tau}{\gamma} = \frac{\tau_u - G_e \gamma_e}{\gamma_e^2} \gamma + G_e \quad (4-14)$$

Shear strain can be derived through the rules of trigonometry, as demonstrated in Figure 4-5.

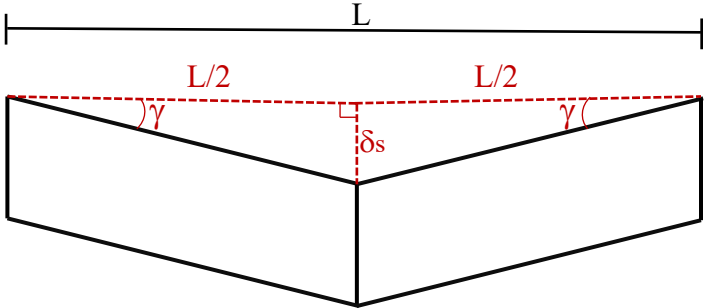


Figure 4-5 Shear deflection of beam under three-point bending.

$$\gamma = \text{Tan}(\gamma) = \frac{\delta_s}{L/2} \quad (4-15)$$

Since the value of shear strain is small, $\tan(\gamma)$ becomes equivalent to γ . Substituting shear strain into equation (4-14), the secant shear modulus become equivalent to:

$$G_{\text{sec}} = \frac{\tau_u - G_e \gamma_e}{\gamma_e^2} \cdot \frac{\delta_s}{L/2} + G_e \quad (4-16)$$

The singular changing variable within the above equation is shear deflection, which depends on the amount of load applied to the beam in three-point bending. Displacement due to shear equation is shown below:

$$\delta_s = \frac{PL}{4(bd)G_{\text{sec}}} \quad (4-17)$$

The first shear deflection step of the non-linear load vs shear deflection model uses the elastic shear modulus—a constant term for developing the linear model. The remainder of the shear deflection steps were based on the secant shear moduli. The flowchart in Figure 4-6 breaks down the procedure for obtaining the shear deflection.

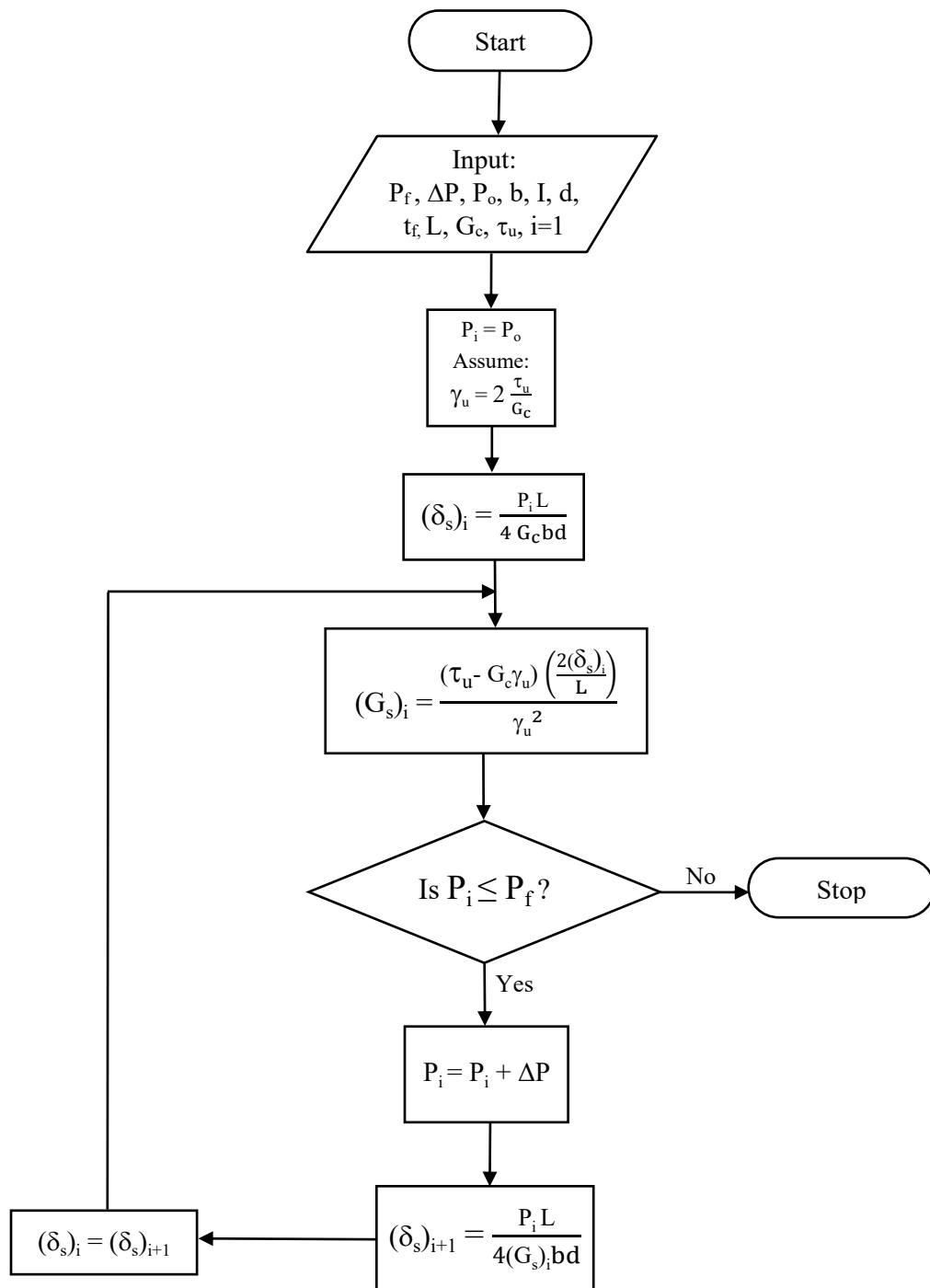


Figure 4-6 Flowchart of shear deflection model.

4.2.3 Verification of Load-deflection models

After developing the load-deflection models using various assumptions, the testing data was compared to the linear and non-linear numerical models. Those models are the sum of shear and bending load-deflection models that were derived in the previous section. The endpoints of the models were distinguished using an iterative procedure illustrated in Figure 4-7, which is carried out due to the bilinear stress-strain correlation associated with the PET FRP sandwich facings. Figure 4-8 presents the load-deflection diagrams for all sandwich panels made from PET FRP facings. The load-deflection diagrams were obtained through the linear models, non-linear models and direct lab testing. As shown in the Figure, the linear model is most accurate at the initial stage of the load-deflection curve. This is because the load-deflection curve of the bending beam starts in a linear trend. Once the behaviour of the load-deflection curve becomes more parabolic, the linear-model gradually becomes less accurate. Therefore, the end behavior is most accurately predicted by the non-linear model. Overall, both models were effectively used to verify the deflection behavior of the tested sandwich beams under applied load.

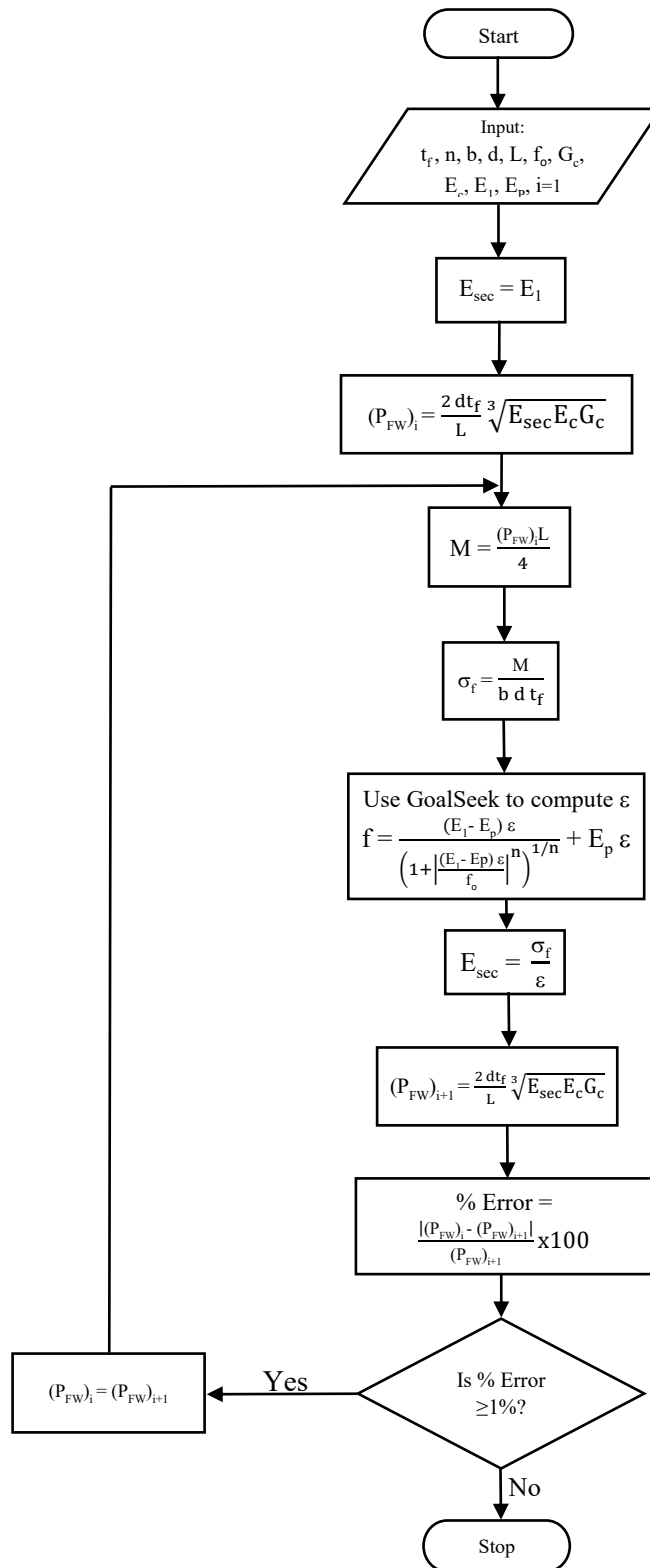


Figure 4-7 Flowchart for determining the failure load of sandwich panels made from PET FRP facings.

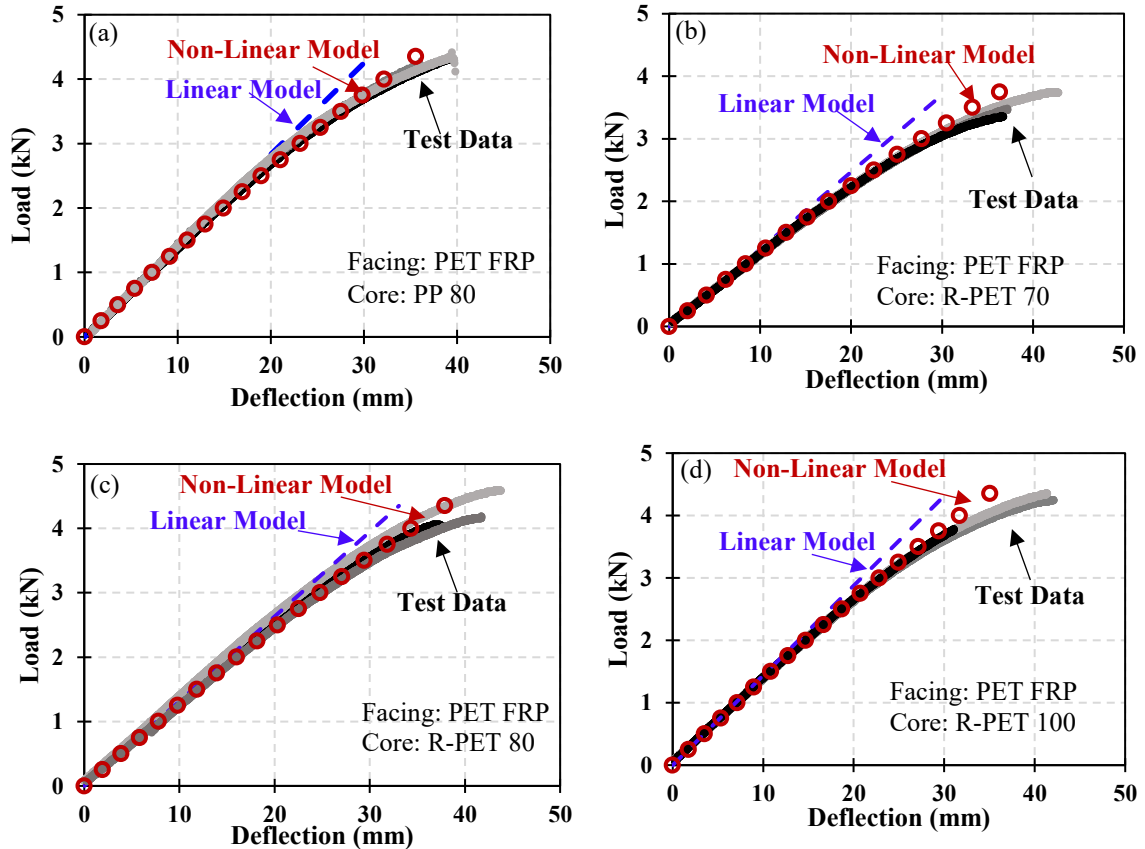


Figure 4-8 Load vs deflection curves of sandwich panel sets made from PET FRP facing and (a) PP honeycomb core, (b) R-PET 70 foam core, (c) R-PET 80 foam core and (d) R-PET 100 foam core, under three-point bending.

4.3 BREAKDOWN OF SHEAR AND BENDING DEFLECTIONS REGARDING CHANGE IN DENSITY OF RECYCLED PET FOAM CORE

As the density of the recycled PET foam core changes, the contribution of shear and bending deflections on the total midspan deflection will change subsequently. This section presents the modeled midspan shear and bending deflections of sandwich panels made from R-PET foam of varying densities. The dimensions of the sandwich panels are equal to the ones fabricated and tested experimentally.

As illustrated in Figure 4-9 and Table 4-1, as the core density increase the impact of midspan shear deflection on the total deflection will decrease. As the core density

increase from 70 kg/m^3 to 80 kg/m^3 the corresponding shear contribution to total deflection at midspan changes from 40% to 35%. However, as the density of the core component increase further from 80 kg/m^3 to 100 kg/m^3 the shear contribution to total deflection decreases 10%. This demonstrates that the shear deflection changes proportionally in conjunction with the change in foam core density.

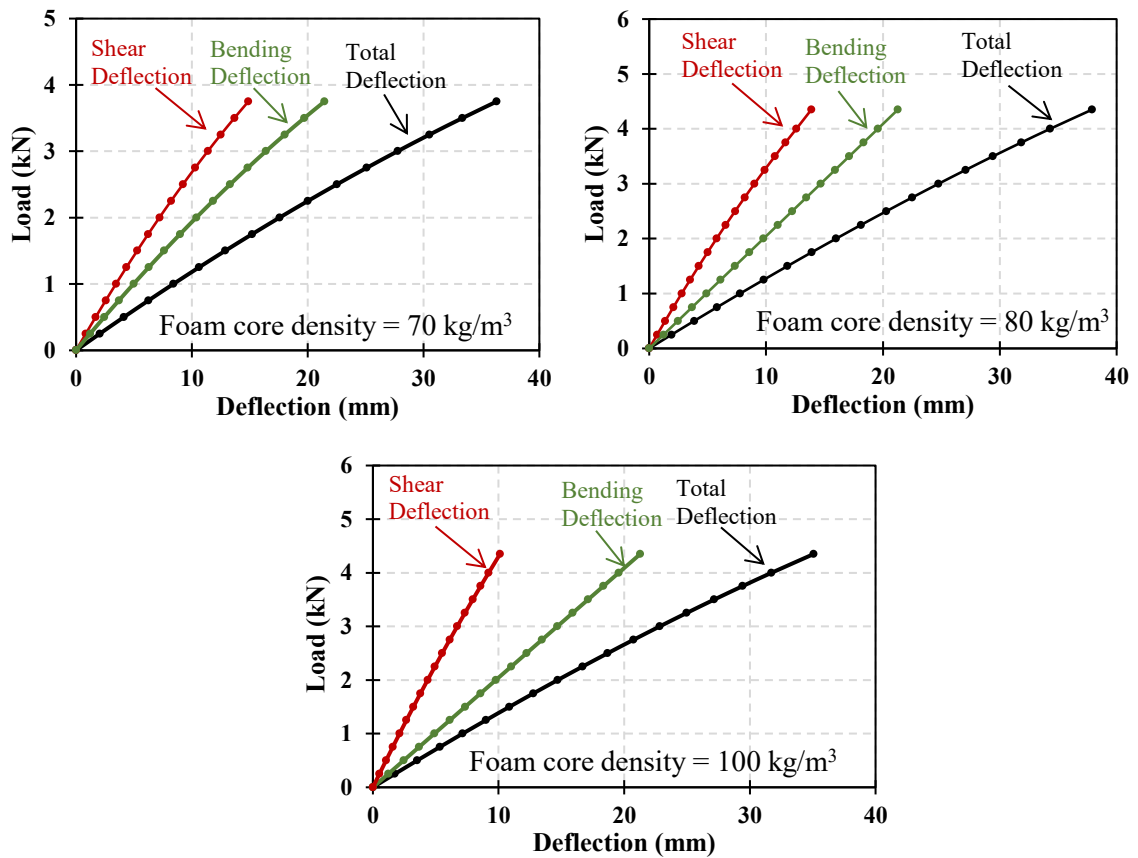


Figure 4-9 Breakdown of total deflection into shear and bending deflections of specimens made from PET FRP facings and R-PET foam core of varying densities.

Table 4-1 Change in shear contribution to total deflection regarding varying core densities

Core Density (Kg/m ³)	Ultimate Midspan Shear Deflection (mm)	Ultimate Midspan Bending Deflection (mm)	Total Midspan Deflection (mm)	Shear Contribution to Total Deflection (%)
70	15	21	36	42
80	14	26	38	37
100	10	26	36	27

4.4 MODELING FAILURE MODES

As mentioned in section 2.5.3.1, an FMM provides useful data for manufacturers and engineers during the design stage of sandwich structures. FMMs were created for all the sets of tested PET FRP-RPET sandwich panels. The three modes of failure presented in the FMM are facing rupture/crushing, core shear and face wrinkling. The equation associate with each mode of failure are presented in chapter 2. The ultimate failure loads of the three anticipated modes of failure were set equal to create the transition lines represented in the model. The progressing equations below illustrate a step-by-step procedure used in deriving the failure mode transition lines.

4.4.1 Transition between Face Rupture and Core Shear

To obtain the transition line between face rupture and core shear zones, the equations corresponding to those modes were set equal as shown below:

$$P_{FR} = P_{CS} \longrightarrow \frac{4 \sigma_f t_f d}{L} = 2dE_c \quad (4-18)$$

Hence, along the transition line, core shear and face fracture have an equal chance of occurring. Since failure mode maps are represented in terms of core density, ρ_c , as a

function of thickness of the face component with respect to span length, $\frac{t_f}{L}$, the elastic modulus term, E_c , was substituted with the relation presented in Figure 3-7(a), which relates the elastic modulus to the core density. Therefore, the transition relation simplifies to:

$$\rho_c = \sqrt[1.12]{223\sigma_f \left(\frac{t_f}{L}\right)} \quad (4-19)$$

4.4.2 Transition between Face Rupture and Wrinkling

The first step in obtaining the transition line between face rupture region and wrinkling region of the failure mode map is stated below; in which the face rupture force was set to the force that causes wrinkling:

$$P_{FR} = P_{FW} \quad \longrightarrow \quad \frac{4\sigma_f t_f d}{L} = \frac{2t_f d}{2L} \sqrt[3]{G_c E_c E_f} \quad (4-21)$$

This relation is further simplified to by crossing out the common factors present in both sides of the equation and substituting the elastic modulus of the core component, E_c and shear modulus, G_c , with the corresponding core density relation obtained from Figure 3-5 and Figure 3-7. Hence the transition line between face rupture and wrinkling regions simplifies to:

$$\rho_c = \sqrt[3.12]{\frac{8221\sigma_f^3}{E_f}} \quad (4-22)$$

The transition equations shown above is not in terms of facing thickness, t_f , and span length, L . Therefore, this transition line is constant with respect to the x-axis.

4.4.3 Transition between Core Shear and Wrinkling

Similar to the transition line equations obtained in the previous sections, transition line between core shear and wrinkling regions are derived by setting the force that triggers core shear equal to the force that triggers wrinkling as shown below:

$$P_{CS} = P_{FW} \longrightarrow 2dE_c = \frac{2t_f d}{2L} \sqrt[3]{G_c E_c E_f} \quad (4-24)$$

The equation is further simplified using Figure 3.5 and Figure 3.7 and becomes as follows:

$$\rho_c = \left[\sqrt[3]{0.001 E_f} \cdot (233) \cdot \left(\frac{t_f}{L} \right) \right]^{1.2} \quad (4-25)$$

Figure 4-10 presents the failure mode map of sandwich panels made from PET FRP facing and R-PET foam core. Standard FMMs are developed using a constant value for the elastic modulus of the facing component; the facing component of conventionally used sandwich panels are made from a material possessing a linear stress-strain correlation. Since the facing components of these sandwich panels are made from a material holding a bilinear stress-strain relationship, the secant and initial elastic moduli were considered when developing FMM.

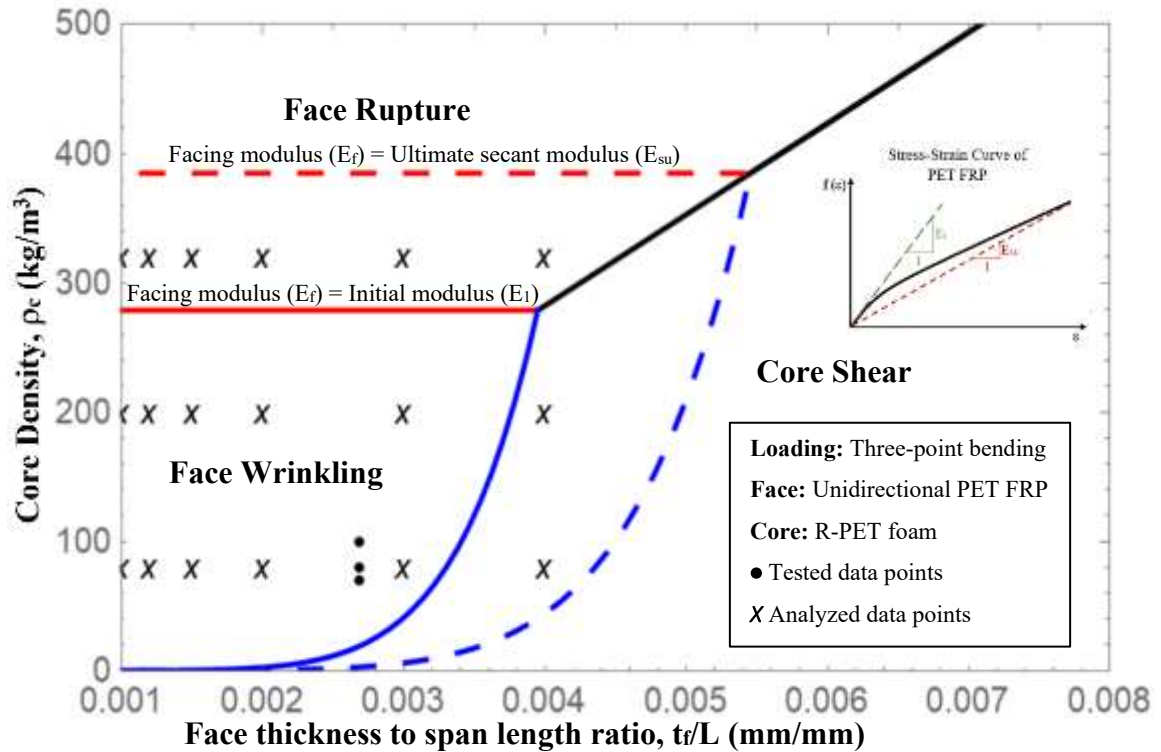


Figure 4-10 Failure mode maps of PET FRP-RPET sandwich panel sets.

4.5 PARAMETRIC STUDY

A parametric study was conducted on sandwich panels made from PET FRP facings and R-PET foam core. This helped further analyse structural behaviour under applied load with respect to additional changing variables not considered during experimental testing. The parameters analysed included thickness of facing component, thickness of core component, unsupported span length, and density of foam core. During the analytical study, each parameter was analysed at a pre-specified range. Concurrently, the dimensional variables and loading configuration were held constant. At this stage, unsupported span length, width, core thickness, and thickness of facing were set to 3m, 78mm, 150mm, and 6mm, respectively. This section presents the load-deflection and load-strain models numerically developed for the range of variables considered within

each parameter. In-depth analysis of the load-deflection models is further discussed within Appendix D of this thesis. All models were terminated at the failure point, which was calculated using the failure mode concept. Tables 4-2, 4-3, and 4-4 present summaries of the main results obtained from the parametric study analysis.

To comprehend the extent of non-linearity of the load-deflection curve, the initial and ultimate stiffnesses were extracted. As illustrated in Figure 4-11, the initial stiffness (K_i) corresponds to the stiffness of the initial linear trend, followed by the load-deflection curve, and the ultimate stiffness (K_u) is the slope of the secant line connected to the endpoint of the graph. The results summed in Tables 4-2, 4-3, and 4-4 illustrates that the ultimate stiffness varies from 40% to 70% of the initial stiffness depending on the density of the core component. As the density of the core component increase the difference of initial and secant stiffness becomes more pronounced.

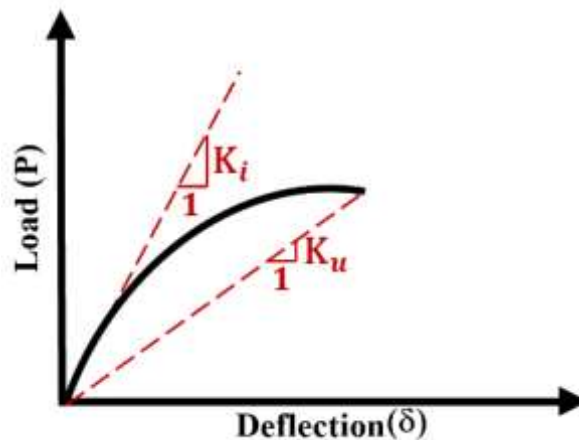


Figure 4-11 Load-deflection curve displaying initial and ultimate-secant stiffnesses.

Table 4-2 Mechanical properties of sandwich panels with varying core thickness and core density ($t_f = 6\text{mm}$, $L = 3\text{m}$)

Core Thickness (mm)	Core Density = 80 kg/m ³							Core Density = 200 kg/m ³							Core Density = 320 kg/m ³						
	Initial Stiffness, K (N/mm)	Ultimate Stiffness, K _u (N/mm)	$\frac{K_u}{K_i}$	Peak Load, P _u (kN)	Total Def. at Peak, δ_u (mm)	Facing Strain at Peak, ϵ_u ($\mu \epsilon$)	Failure Mode	Initial Stiffness, K (N/mm)	Ultimate Stiffness, K _u (N/mm)	$\frac{K_u}{K_i}$	Peak Load, P _u (kN)	Total Def. at Peak, δ_u (mm)	Facing Strain at Peak, ϵ_u ($\mu \epsilon$)	Failure Mode	Initial Stiffness, K (N/mm)	Ultimate Stiffness, K _u (N/mm)	$\frac{K_u}{K_i}$	Peak Load, P _u (kN)	Total Def. at Peak, δ_u (mm)	Facing Strain at Peak, ϵ_u ($\mu \epsilon$)	Failure Mode
75	19.6	13.6	0.69	4.33	319	15300	FW	21.9	10.7	0.49	8.32	770	41000	FW	22.5	9.6	0.43	11.93	1238	66922	FW
100	32.2	22.4	0.70	5.67	252	15279	FW	37.0	18.2	0.49	10.77	590	40782	FW	38.12	16.4	0.43	15.62	951	66940	FW
125	47.2	33.1	0.70	7.01	212	15282	FW	55.7	27.7	0.50	13.31	480	40620	FW	57.7	25.0	0.43	19.30	772	66911	FW
150	64.3	45.4	0.71	8.34	183	15258	FW	77.8	39.1	0.50	15.85	405	40510	FW	81.1	35.3	0.44	23.00	652	66963	FW

Table 4-3 Mechanical properties of sandwich panels with varying face thickness and core density ($t_c = 150\text{mm}$, $L = 3\text{m}$)

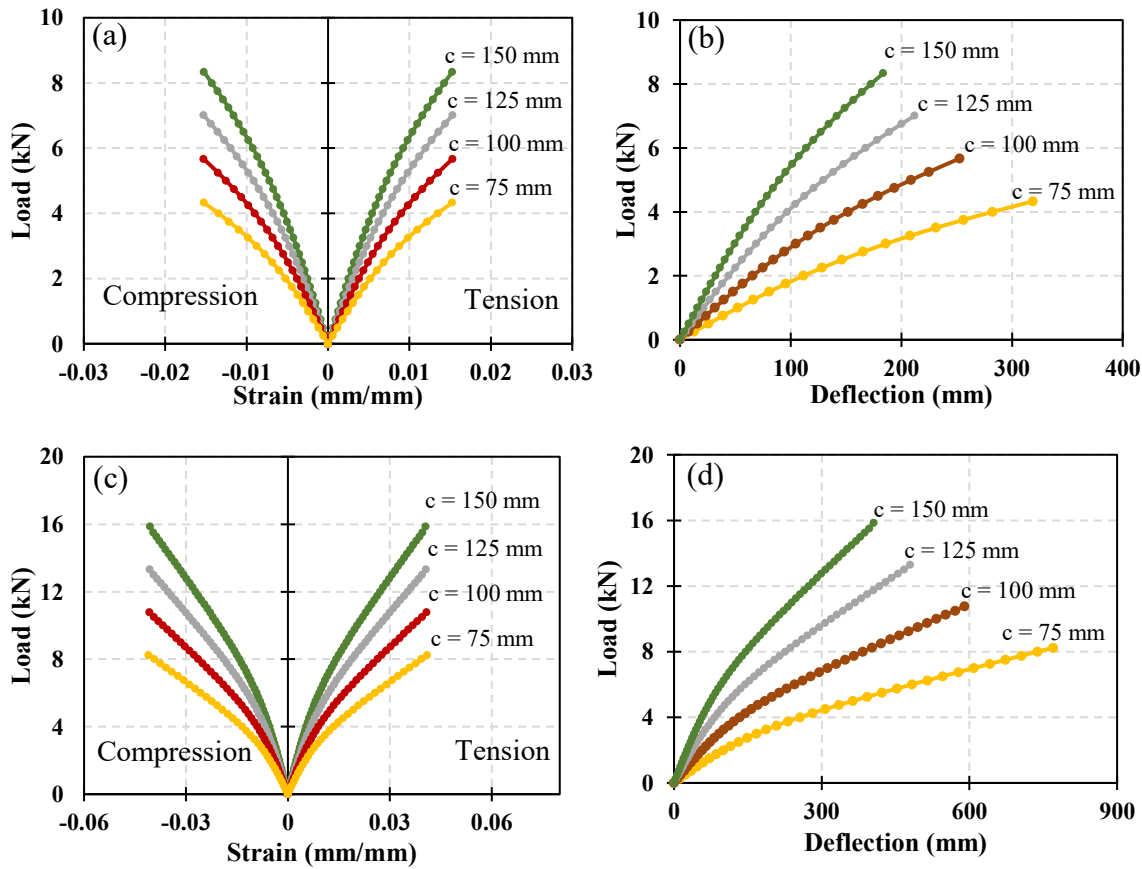
Face Thickness (mm)	Core Density = 80 kg/m ³							Core Density = 200 kg/m ³							Core Density = 320 kg/m ³						
	Initial Stiffness, K (N/mm)	Ultimate Stiffness, K _u (N/mm)	$\frac{K_u}{K_i}$	Peak Load, P _u (kN)	Total Def. at Peak, δ_u (mm)	Facing Strain at Peak, ϵ_u ($\mu \epsilon$)	Failure Mode	Initial Stiffness, K (N/mm)	Ultimate Stiffness, K _u (N/mm)	$\frac{K_u}{K_i}$	Peak Load, P _u (kN)	Total Def. at Peak, δ_u (mm)	Facing Strain at Peak, ϵ_u ($\mu \epsilon$)	Failure Mode	Initial Stiffness, K (N/mm)	Ultimate Stiffness, K _u (N/mm)	$\frac{K_u}{K_i}$	Peak Load, P _u (kN)	Total Def. at Peak, δ_u (mm)	Facing Strain at Peak, ϵ_u ($\mu \epsilon$)	Failure Mode
3	35.6	24.9	0.70	4.09	152	15250	FW	39.4	19.2	0.49	7.78	405	40909	FW	40.2	17.2	0.43	11.28	654	66947	FW
6	64.3	45.4	0.71	8.34	170	15282	FW	77.7	38.8	0.50	15.85	409	40870	FW	81.1	35.3	0.44	23.00	652	66963	FW
9	87.8	59.4	0.68	12.75	201	15264	FW	115.0	58.4	0.51	24.23	415	40884	FW	122.5	53.8	0.44	35.15	653	66954	FW
12	107.3	66.8	0.62	15.25	228	12494	CS	151.0	72.7	0.48	37.63	517	49142	FW	164.2	72.0	0.44	47.70	664	66958	FW

Table 4-4 Mechanical properties of sandwich panels with varying span length and core density ($t_f = 6\text{mm}$, $t_c = 150\text{mm}$)

Span Length (m)	Core Density = 80 kg/m ³							Core Density = 200 kg/m ³							Core Density = 320 kg/m ³						
	Initial Stiffness, K (N/mm)	Ultimate Stiffness, K _u (N/mm)	$\frac{K_u}{K_i}$	Peak Load, P _u (kN)	Total Def. at Peak, δ_u (mm)	Facing Strain at Peak, ϵ_u ($\mu \epsilon$)	Failure Mode	Initial Stiffness, K (N/mm)	Ultimate Stiffness, K _u (N/mm)	$\frac{K_u}{K_i}$	Peak Load, P _u (kN)	Total Def. at Peak, δ_u (mm)	Facing Strain at Peak, ϵ_u ($\mu \epsilon$)	Failure Mode	Initial Stiffness, K (N/mm)	Ultimate Stiffness, K _u (N/mm)	$\frac{K_u}{K_i}$	Peak Load, P _u (kN)	Total Def. at Peak, δ_u (mm)	Facing Strain at Peak, ϵ_u ($\mu \epsilon$)	Failure Mode
3	51.3	29.0	0.57	8.34	237	13580	FW/CS	71.0	36.1	0.51	15.85	438	40870	FW	71.0	33.7	0.47	23.00	683	66963	FW
4	26.3	17.9	0.68	6.26	349	15276	FW	32.4	16.2	0.50	11.89	735	40884	FW	32.4	14.8	0.46	17.25	1168	66963	FW
5	14.9	10.3	0.69	5.01	484	15287	FW	17.3	8.5	0.49	9.51	1119	40870	FW	17.3	7.7	0.45	13.80	1799	66963	FW
6	9.2	6.4	0.70	4.17	656	15258	FW	10.2	5.0	0.49	7.93	1592	40905	FW	10.2	4.5	0.44	11.50	2572	66963	FW

4.5.1 Effect of Core Thickness (Core Density = 80 kg/m³, 200 kg/m³, 320 kg/m³)

Core thickness was analysed at a range between 75mm and 150mm. Change in sandwich panels' mechanical properties with respect to varying core thickness and core density is presented in Table 4-2. As shown in Figure 4-12 (a-f) the load bearing capacity of the sandwich panels increased proportionally with respect to the increase in core thickness. Figure 4-12 (b, d and f) shows that the stiffness increased as core thickness and/or density of the foam core increase. Both load-deflection and load-strain curves appear more bilinear as the core density increase; this is because as the core component of the sandwich panels increase the facing component becomes prone to reaching its ultimate stress-strain capacity—which holds a bilinear correlation.



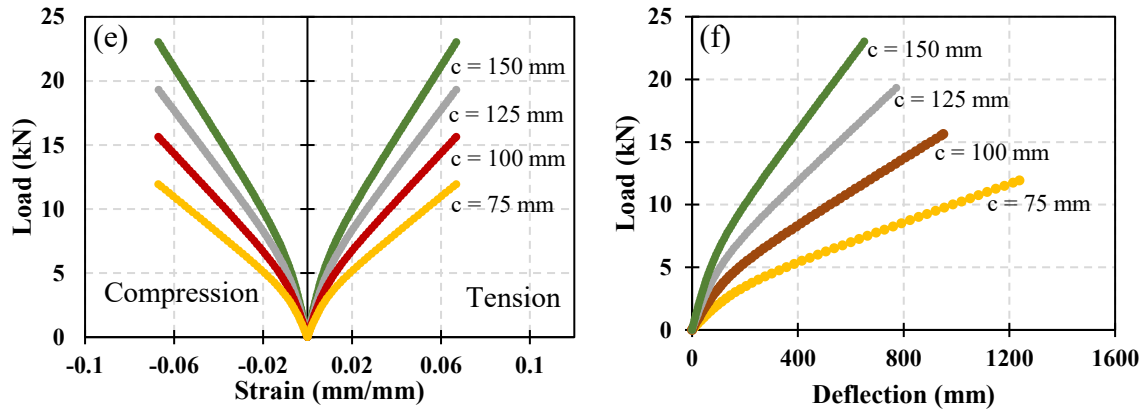


Figure 4-12 Stress-strain and load-deflection curves for sandwich panels with varying core thickness and core density; (a-b) density = 80 kg/m^3 , (c-d) density = 200 kg/m^3 , (e-f) density = 320 kg/m^3 .

4.5.2 Effect of Facing Thickness (Core Density = 80 kg/m^3 , 200 kg/m^3 , 320 kg/m^3)

Sandwich panels' facing thickness was analysed at a range between 3 mm and 12 mm, which corresponds to one and three layers of PET FRP. Table 4-3 the effect of changing face thickness and core density on the mechanical properties of sandwich panels. As illustrated in the previous unit, the facing component dictates the stiffness capacity of the sandwich panel as whole. Therefore, strengthening the facing component increases the stiffness of sandwich beams loaded in three-point bending conditions. This is illustrated in Figure 4-13 (b, c, and d). Since strain and deflection are correlated, increasing the facing thickness results in an decrease of beam's tension and compression strain under a specific applied load as shown in Figure 4-13 (a, c, and e).

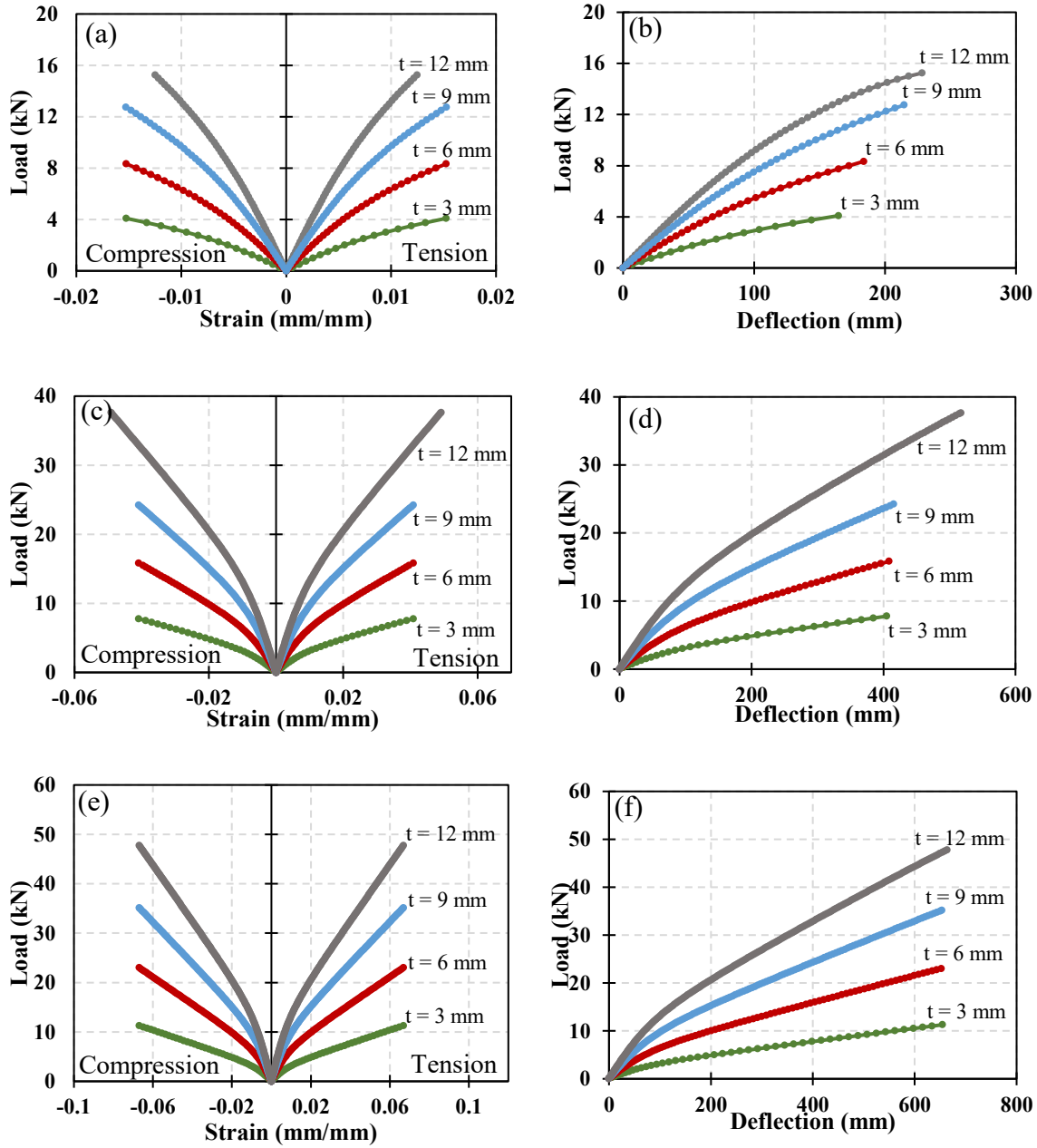
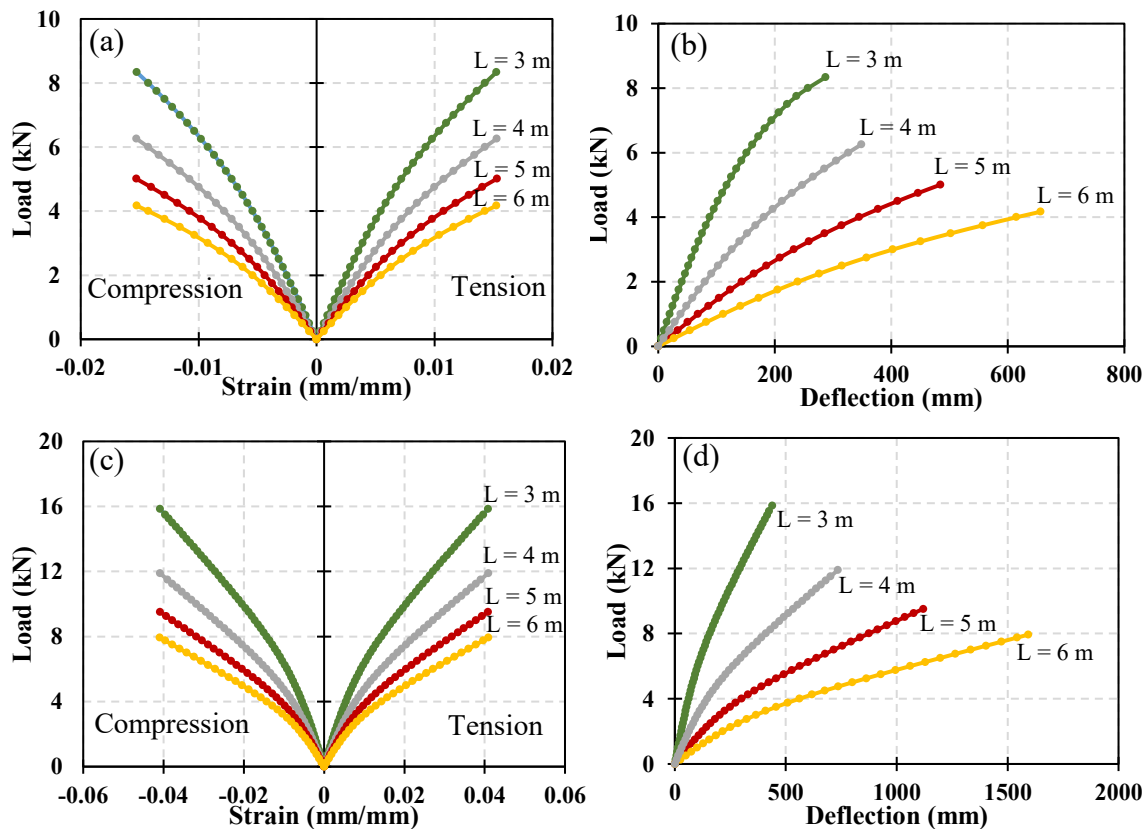


Figure 4-13 Stress-strain and load-deflection curves for sandwich panels with varying facing thickness and core density; (a-b) density = 80 kg/m³, (c-d) density = 200 kg/ m³, (e-f) density = 320 kg/ m³.

4.5.3 Effect of Span Length (Core Density = 80 kg/m³, 200 kg/m³, 320 kg/m³)

Span-length parameter was analysed at a range between 3m and 6m, which was selected to match large and small scale projects involved with sandwich construction. The change in mechanical properties of sandwich panels with varying span length and core density are presented in Table 4-4. As shown in Figure 4-14, an increase in the separation of simple support results in a significant decrease in beam strength capacity as well as an increase in deflection.



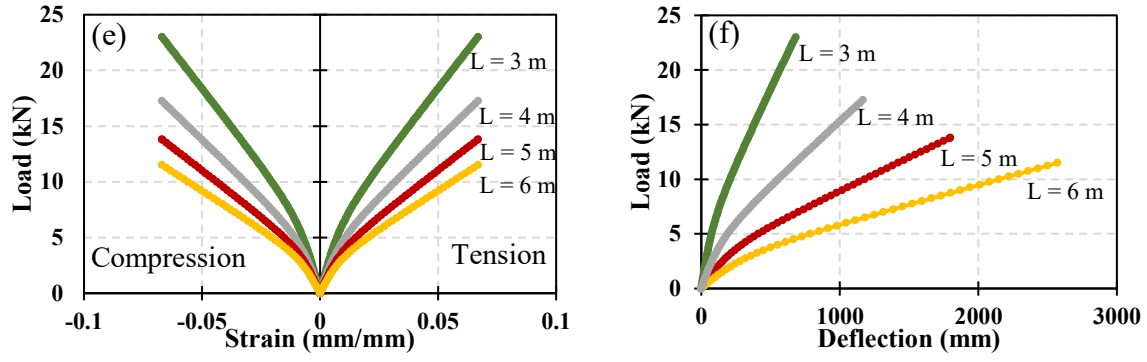


Figure 4-14 Stress-strain and load-deflection curves for sandwich panels with varying span length and core density; (a-b) density = 80 kg/m^3 , (c-d) density = 200 kg/m^3 , (e-f) density = 320 kg/m^3 .

CHAPTER 5 CONCLUSIONS AND RECOMMENDATIONS

5.1 CONCLUSIONS

In this research, new forms of sandwich panels were fabricated, tested in three-point bending loading conditions, and analytically modeled. The motive was to propose a composite product capable of consuming large amounts of recycled plastic and tackle part of the current environmental pollution caused by plastic waste. The sandwich panels were fabricated using two types of plastic core (namely, PP honeycomb and recycled PET foam) and two type of FRP facings (namely, GFRP and PET FRP). The testing matrix covered six different sandwich panel sets. The changing parameters within those sets included: the type of materials used in the facing and core components; the density of the core material used; and the core structure. Thermoplastic sandwich panels were tested and monitored during the entire period as well as sandwich panels made from conventionally used GFRP facings. Also, an analytical model was developed to capture the non-linear behavior of the sandwich specimens based on the non-linearity of both facings and core. Given the analysis of experimental testing results and analytical models, the following conclusions are made:

- Based on the coupon tests, PET FRP composites showed a bilinear stress-stress behavior in tension with distinctive initial and secondary moduli and yielding strength. It was shown that PET FRPs had four times more strain capacity and 25% less stress capacity compared to conventionally used GFRP composite created from the same polymer matrix.
- The Richard-Abbott equation can be adopted to model the bilinear stress-strain behavior of the PET FRPs in tension. Additional constants developed in this thesis

can be used to predict the full stress-strain relationship of PET FRP composites based on the initial modulus and yielding strength.

- The ideal recycled PET foam core density to be used for sandwich beams should be 80 kg/m^3 —according to the load-deflection curves of the tested beams. Beyond the density of 80 kg/m^3 , sandwich panel stiffness remained fairly constant.
- The load-deflection behavior of thermoplastic sandwich panels is non-linear, which derives from both the thermoplastic core and facing components.
- The failure mode of sandwich panels tested under lab conditions is challenging to correctly interpret: face rupture, core shear, and face wrinkling can all occur sequentially during an incredibly short time interval—just as the test is terminated. Through slow motion videos, face wrinkling failure was identified as the main mode of failure for sandwich specimens with PET FRP facing triggering the shear failure of the PET foam cores.
- Increasing the foam core density of sandwich panels made from PET FRP facing and recycled PET foam core will decrease the contribution of shear deflection to the total deflection. According to the developed analytical model, the percentage of shear deflection to the total deflection of sandwich panels made from recycled PET foam core with densities of 70 kg/m^3 , 80 kg/m^3 and 100 kg/m^3 are equivalent to 42%, 37%, and 27%, respectively. Hence, the contribution of shear deflection change proportionally in conjunction with foam core density.
- The majority of the analytically-analysed sandwich panels failed in face wrinkling rather than core shear or face rupture. Hence, due to the large strain capacity

associated with thermoplastics, the governing mode of failure of panels made from PET FRP facings and recycled PET foam core is likely face wrinkling.

- Based on the parametric analysis of sandwich panels made from PET FRP facings and recycled PET foam core of varying densities, doubling the thickness of the sandwich facing or core components, or dividing the span length by two, equals the same effect regarding change in ultimate load capacity resisted by sandwich panels.
- Due to the bilinear stress-strain correlation of PET FRP, failure mode maps created for sandwich panels made from PET FRP facings must consider the secant moduli of the facing at wrinkling load to identify the boundary of the failure modes correctly.

5.2 RECOMMENDATIONS FOR FUTURE RESEARCH

The following list includes recommendations and suggestions for future research:

- In-depth understanding of the chemical bond between fibres and adhesive polymer to achieve a strong composite and avoid premature failure.
- Study the effect of long-term/sustained loads on sandwich panels to analyse fatigue capacity.
- Analyze the mechanical performance of sandwich panels under dynamic loading condition to further understand load-bearing behavior.
- Conduct testing on large scale sandwich panels and study the effect of size variation on strength parameter.

BIBLIOGRAPHY

- Aizenshtein, E. M. (2009). Polyester fibres continue to dominate on the world textile raw materials balance sheet. *Fibre Chemistry*, 41(1), 1–8.
- Allen, H. G. (1969). *Analysis and Design of Structural Sandwich Panels* (1st ed.). Oxford: Pergamon.
- Andrady, A. L., & Neal, M. (2009). Applications and Societal Benefits of Plastics. *Philosophical Transactions of The Royal Society B Biological Sciences*, 364, 1977–1984.
- Anil, R. R., Ladani, R. B., Wu, S., Kinloch, A. J., Wang, C. H., & Mouritz, A. P. (2018). The Electric Field Alignment of Short Carbon Fibres to Enhance the Toughness of Epoxy Composites. *Composites Part A: Applied Science and Manufacturing*, 106, 11-23.
- Anshuman, S. (2018). *Introduction to Plastics Engineering*. Cambridge, MA: William Andrew.
- Armacell. (2018). *Armacell*. Retrieved 12 24, 2019, from https://local.armacell.com/fileadmin/cms/pet-foams/TDS/ArmaForm_Core/Core_TDS_0076_201800806.pdf
- Auxx.me*. (2019). Retrieved September 27, 2019, from <https://auxx.me/you-will-want-to-recycle-everything-after-seeing-these-photos/86-10/>
- Betts, D., Sadeghian, P., & Fam, A. (2018). Experimental Behavior and Design-Oriented Analysis of Sandwich Beams with Bio-Based Composite Facings and Foam Cores. *Journal of Composites for Construction*, 22(4), 1-36.
- Bisinella, V., Albizzati, P. F., Astrup, T. F., & Damgaard, A. (2018). *Life Cycle Assesment of Grocery Bags*. Denmark: The Danish Environmental Protection Agency.
- CCME. (2018). *strategy on zero plastic waste*. Canadian Council of Ministers of the Environment.
- Christopher, R. J. (2018). Plastic pollution and potential solutions. *Science Progress*, 101(3), 207-260.
- Chu, J. (2017). *MIT News*. Retrieved November 2, 2019, from <http://news.mit.edu/2017/fortify-concrete-adding-recycled-plastic-1025>
- Cool Healthy Recipes*. (2015). Retrieved September 12, 2019, from <http://www.coolhealthyrecipes.com/are-plastic-bottles-poisoning-us-what-do-those-recycling-symbols-and-codes-at-the-bottom-mean/>

- Discover Natural Fibres Initiative. (2019, February 20). *Textile Network*. Retrieved December 14, 2019, from <https://textile-network.com/en/Technical-Textiles/Fasern-Garne/Forecast-world-fibre-production>
- Dodiuk, H., & Goodman, S. H. (2014). *Handbook of Thermoset Plastics* (3 ed.). Elsevier.
- FAO. (2011). *Food and Agriculture Organization* . Retrieved September 29, 2019, from <http://www.fao.org/food-loss-and-food-waste/en/>
- Flip, N. (2013). *Fine Art America*. Retrieved September 22, 2019, from <https://fineartamerica.com/featured/bottlenose-dolphin-with-plastic-six-flip-nicklin.html>
- François, G., Christopher, K. P., & Julia, R. (2017). *Plastic Pollution*. Lausanne: Frontiers Media SA .
- Gibson, L., & Ashby, M. (1999). *Cellular Solids: Structure and Properties* (2 ed.). Cambridge: Cambridge University Press;.
- Government of Canada. (2017). *Justin Trudeau, Prime Minister of Canada*. Retrieved September 28, 2019, from <https://pm.gc.ca/en/news/news-releases/2017/12/14/prime-minister-unveils-themes-canadas-2018-g7-presidency>
- Groves, D. (2019). *Whales and Dolphin Conservation*. Retrieved September 22, 2019, from <https://uk.whales.org/2019/04/02/nature-may-have-the-answer-to-plastic-pollution/>
- Hammer, S., Nager, R., Johnson, P., Furness, R. W., & Provencher, J. (2016). Plastic debris in great skua (*Stercorarius skua*) pellets corresponds to seabird prey species. *Marine Pollution Bulletin*, 103(1-2), 206-210.
- Harrison, R. M. (2019). *Plastics and the Environment*. Cambridge: Royal Society of Chemistry.
- Hester, R. E., & Harrison, R. M. (2019). Microplastics in the Environment. In R. E. Hester, & R. M. Harrison (Eds.), *Plastics and the Environment* (pp. 60-81). Croydon: Royal Society of Chemistry.
- Hidayah, N., & Syafudin. (2018). A Review on Landfill Management in the Utilization of Plastic Waste as an Alternative Fuel . *EDP Sciences* , 31, 1 - 6.
- Hopewell, J., Dvorak, R., & Kosior, E. (2009). Plastics Recycling: Challenges and Opportunities. *Philosophical Transactions: Biological Sciences*, 364, 2115-2126.
- Jambeck, J., Geyer, R., Wilcox, C., Siegler R, T., Perryman, M., Andrady, A., . . . Lavender Law, K. (2015). Plastic waste inputs from land into the ocean. *Science*, 347(6223), 768-771.
- Juran, R. (1989). *Modern Plastics Encyclopedia* (11 ed.). Heightstown, New Jersey: McGraw-Hill .

- Kelly, W. (2016). *Illinois*. Retrieved September 22, 2019, from <https://blogs.illinois.edu/view/789/380569>
- Kuen, E. (1959). *Structural Sandwich Design Criteria*. Wisconsin: University of Wisconsin.
- Laist, D. W. (1997). *Impacts of Marine Debris: Entanglement of Marine Life in Marine Debris Including a Comprehensive List of Species with Entanglement and Ingestion Records* (Springer Series on Environmental Management ed.). New York City: Springer-Verlag.
- Larco, C., Pahonie, R., & Ioana, E. (2015). The Effects of Fibre Volume Fraction on a Glass-Epoxy. *INCAS BULLETIN*, 7, 113-119.
- Leavy, T. (2018). *CBS News*. Retrieved September 22, 2019, from <https://www.cbsnews.com/news/florida-saltwater-brewery-non-plastic-six-pack-rings-spare-sea-turtles/>
- Lofgren, K. (2014). *Inhabitat*. Retrieved September 27, 2019, from <https://inhabitat.com/donate-to-suck-millions-of-tons-of-plastic-out-of-the-worlds-oceans/>
- Macpherson, A. (2014). *Municipal Solid Waste Landfills*. North Carolina : U.S. Environmental Protection Agency .
- Matthias, K., & Alexandra, P. (2014). Theodor Billroth's vision and Karl Ziegler's action: Commemoration of the 40th day of death and the 50th anniversary of conferment of Nobel Prize for Chemistry of Karl Ziegler. *Surgery*, 155(2), 347-349.
- Moore, C. J. (2008). Synthetic polymers in the marine environment: A rapidly increasing, long-term threat. *Environmental Research*, 108, 131-139.
- Mudgal, S., Lyons, L., Bain, J., Dias, D., Faninger, T., & Johansson, L. (2011). *Plastic Waste in The Environment*. Paris: Bio Intelligence Service .
- Office of Consumer Affairs. (2019, April 1). *Government of Canada* . Retrieved December 14, 2019, from <https://ic.gc.ca/eic/site/oca-bc.nsf/eng/ca02747.html>
- Olagoke, O., & Kolapo Peluola, A. (2016). *Hand Book of Thermoplastics* (2nd ed.). Florida: Taylor and Francis Group.
- Palm, E., & Svensson, E. M. (2018). *Mapping the plastics system and its sustainability challenges*. Lund: Lund University.
- Pathak, S., Sneha, C., & Baby Mathew, B. (2014). Bioplastics: Its Timeline Based Scenario & Challenges. *Journal of Polymer and Biopolymer Physics Chemistry*, 2(4), 84 - 90.
- Pearce, A. R., Ahn, Y. H., & Hanmi, K. C. (2018). *Sustainable buildings and infrastructure : paths to the future* (2 ed.). New York: Abingdon .

- Pilz, H., Schweighofer, J., & Kletzer, E. (2005). *The Contribution of Plastic Products to Resource Efficiency*. Vienna: Gesellschaft für umfassende Analysen.
- Plastic Europe. (2015). Retrieved September 5, 2019, from <https://www.plasticseurope.org>
- Ragaert, K., Delva, L., & Van Geem, K. (2017). Mechanical and Chemical Recycling of Solid Plastic Waste. *Waste Management*, 69, 24-58.
- Raheem, D. (2013). Application of plastics and paper as food packaging materials – An overview. *Emirates Journal of Food and Agriculture*, 25(3), 177-88.
- Reay, D., Smith, P., & Amstel, A. (2012, January). Methane and Climate Change.
- Reisser, J., Shaw, J., Wilcox, C., Hardesty, B. D., Proietti, M., Thums, M., & Pattiaratchi, C. (2013). Marine Plastic Pollution in Waters around Australia: Characteristics, Concentrations, and Pathways. *PLOS ONE*, 8(11), 1-11.
- Rhodes, C. J. (2018). Plastic Pollution and Potential Solutions. *Science Progress*, 207–260.
- Richard, R., & Abbott, B. (1975). Versatile Elastic-Plastic Stress-Strain Formula. *Journal of the Engineering Mechanics Division*, 101, 511-515.
- Ryan, P. G., Moore, C., Franeker, J. A., & Moloney, C. L. (2009). Monitoring the abundance of plastic debris in the marine environment. *Philosophical Transactions of the Royal Society B*, 364(1526), 1999–2012.
- Santos, R. G., Andrades, R., Boldrini, M. A., & Martin, A. S. (2015). Debris Ingestion by Juvenile Marine Turtles: An Underestimated Problem. *Marine Pollution Bulletin*, 37–43.
- Shelton, S. (2019). *GreenBiz*. Retrieved September 22, 2019, from <https://www.greenbiz.com/article/can-your-brand-help-concerned-consumers-kick-single-use-plastics-habit>
- Sinclair, G. (2014). ESG in Finance Symposium for Villanova School of Business 22 October 2014. Pennsylvania: Economy & Finance.
- Smith, K. T. (2018). How Plastic Pollution is Affecting the Ocean. *Azo Clean Tech*, 1-4.
- Smith, M., Love, D. C., Rochman, C. M., & Neff, R. A. (2018). Microplastics in Seafood and the Implications for Human Health. *Current Environmental Health Reports*, 5(3), 375-386.
- Stewart, R. (2005). Medical Plastics. *Plastics Engineering*, 61(10), 20 -24, 26.
- Thompson, A. (2018). *Scientific American*. Retrieved September 2019, 2019, from <https://www.scientificamerican.com/article/from-fish-to-humans-a-microplastic-invasion-may-be-taking-a-toll/>

- Thompson, R. C., & Pahl, S. (2019). Plastics, the Environment and Society: Current Consensus and Future Directions. *royal society of chemistry*(47), 177-187.
- Thomsen, Bozhevolnaya, & Lyckegaard. (2005). *Sandwich Structures 7: Advancing with Sandwich Structures and Materials*. Aalborg: Aalborg University.
- Timm, A. (2018). How Injection Molded Plastics Measure Up In Aerospace Applications. *Appliance Design*, 66(10), 30-33.
- Timoshenko, S. (1953). *History of Strength of Materials*. New York: Dover Publications.
- U.S. Energy Information Administration. (2012). Retrieved December 12, 2019, from <https://www.eia.gov/todayinenergy/detail.php?id=6970>
- United Nations. (2018). *United Nations*. Retrieved December 14, 2019, from <https://news.un.org/en/story/2018/06/1011351>
- Wang, Q., Howell, M., Yoshioka, Y., & Clement, G. (2014). Comparison Between Diffuse Infrared and Acoustic Transmission Over The Human Skull. *The Journal of the Acoustical Society of America*, 136(4), 1-7.
- Washam, C. (2010, April). *American Association of Chemistry Teachers* . Retrieved November 2, 2019, from <https://www.acs.org/content/acs/en/education/resources/highschool/chemmatters.html>
- Wilson, K. (2017). *Marine Conservative Society*. Retrieved September 27, 2019, from <https://www.mcsuk.org/news/turtle-eats-plastic-bag>
- Worm, B., Lotze, H. K., Jubinville, I., Wilcox, C., & Jambeck, J. (2017). Plastic as a Persistent Marine Pollutant. *Annual Review of Environment and Resources*, 42, 1–26.
- Wright, S. L., Thompson, R. C., & Galloway, T. S. (2013). The physical impacts of microplastics on marine organisms: A review. *Environmental Pollution*, 178, 483-492.
- Wuennenberg, L., & Tan, C. M. (2019, July). *International Institute for Sustainable Development*. Retrieved September 28, 2019, from <https://iisd.org/about/about-iisd>
- Zenkert, D. (1997). *The Handbook of Sandwich Construction*. Cradley Heath: Engineering Materials Advisory Services Ltd.
- Zheng, Y., Yanful, E. K., & Bassi, A. S. (2008). A Review of Plastic Waste Biodegradation. *Critical Reviews in Biotechnology*, 25(4), 243-250.

APPENDIX A: Details on PP Honeycomb Core Modeling

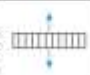
A1 Overview

The polypropylene honeycomb structure used as the core component of multiple sandwich panel sets were modeled using finite element simulation. The model was created using SOLIDWORKS 2019. The technical data sheet provided by the manufacturer of the core was used to create and verify the values obtained by the model. Table A1-1—extracted from the technical data sheet—illustrates the testing set-ups that were used by manufacturer to obtain the listed mechanical properties.

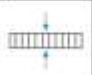
Table A1-1 Mechanical properties and testing configuration of PP honeycomb

PP Honeycomb Core Mechanical Properties																								
CORE	CELL SIZE		DENSITY				FLATWISE TENSILE ¹		BARE COMPRESSION ²						PLATE SHEAR ³									
			TYPICAL		MINIMUM		TYPICAL STRENGTH		STRENGTH			MODULUS			STRENGTH			MODULUS						
			lb/ft ³	kg/m ³	lb/ft ³	kg/m ³	psi	MPa	psi	MPa	psi	MPa	psi	MPa	psi	MPa	psi	MPa	psi	MPa	psi	MPa		
PP1-5.0-N1-8	0.315	8	5	80.0	4.75	75.0	130	0.89	275	1.89	255	1.55	11.5	79.2	9.5	65.4	85	0.58	75	0.52	2.2	15.2	1.7	11.7
PP1-4.0-N1-10	0.395	10	4	64.0	3.8	60.0	120	0.83	180	1.24	140	0.96	10.5	72.3	8.5	58.5	60	0.41	55	0.38	2.0	13.8	1.5	10.3


¹ Flatwise Tensile
Tested per ASTM C 267
Room Temperature, core
specy used



² Bare Compression
Tested per ASTM C 365



³ Plate Shear
Tested per ASTM C 273



The data provided is based on the testing of 21 (not only) various of each core type.

A1 Development of SolidWorks Model

Plastic polymers vary depending on the process used in the manufacturing. Hence, same grade plastic can have slightly different properties and strength characteristics. Therefore, the material properties of polypropylene including its density were inputted manually using from the technical data sheet and properties of polypropylene found on SolidWorks. Two polypropylene cylinders were first created in the model. The cylinders were infused and were positioned at a 60 degrees angle as shown in Figure A2-1(a). Using the pattern

function, the two cylinders were reduplicated to form the honeycomb structure illustrated in part (b) of the Figure. The edges of the structure were then cut, as demonstrated in Figure A2-1(c) to prepare the structure for the applied stresses.

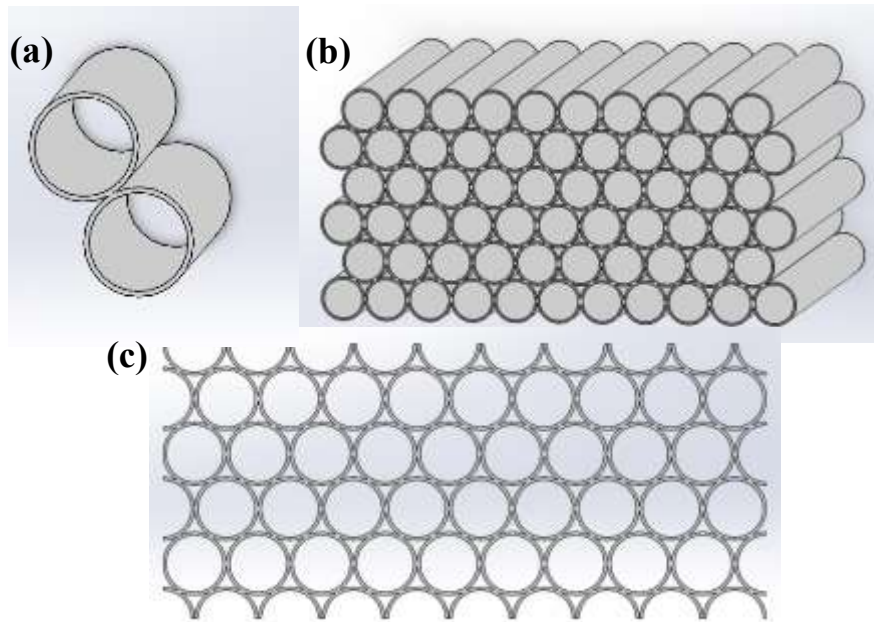


Figure A2-1 Development of honeycomb model

It should be noted that the PP cylinders provided by the manufacturer were linked together using an adhesive. Infusing the cylinders in the analytical model rather than gluing them is justified because stresses applied on the model were in the direction of compression. Which means that the cylinders were never pulled apart during testing.

A3 Applying Stress on Developed Model

The model was loaded in shear and bear compression to compare the results obtained by the model to the ones provided by the manufacturer. The model was modified slightly and

the boundary conditions were set distinctly according to the orientation of the stress prior to applying the load.

A3.1 Shear Test

The model was modified for this test by attaching two plates on the top and bottom faces of the honeycomb structure to allow for an even stress distribution. The bottom plate was fixed and restrained from moving in the “x” and “y” planes. Meanwhile, the top face was restrained in the “y” direction only. Prior to applying the force on the model, model was meshed using the finest mesh option in Solidworks as shown in Figure A3-1.

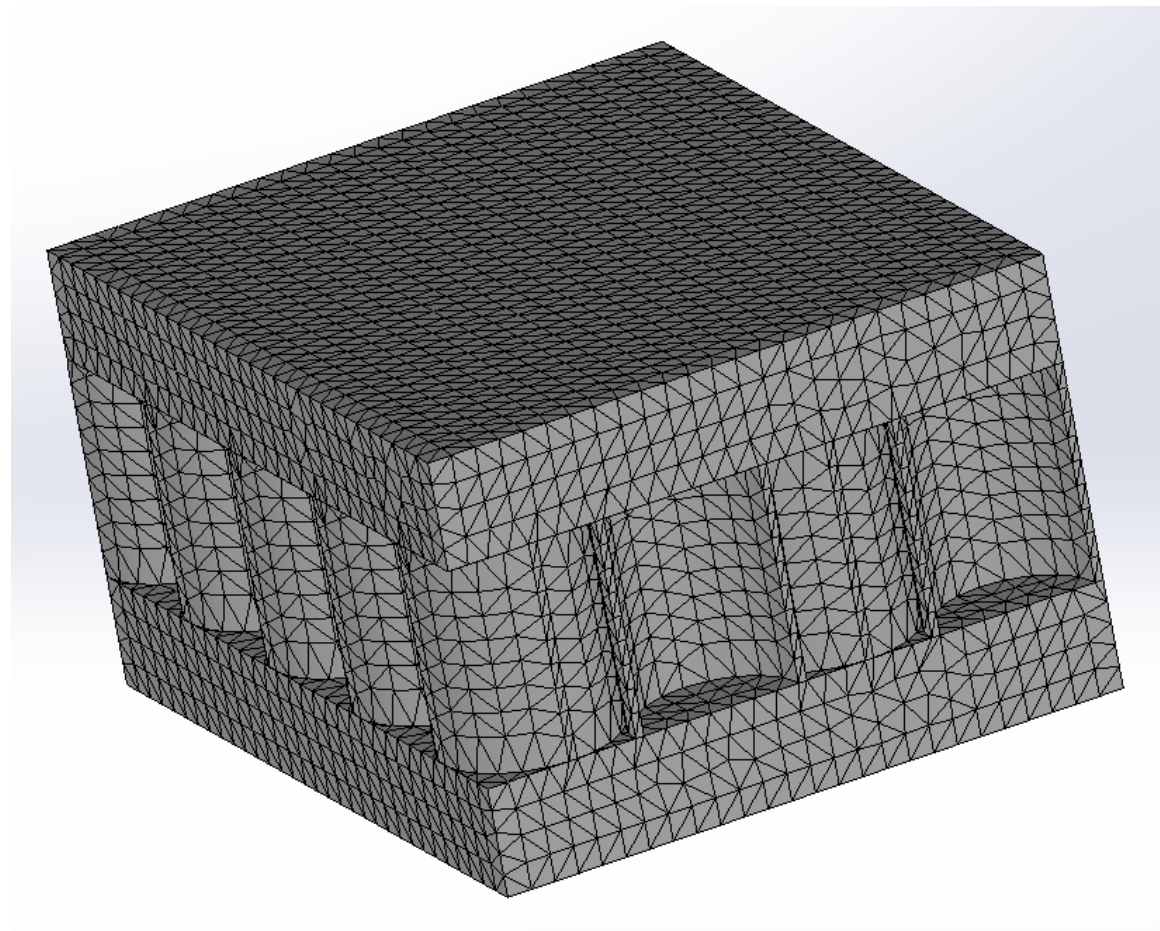


Figure A3-2 Meshed model of PP honeycomb structure.

Figure A3-2, illustrates the displacement of the model after applying shear stress over the area of the top plate.

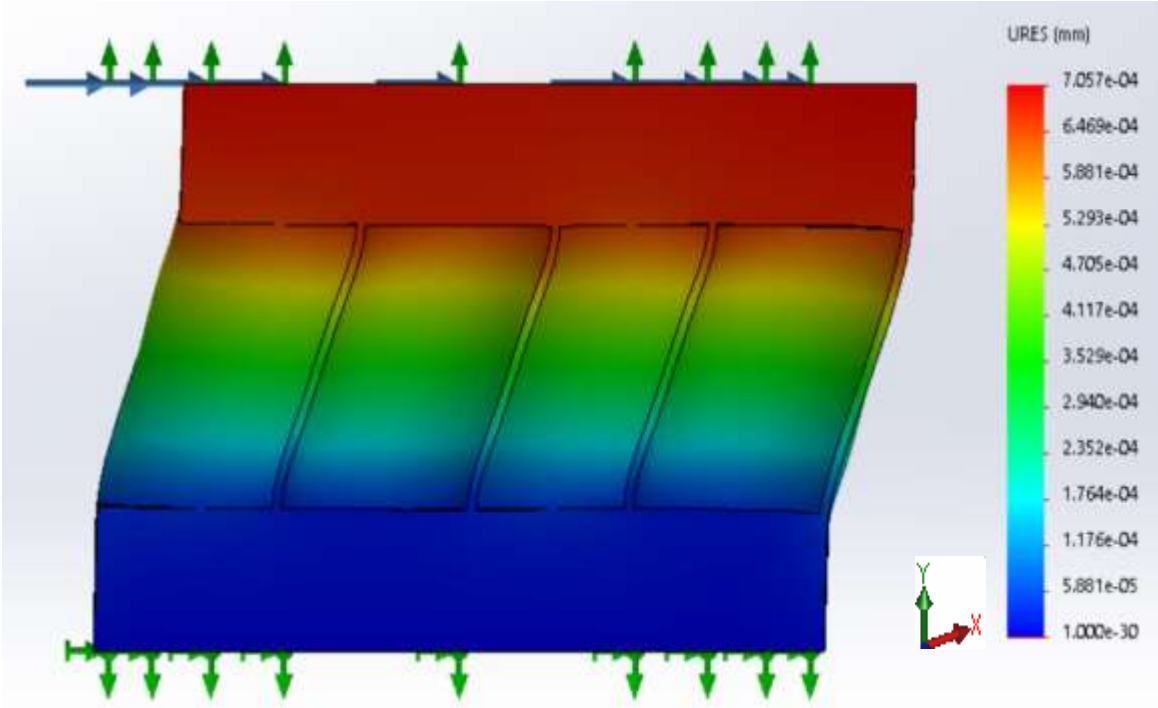


Figure A3-2 Shear displacement of modeled honeycomb core.

The shear modulus was calculated based on the shear displacement model. Two points were selected on the same “y” plane, as shown in Figure A3-3, to calculate the change in displacement caused by the shear stress.

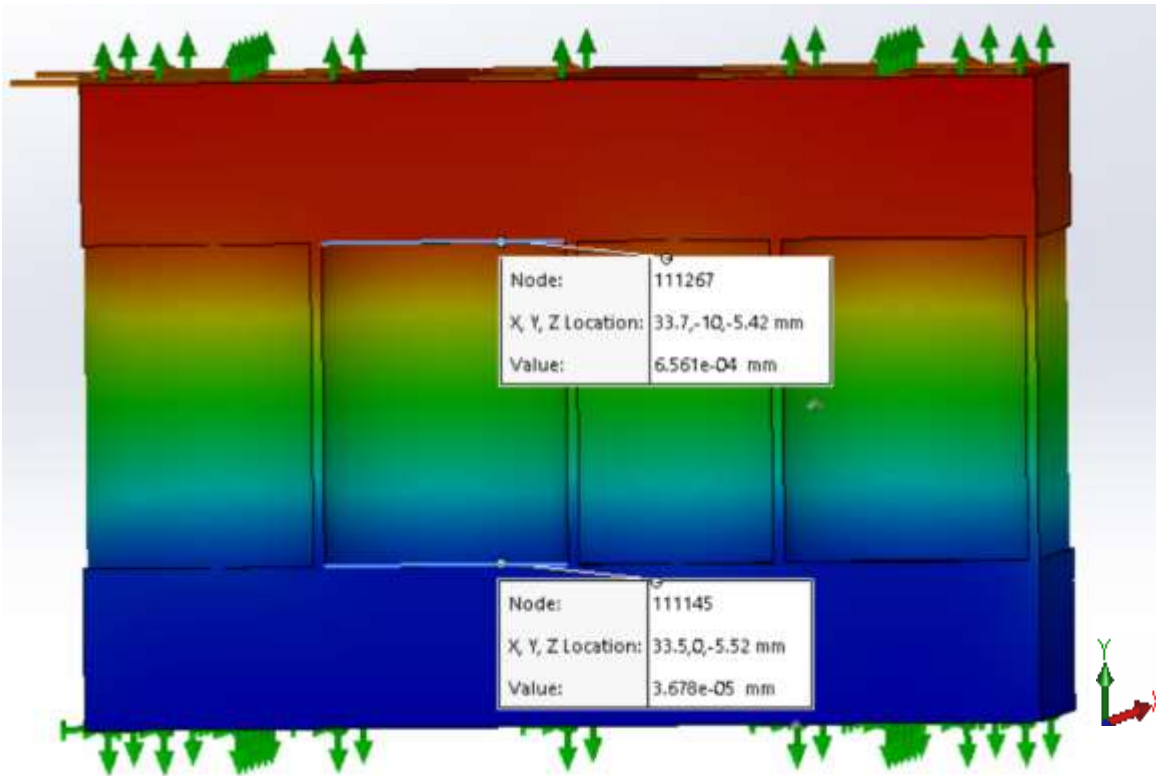


Figure A3-3 Displacement values on two points selected from the shear displacement model.

A3.1.1 Shear Modulus Sample Calculation

Shear modulus, G_c , is calculated using the following equation:

$$G_c = \frac{F \cdot L}{A \cdot \Delta x}$$

In which F is the sum of applied force, L is the vertical distance between the plates, A is the area on which the force is distributed and Δx is the horizontal shear displacement. A 1N force was applied in shear over the area of the plate. The plate's area was precisely measured to be 1098.3 mm² using the "evaluate-measure" function in solidworks as shown in Figure A3-4.

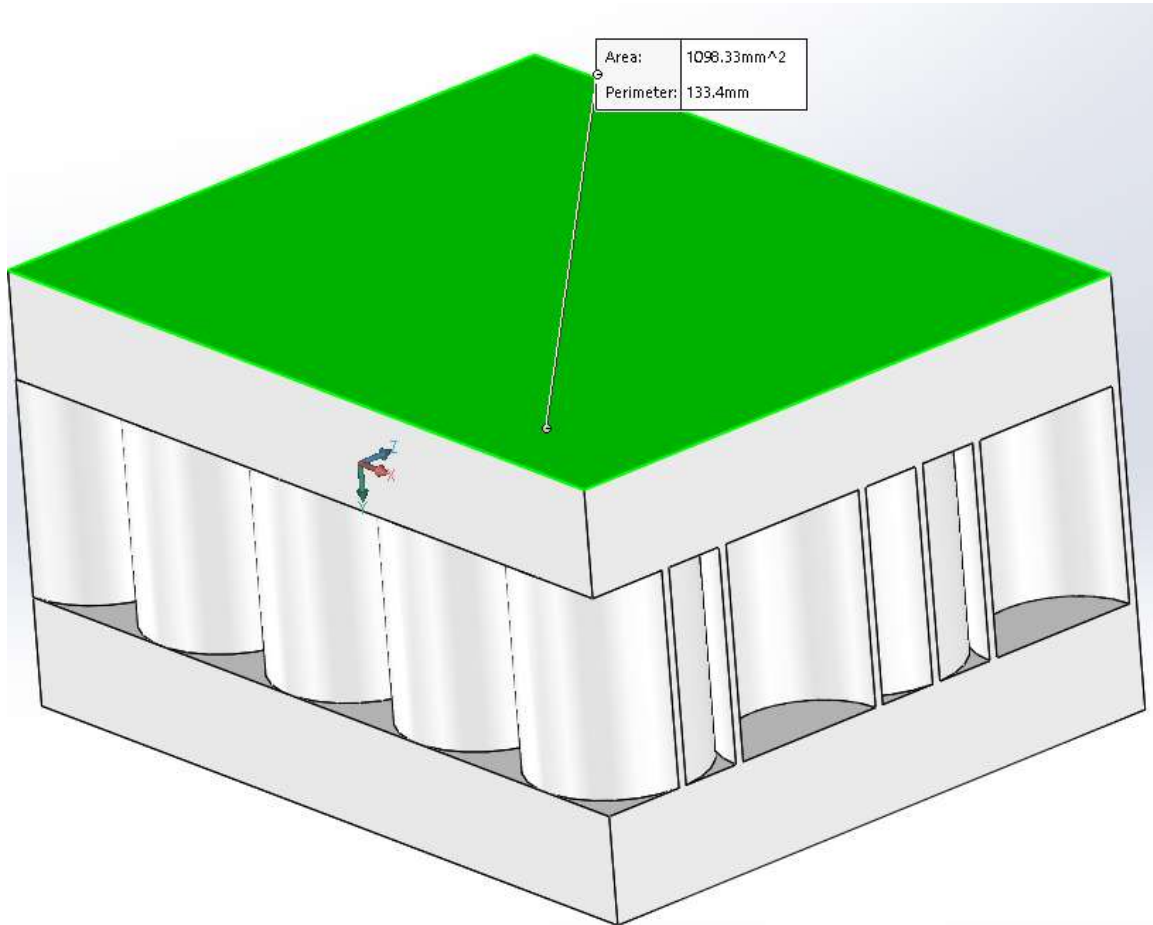


Figure A3-4 Area of the top plate.

The vertical distance between the top and bottom plates was equal to 10 mm. After determining the required variables the shear modulus equation is then simplified as shown below:

$$G_c = \frac{(1N) \cdot (10mm)}{(1098.3 \text{ mm}^2) \cdot ((6.561 \cdot 10^{-4} \text{ mm}) - (3.678 \cdot 10^{-5} \text{ mm}))} = 14.7 \text{ MPa}$$

The honeycomb core manufacturer reports the shear modulus as 15.2 MPa as shown in Table A1-1. This proves that the model developed in solidworks is in good agreement with the experimental testing results.

A3.2 Bare Compression Test

To identify the elastic modulus of the honeycomb structure in bare compression, two plates were attached to the top and bottom faces of the structure; which allows the compressive force to distribute evenly and simulate the load-distribution in sandwich panels. The model was fixed from the bottom face only. This face was restricted from moving in “x” and “y” directions. The force was then applied to the face of the top plate after being finely meshed similar to Figure A1-2. Consequently, the top face displaced downwards as shown in Figure A4-5.

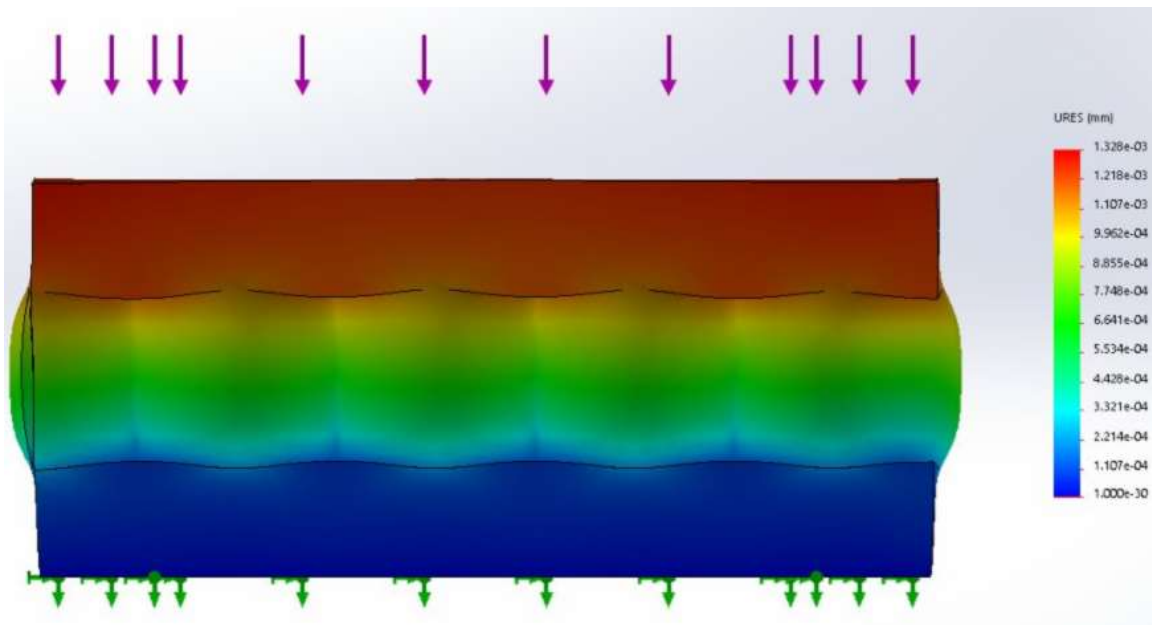


Figure A4-5 Displacement of honeycomb structure under bare compression.

The amount of displacement is determined by selecting two points from the top and bottom plates on the same y plane and finding the difference of their displacement. The selected points along with their displacement values are shown in Figure A4-6.

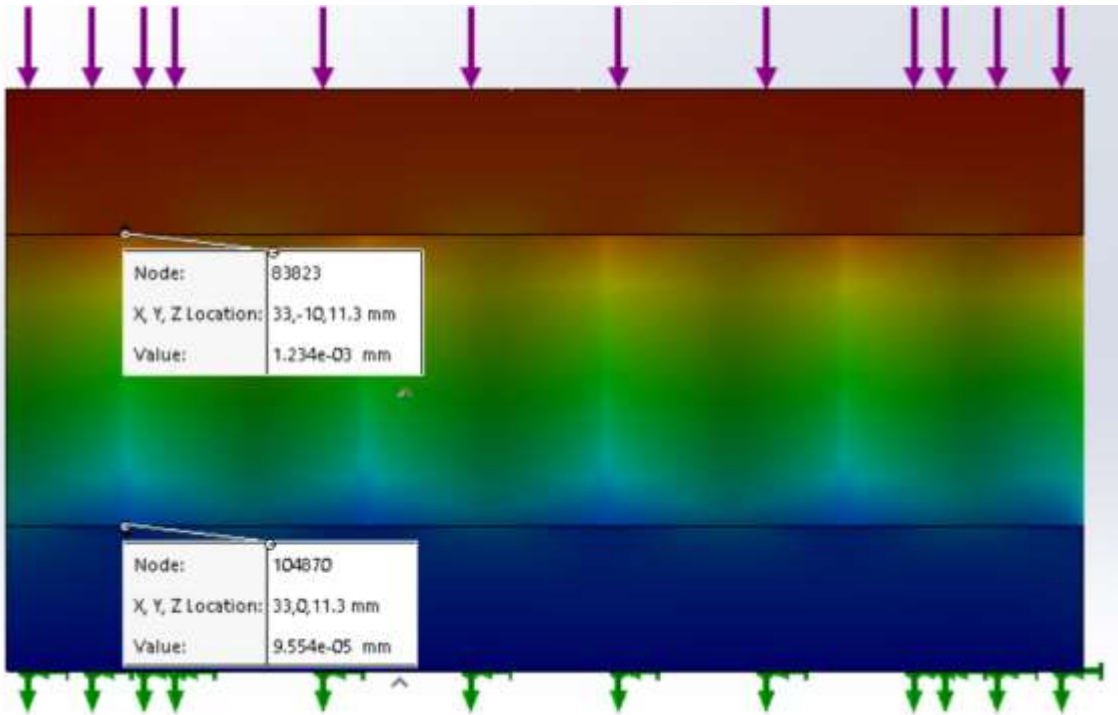


Figure A3-6 Displacement values on two points selected from the bare compression displacement model.

A3.2.1 Elastic Modulus in Bare Compression Sample Calculation

Elastic modulus is the resistance to deformation property of the structure. The following equation is used to obtain the elastic modulus of the honeycomb structure under bare compression:

$$E_c = \frac{F/A}{\Delta L/L}$$

In which F is the total force applied over the plate area A and ΔL is the change in original length, L, between the top bottom plates. The area of the plate and the original length are equivalent to the values used in the model loaded in shear. A 10N force was distributed over the plate's area. Change in displacement was calculated based on the points selected

in Figure A3-6. Finally, after obtaining all the required variables the elastic modulus was calculated as shown bellow:

$$E_c = \frac{(10 \text{ N})/(1098.3 \text{ mm}^2)}{((1.234*10^{-3})-(9.554*10^{-5}))/10} = 79.93 \text{ MPa}$$

The computed elastic modulus matched the one reported by the manufacturer in the technical data sheet presented in Figure A-1. This proves that the analytical model created on Solidworks is reliable and can be used to obtain additional required properties that are not reported by the manufacturer.

A3.3 Honeycomb Compression Test

The compression elastic modulus was acquired by conducting a compression test on the honeycomb structure at direction perpendicular to the cylindrical sections. The analytical model was tested multiple times—after changing the density of the honeycomb structure—to derive the correlation between density and elastic modulus, which is required for the development of the failure mode maps. A plate was attached on each load-bearing end of the structure prior to the compression test to allow an even distribution of the applied load. Figure 3-7, illustrated the boundary conditions applied to the analytical model. As shown in the figure below, one of the plates was fixed and restrained from moving within the “x” and “y” planes. Meanwhile, the other plate was set to move freely in all directions.

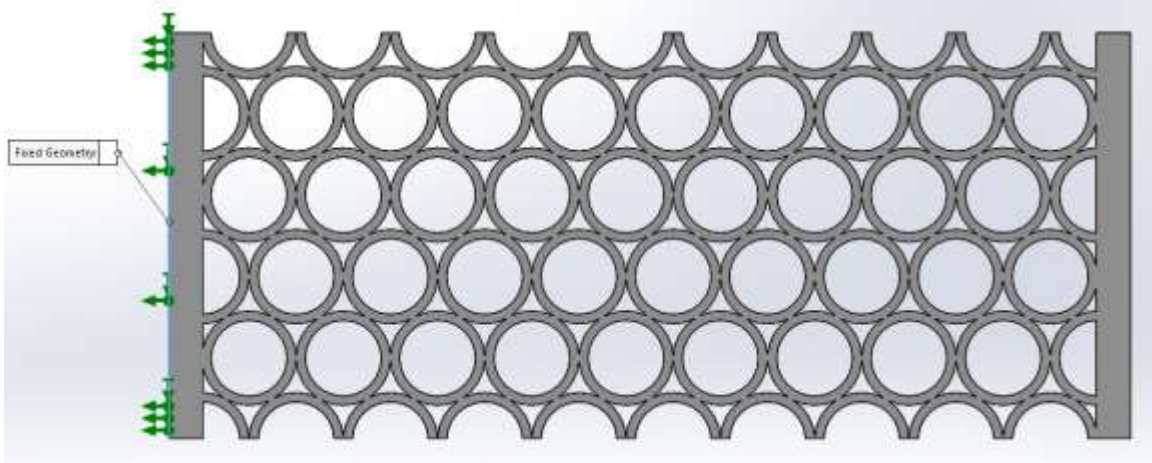


Figure A3-7 Analytical model and boundary conditions of honeycomb structure used in obtaining the compression elastic modulus.

After setting the boundary condition, the distributed load was applied to the unrestrained plate side and the model was finely meshed before running the analysis shown in Figure A3-8. Figure A3-9 illustrates the structure's displacement under the applied load, which is dependant on the thickness of the circular sections creating the honeycomb structure. For example, a honeycomb structure made from thick circular tubes will displace less than one made from thin circular tubes under a given applied load. The thickness of the tubes comprising the honeycomb structure influences its overall core density. Therefore, the honeycomb structure's compression elastic modulus is dependant on the core density. The following equation is used to obtain the elastic modulus of a honeycomb structure after its displacement under an applied load:

$$E_c = \frac{F/A}{\Delta L/L}$$

In which "F" is the sum of applied force, "A" is the area of plate that force is distributed on, "L" is the length of the intact structure, and "ΔL" is the structure's change in length resulting from applied force.

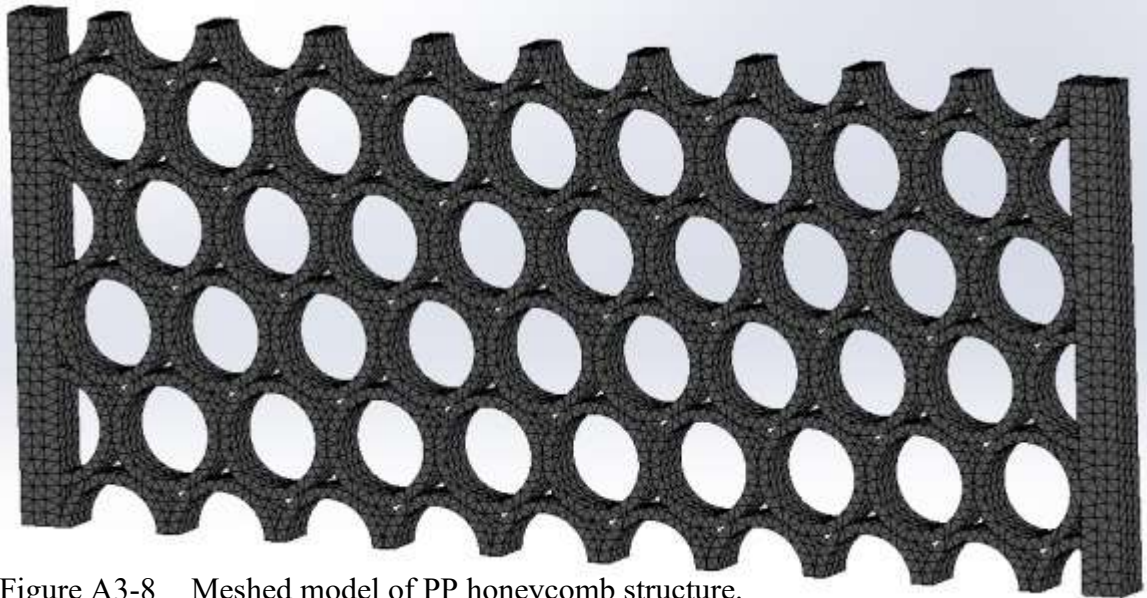


Figure A3-8 Meshed model of PP honeycomb structure.

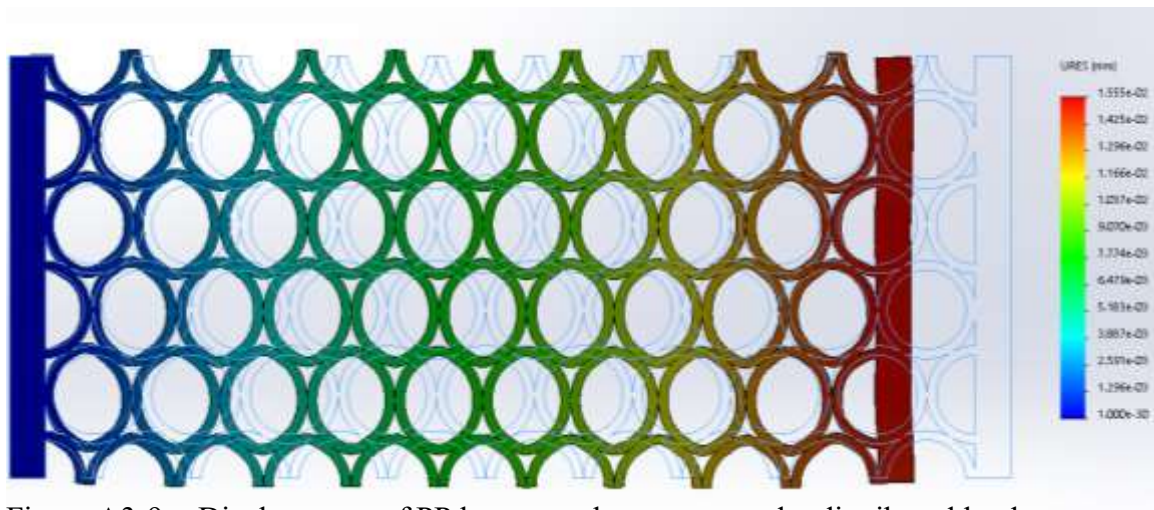


Figure A3-9 Displacement of PP honeycomb structure under distributed load.

To generate a relationship between the density of the honeycomb structure and elastic modulus, a compression test was conducted on numerous honeycomb structures with variable thicknesses. The “Mass Properties” tool in SolidWorks was used every time the thickness was modified to acquire the density of the new structure.

APPINDIX B: Computing Strain Using VBA Programming Language

B1 Overview

As shown in equation B-1, Richard-Abbott equation yields stress explicitly in terms of strain.

$$f = \frac{(E_1 - E_p) \cdot \varepsilon}{\left(1 + \left|\frac{(E_1 - E_p) \cdot \varepsilon}{f_0}\right|^n\right)^{1/n}} + E_p \cdot \varepsilon \quad (\text{B-1})$$

The disadvantage is that the above equation cannot be rearranged algebraically to provide strain in terms of stress. Because the load-deflection analytical model—which was developed in the previous chapters—begins with applying loads translating into stresses on the facing component of the sandwich structure, rearranging strain regarding stress becomes critical to carry out the load-deflection analysis. The only solution for this arithmetic operation is using iteration or a guessing and checking method. Iteration can be achieved in one step using a built-in “what if” analysis tool in Excel called “GoalSeek.” Despite momentarily outputting the strain value associated with each stress step, the analysis tool becomes inconveniently used when considering large stress data points. To overcome this drawback, decrease potential error, and complete the analytical model, a program was developed using Excel’s Visual Basic for Application (VBA) programming language, which will be displayed and analysed in this section.

B2 Introduction to VBE

The Visual Basic Editor (VBE) is an Excel application through which all VBA codes are developed. Hence, the first step in creating an Excel code is accessing VBE via “Alt +

F11.” When developing the code to obtain strain for the specified stress value, all stress values were selected prior to accessing the VBE. Figure B2-1(a-c) depicts the step-by-step procedure used prior to programming.

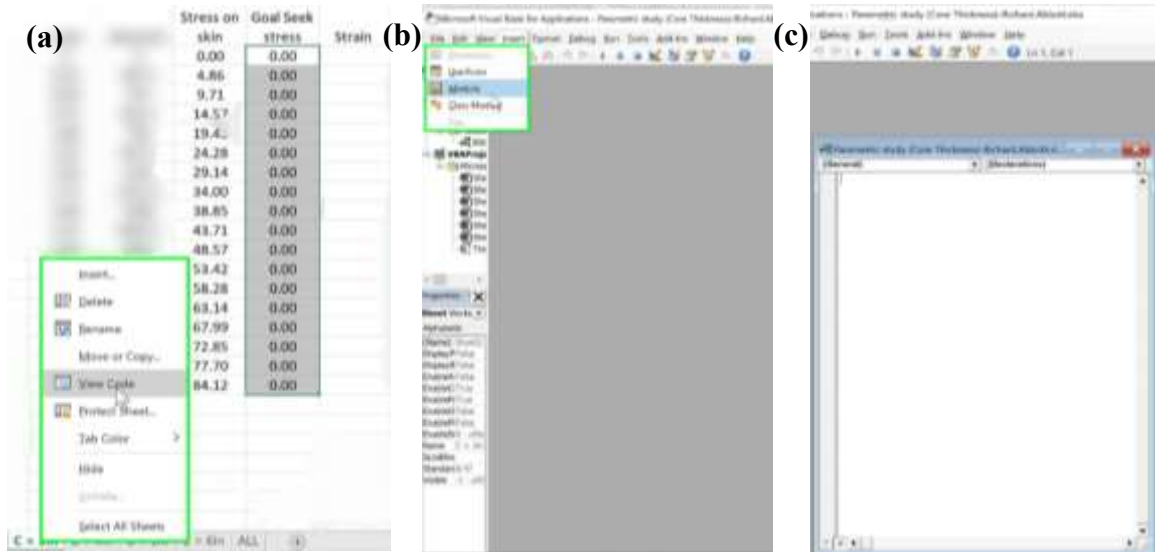


Figure B2-1 Procedure for accessing VBE; (a) selecting required cells and viewing the code; (b) inserting new module; and (c) activating module panel.

B3 Explanation of VBA Code

To compute the strain regarding stress using the VBA programming language, the code should first begin with “sub”—short for subroutine—as well as a given name for the program. In this stage, the program’s chosen name should not contain spaces or be categorized as a VBA reserved word. The program developed for this section was labelled “GoalSeekForAllCells.” Notably, the name does not influence the developed code; hence, any chosen moniker can run the same program. However, it is recommended to name a program based on the task required to deliver. After specifying the program’s name, the code’s second line is the Dim statement—the code section used to declare the program’s variable. The variable of the developed code is “c” and is declared as the range. As illustrated in section B2, this code range was selected from the Excel

spreadsheet prior to code development. The third line represents the code portion allowing the program to loop through all selected cells. To allow the program use of Excel's GoalSeek feature, the command line format should be precisely written. This format is dissected and explained below:

A'.GoalSeek **B'**, **C'**

In which **A'** corresponds to the cells including GoalSeek results, **B'** corresponds to the cells from which GoalSeek results are copied, and **C'** corresponds to the changing parameter required to achieve the GoalSeek result. Lastly, the final code statement is "End Sub." This is required to mark the completion of a given command and allows the code proper execution.

B4 VBA Code for GoalSeek Analysis

```
Sub GoalSeekForAllCells()  
Dim c As Range  
  
For Each c In Selection  
    c.GoalSeek Goal:=c.Offset(, -1),  
ChangingCell:=c.Offset(, 1)  
  
Next c  
End Sub
```

APPINDIX C: Shear Test on Polypropylene Honeycomb Core

C1 Overview

Unlike regular honeycomb structures created through infusion, the PP honeycomb structure is made by attaching adhesively bonded circular tubes. As a result, a series of weak points become present within the walls of the circular sections. For further analysis, a shear test was conducted on the PP honeycomb; three identical sections were consecutively tested under the same loading and boundary conditions. This section illustrates the loading apparatus of the shear test and explains the concept used to obtain the ultimate shear strength value from experimental testing results.

C2 Loading Apparatus

The primary goal of the testing apparatus is to allow the honeycomb structure to shear at a direction parallel to the honeycomb walls. The tested specimens' length, width, and thickness cross-sections are 305mm, 78mm, and 76mm, respectively. As shown in Figure C2-1(a), the loading set-up included three HSS sections completed on a Instron8501 material testing machine. The clearance space between the HSS sections was equivalent to 12mm. The clearance was necessary to simulate debonding within the circular sections, and the load applied by the Instron was monitored during the entire testing period. Finally, the peak load was recorded and used to obtain the ultimate shear strength value.

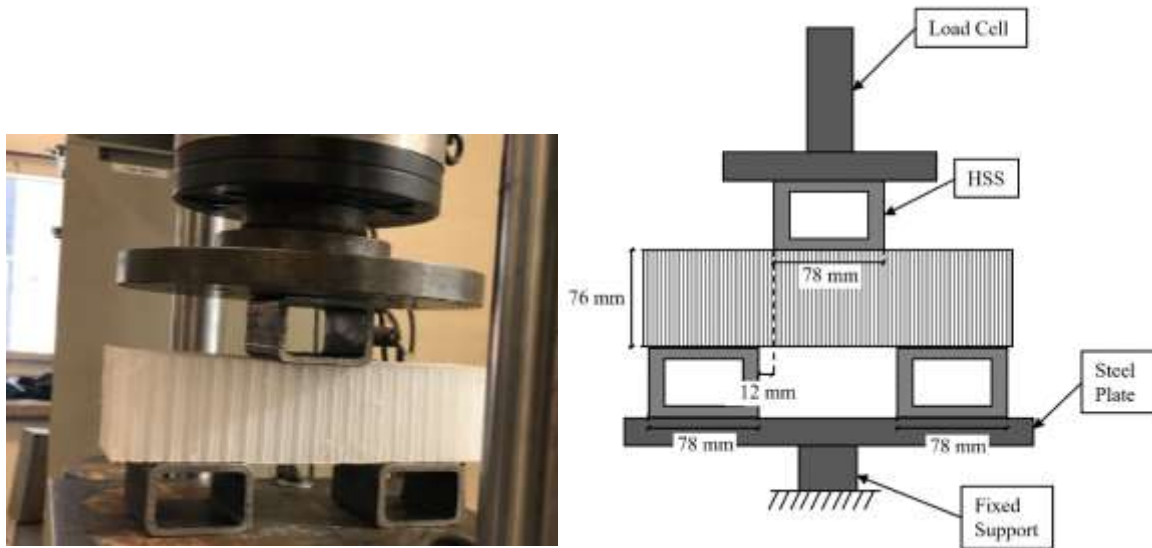


Figure 3-8 Shear test set-up; (a) front view; and (b) sketch including dimensional details.

C3 Ultimate Shear Strength Calculation

The applied load will delaminate two adhesive bonds; one from each side of the central HSS. Hence, the load required to delaminate one bond is equivalent to half of the ultimate peak load. Additionally, since delamination will occur on the entire cross-sectional area, the ultimate shear strength will equal half of the ultimate peak load divided by the cross-sectional area. This relation is as follows:

$$\tau_u = \frac{P_u/2}{bh}$$

APPINDIX D: Shear Contribution to Bending Analysed Within Parametric Study

D1 Overview

As the geometry of the sandwich beam changes, the contribution of shear deflection—respecting bending deflection within the total deflection term—continuously changes. When sandwich panels are used for structural applications, it is vital to understand the source of total deflection during the design stage. Hence, this section presents diagrams including models with total deflection deconstructed into shear and bending deflections.

D1.1 Breakdown of Total Deflection with Respect to Change in Core Thickness (Core Density = 80 kg/m³, 200 kg/m³, 320 kg/m³)

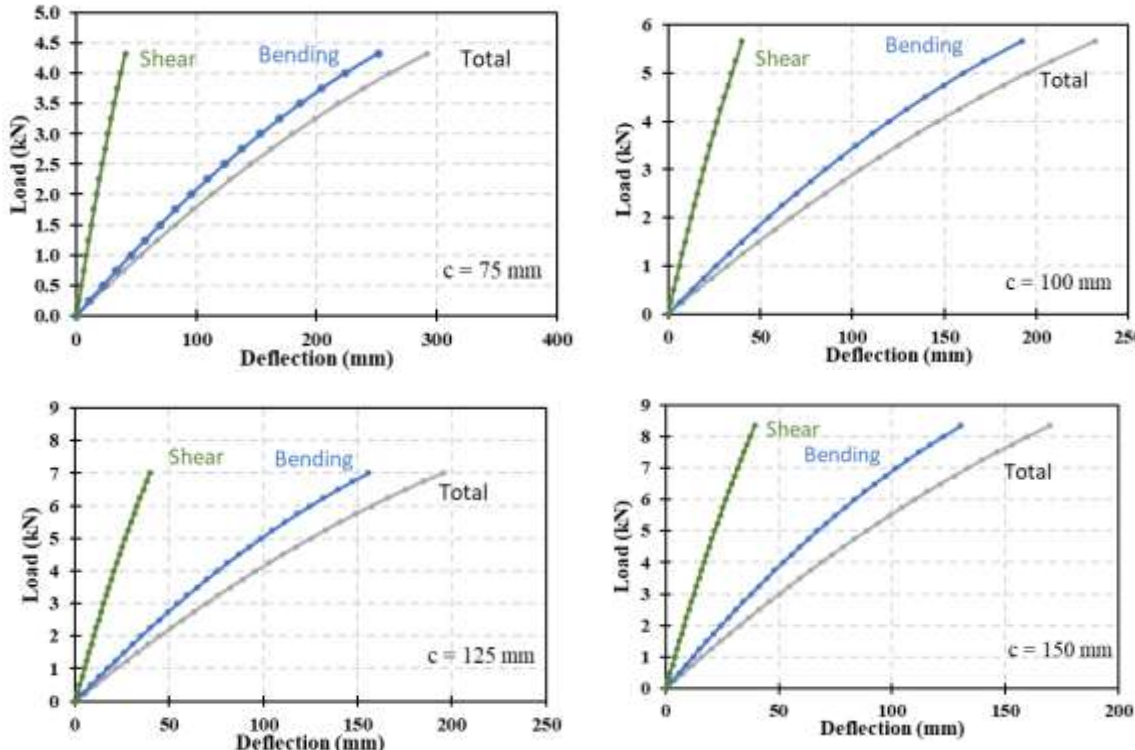


Figure D1-1 Breakdown of Total Deflection with Respect to Change in Core Thickness (Core Density = 80 kg/m³)

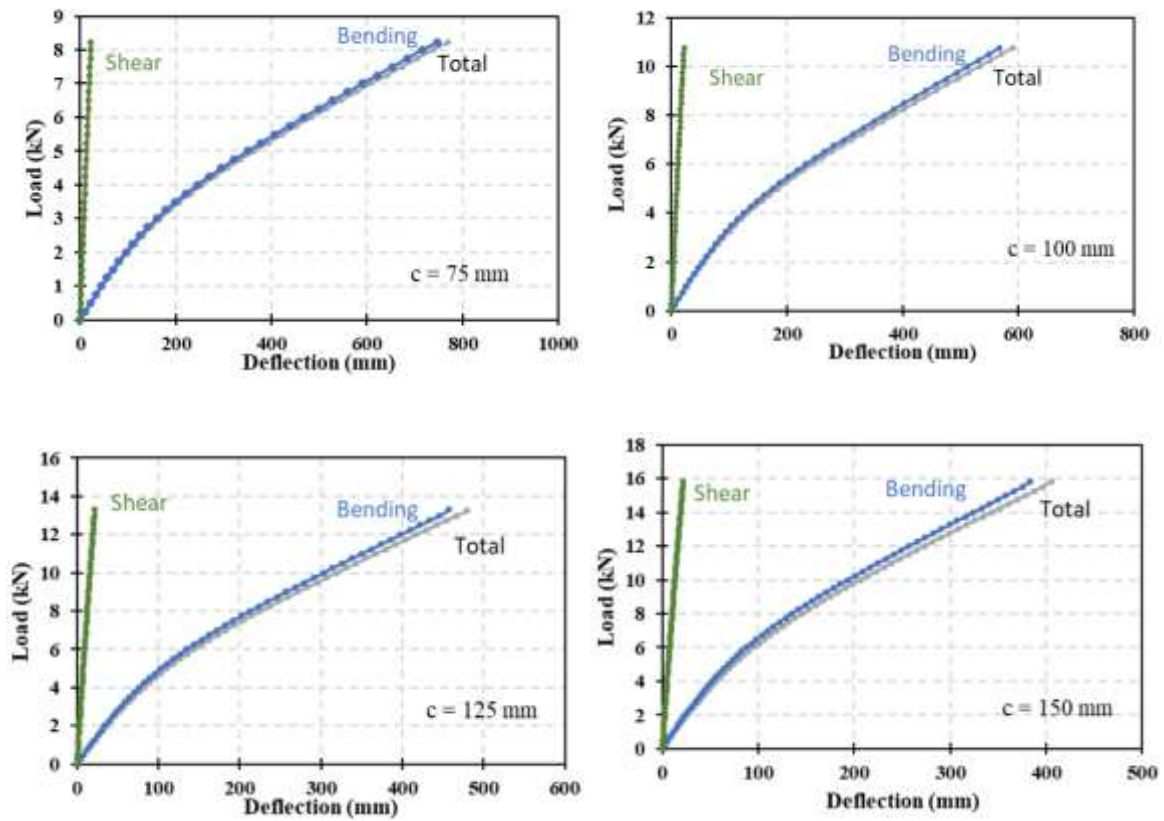


Figure D1-2 Breakdown of Total Deflection with Respect to Change in Core Thickness (Core Density = 200 kg/m³)

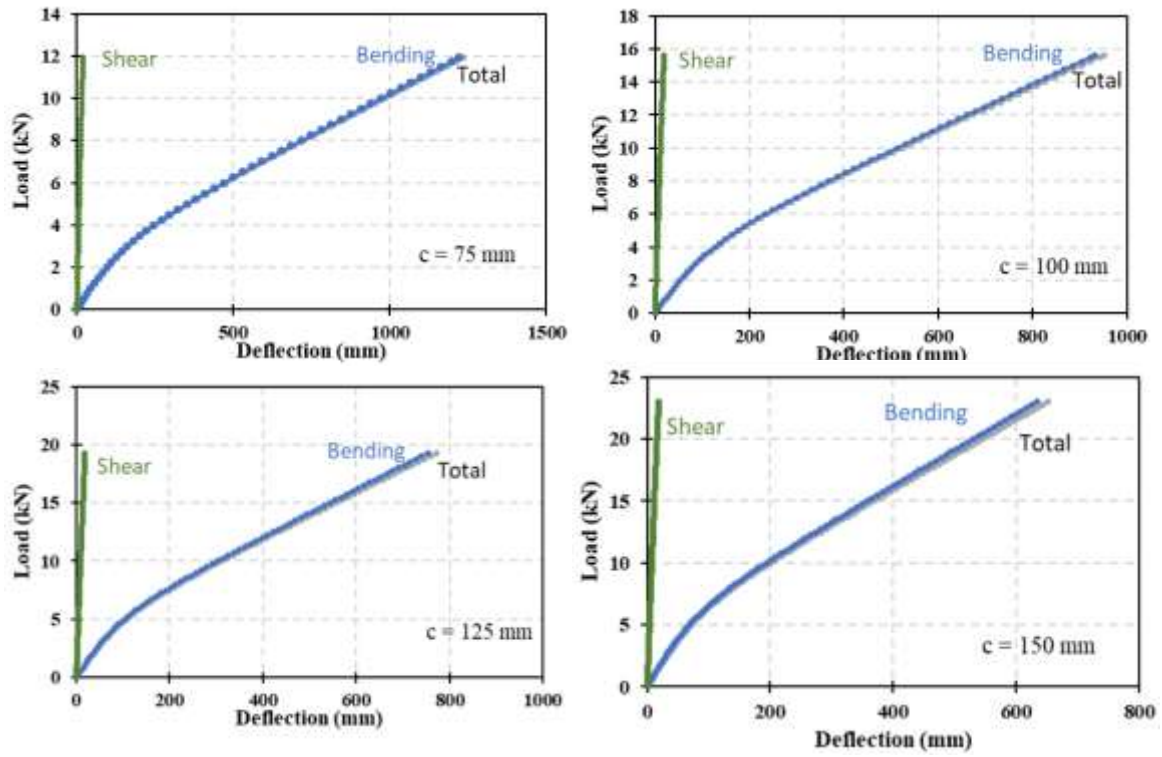


Figure D1-3 Breakdown of Total Deflection with Respect to Change in Core Thickness (Core Density = 320 kg/m^3)

D1.2 Breakdown of Total Deflection with Respect to Change in Facing Thickness (Core Density = 80 kg/m³, 200 kg/m³, 320 kg/m³)

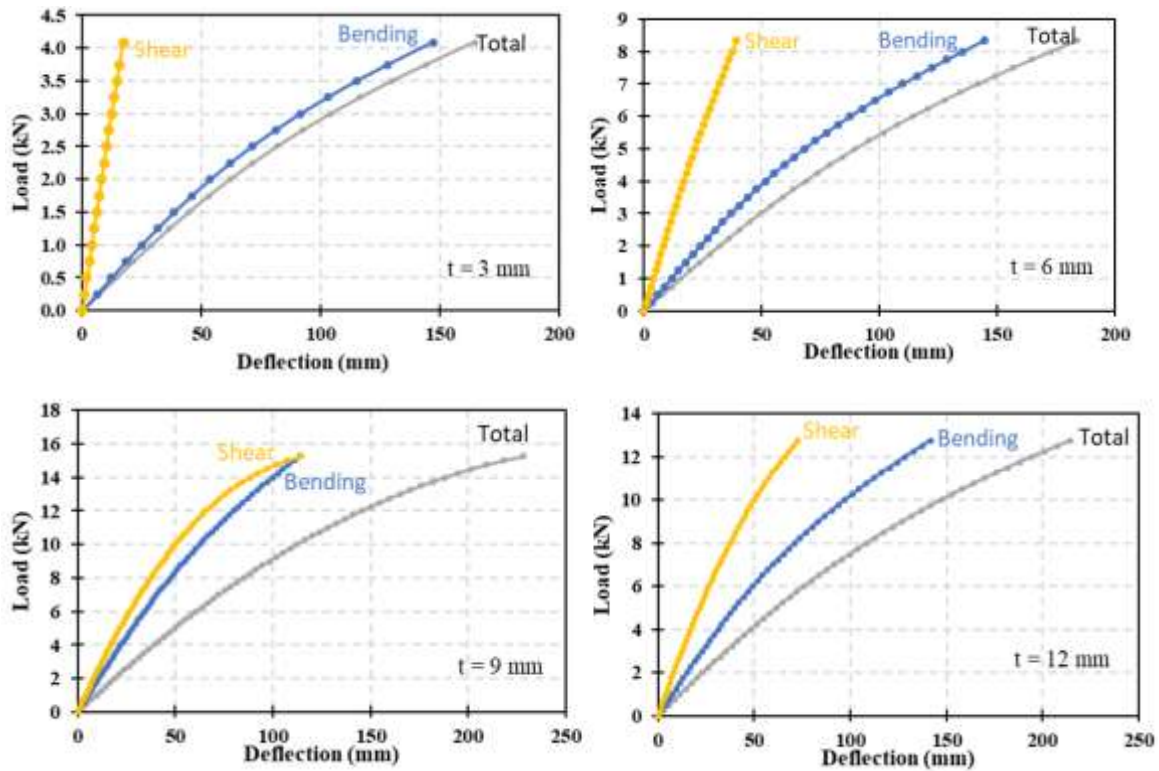


Figure D1-4 Breakdown of Total Deflection with Respect to Change in Facing Thickness (Core Density = 80 kg/m³)

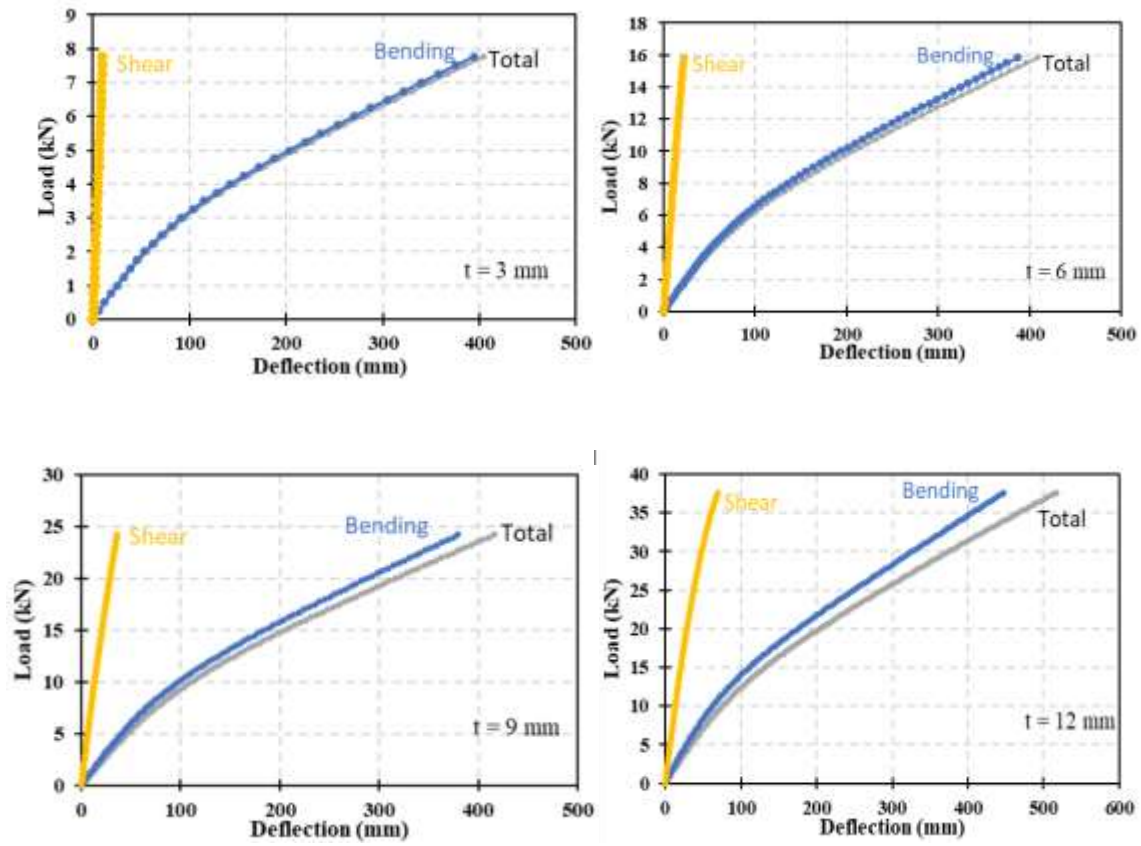


Figure D1-5 Breakdown of Total Deflection with Respect to Change in Core Thickness (Core Density = 200 kg/m³)

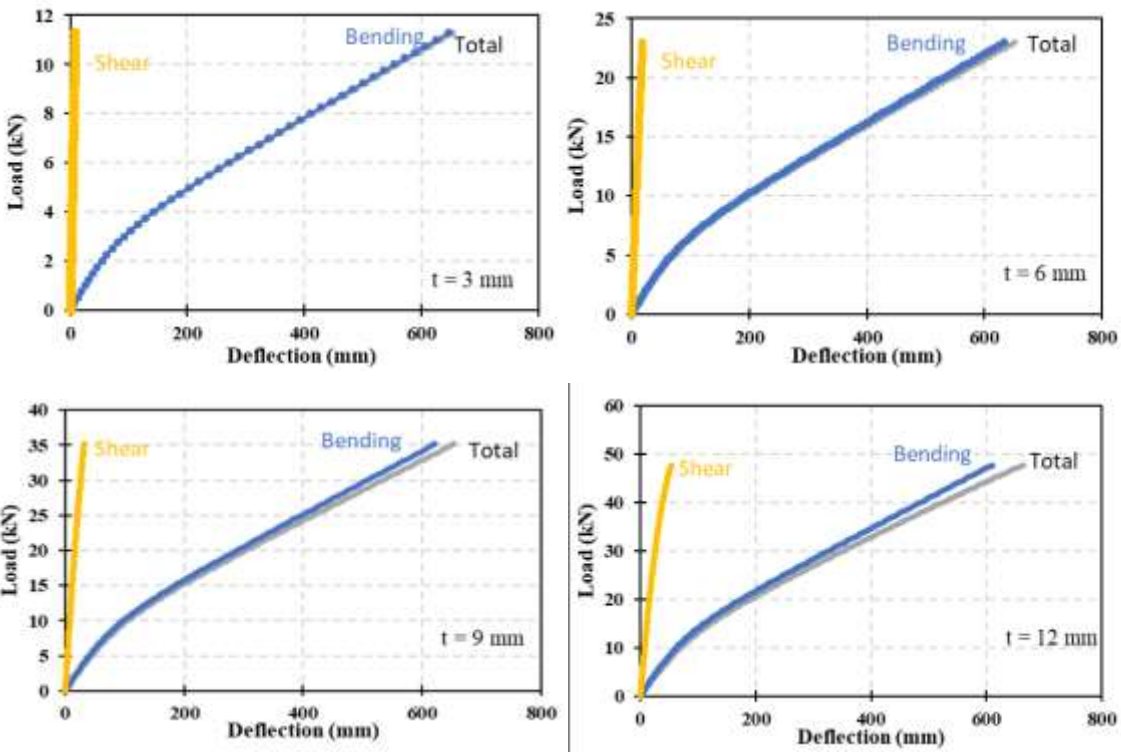


Figure D1-6 Breakdown of Total Deflection with Respect to Change in Core Thickness (Core Density = 320 kg/m³)

D1.3 Breakdown of Total Deflection with Respect to Change in Span Length (Core Density = 80 kg/m³, 200 kg/m³, 320 kg/m³)

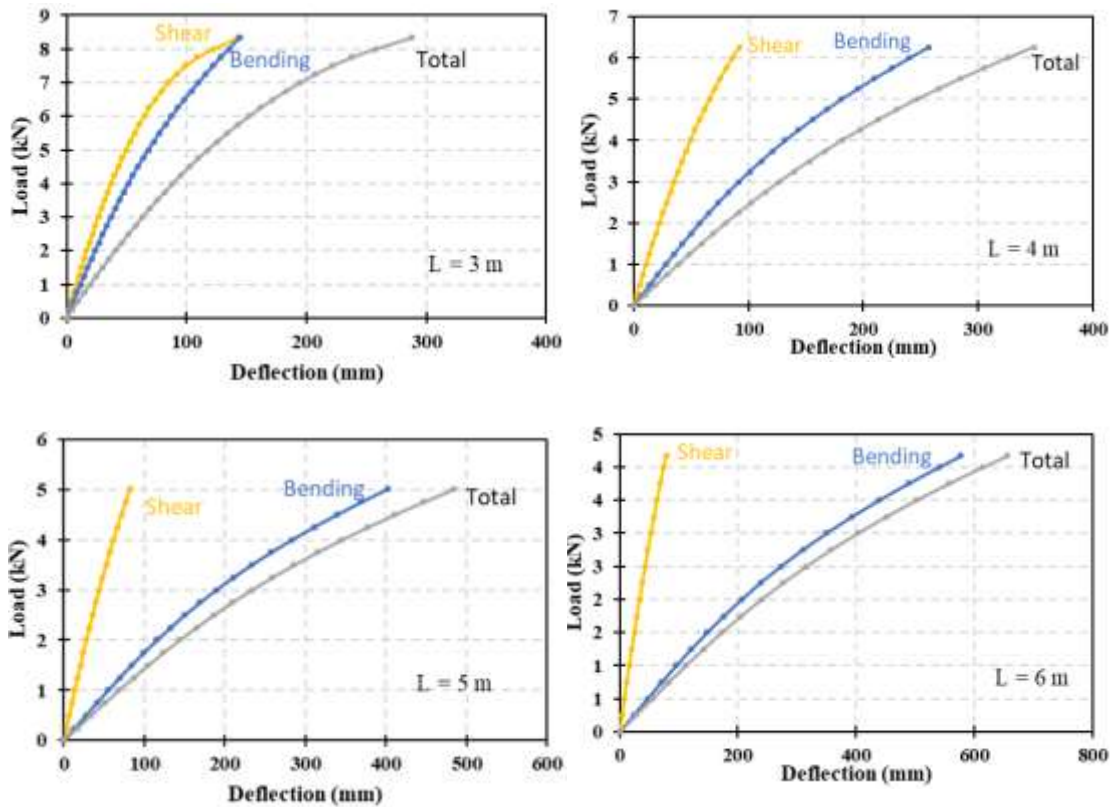


Figure D1-7 Breakdown of Total Deflection with Respect to Change in Span Length (Core Density = 80 kg/m³)

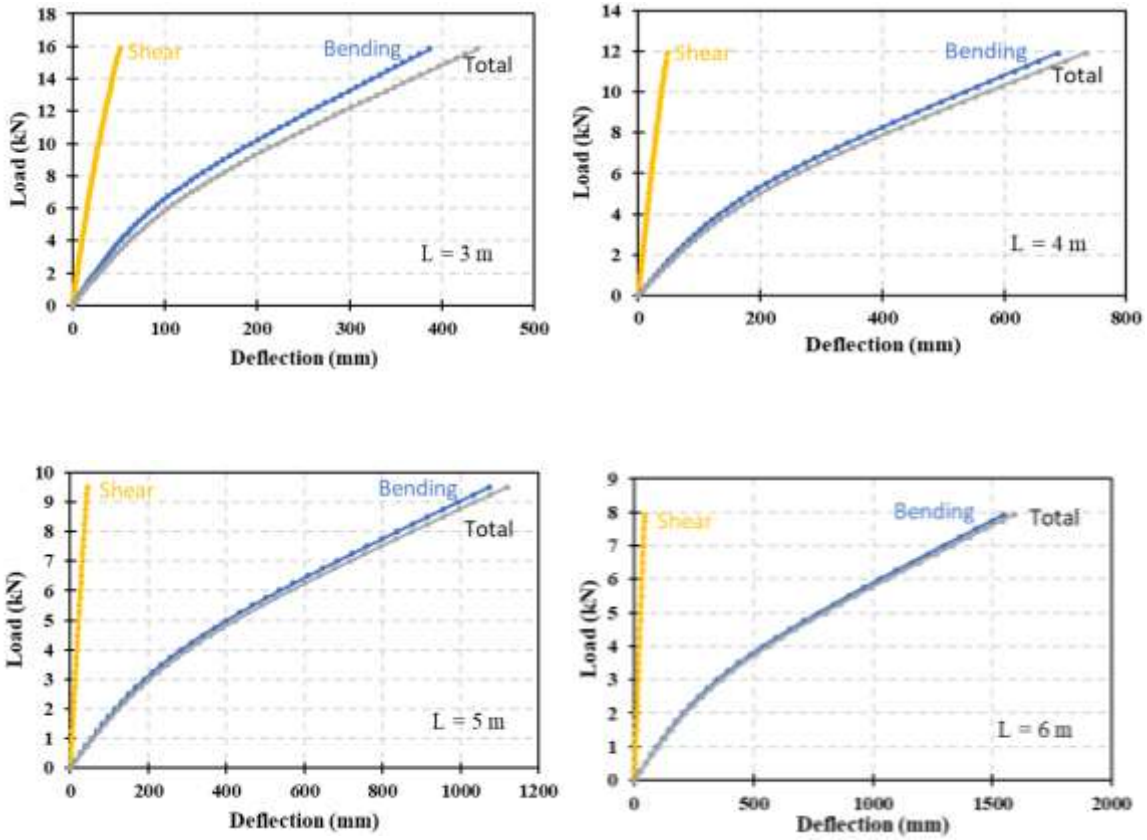


Figure D1-8 Breakdown of Total Deflection with Respect to Change in Span Length (Core Density = 200 kg/m³)

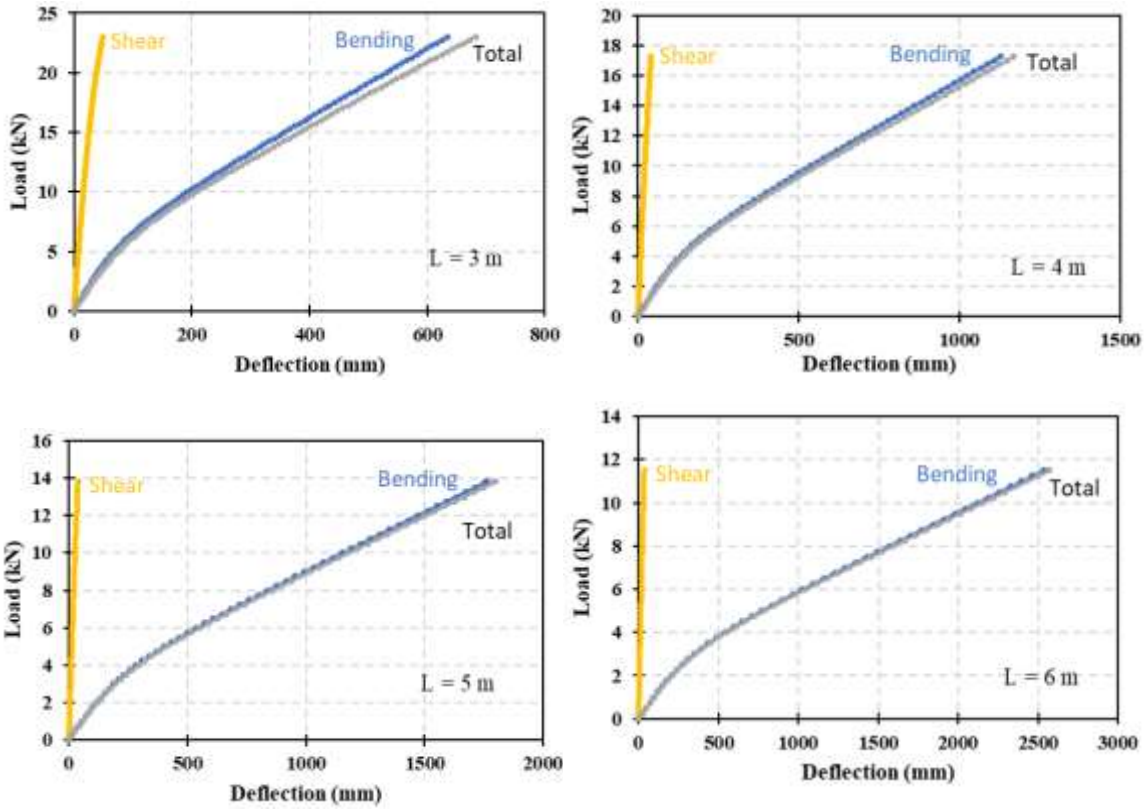


Figure D1-9 Breakdown of Total Deflection with Respect to Change in Span Length (Core Density = 320 kg/m^3)